The Dissertation Committee for Paul M King
certifies that this is the approved version of the following dissertation:

Electron and X-ray source development using picosecond, kilojoule class laser systems

Committee:

Bjorn Manuel Hegelich, Supervisor

Félicie Albert, Co-supervisor

John Keto

Michael Downer

Electron and X-ray source development using picosecond, kilojoule class laser systems

by

Paul M King

DISSERTATION

Presented to the Faculty of the Graduate School of

The University of Texas at Austin

in Partial Fulfillment

of the Requirements

for the Degree of

DOCTOR OF PHILOSOPHY

THE UNIVERSITY OF TEXAS AT AUSTIN

May 2021

This dissertation is dedicated to my friend Franki Aymond.

Acknowledgments

There are so many people I would like to acknowledge and who made my journey through graduate school possible. I would like to start on a personal note and thank all of my family and friends who have provided unending support. My parents who helped keep me sane by always offering to fly me home for a weekend break where they feed me until I explode. My friends from Maryland who make the effort to stay in touch when I get in the grind and don't reach out to them. My friends in Texas who talk about science and are always willing to take a break at Crown or sit in a pool. My friends in California who helped me form a new community right after finding my place in Texas. Thank you all.

I would also like to thank Félicie and Nuno for being incredible mentors and teaching me everything I know about how to run experiments. You both taught me the rigor I needed when making measurements and writing papers. It is hard to put into words how much you have helped me learn and grow and how much I have enjoyed my time working with you. Thank you to Manuel and my other committee members who have each helped me through navigating graduate school and where to focus my academic energy.

Thank you.

Electron and X-ray source development using picosecond, kilojoule class laser systems

Paul M King, Ph.D.
The University of Texas at Austin, 2021

Supervisor: Bjorn Manuel Hegelich
Co-supervisor: Félicie Albert

Self-modulated laser wakefield acceleration (SM-LWFA) of electrons, driven by picosecond, kilojoule class laser systems is a promising method to produce versatile x-ray sources. The electron beams, accelerated up to ≈300 MeV, are used to produce broadband (keV to MeV), low divergence (¡ 50 mrad), high photon number ($> 10^{10}$ photons/keV/sr) x-ray sources utilizing betatron, inverse Compton scattering, and bremsstrahlung generation mechanisms. The x-ray energy spectrum and source size can be tuned by controlling the SM-LWFA directly or the x-ray generation mechanism to provide an optimized source for radiography applications. We will discuss experimental results on electron beam and x-ray source characterization, obtained at the Jupiter Laser Facility (LLNL), and supported by 2D and 3D Particle-In-Cell simulations. Additionally, we will show several static radiography applications relevant to high energy density science and inertial confinement fusion experiments and how this source can be tuned to improve image quality in radiography. X-ray analysis tools have been developed to measure high energy x-ray spectra, source size, and radiography quality, and we have used LLNL's x-ray ray tracing code HADES to simulate radiographic images of experimental objects and help in planning for future experiments and applications. Finally, MeV x-ray source characterization and radiography applications

are explored using laser-solid interactions enhanced by compound parabolic concentrators (CPC).

This work was performed under the auspices of the U.S. Department of Energy under Contract No. DE-AC52-07NA27344, DE-SC0019010, DE-SC0010064 (UCLA), DE-SC0021057, NNSA grant DE-NA0003873 (UCLA) and NSF grants 1806046, 1804463, 1734315, and 2003354 (UCLA), LLNL subcontract B634451, FA9550-14-1-0045, and supported by the DOE Office of Science Early Career Research Program (Fusion Energy Sciences) under SCW1575-1.

Table of Contents

List of Figures

Chapter 1

Introduction

Laser wakefield acceleration (LWFA) produces beams of relativistic electrons [2, 3] that can be used to generate directional x-rays [4] useful for several applications in science and industry. A few examples of applications of LWFA-driven x-ray source are: imaging biological samples [5], laser-driven shock fronts [6] and surface defects in alloys [7]. These applications are enabled by the highly advantageous features of LWFA-driven x-rays [8]: a small μm-sized source allowing for very small resolution in imaging applications, low divergence (< 50 mrad) allowing the x-ray source to be placed far from an object, extremely broad (keV–MeV) range of photon energy which enables energy selection to match the need of an application, and synchronization with the drive laser to within 10's of femtoseconds. These attractive characteristics are attained by operating LWFA in the blowout regime [9] with Joule-class, sub-50-fs-duration laser pulses.

By contrast, many High Energy Density Science (HEDS) facilities such as the National Ignition Facility (NIF) at the Lawrence Livermore National Laboratory, the OMEGA Laser at the University of Rochester, the Z-Machine at Sandia National Laboratories, and the Laser Mégajoule at the Commissariat à l'Energie Atomique are all coupled to picosecond-duration, kilojoule-class laser systems unable to operate in the blowout regime of LWFA. The NIF, for example, is a laser facility designed for indirect drive fusion experiments. NIF has 192 kilojoule-class, ns-scale laser pulses which are frequency tripled and focused in an asymmetric polar configuration. These beams are frequently utilized for high energy density (HED) and inertial confinement fusion (ICF) experiments [10, 11]. The OMEGA laser

similarly utilizes 60 kilojoule class, ns-scale laser pulses to drive HED and ICF experiments. OMEGA, however, has a symmetric laser distribution around a spherical target chamber enabling direct drive fusion experiments. The Z-Machine uses extreme electric currents flowing through small wires to conduct z-pinch experiments. The high current flow through the wires causes the wires to attract to one another, pinching in a cylindrical symmetry. Experiments at each of these facilities produce dense transient states of matter which can be probed through the use of high energy x-rays.

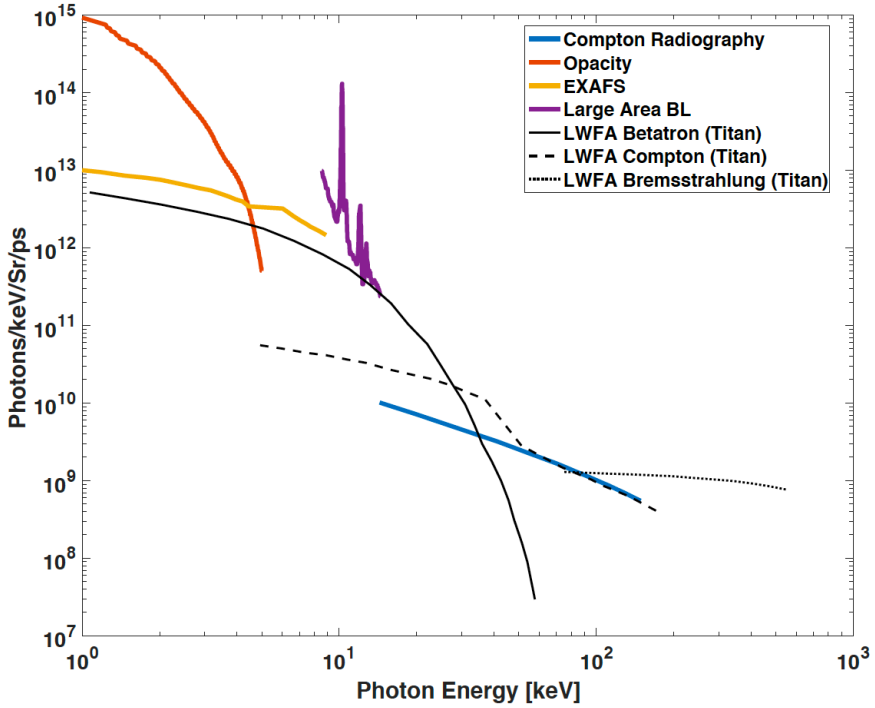

Figure 1.1: Comparison of x-ray sources from various platforms on NIF with self-modulated laser wakefield acceleration driven x-ray sources on the Titan laser system. Figure provided by Dr. Félicie Albert, LLNL.

Understanding the relationships between temperature, pressure, and density in the extreme environments created at these large facilities is crucial and has implications in

planetary science [12], inertial confinement fusion [10], and laboratory astrophysics [13]. A limiting factor at these facilities has been the quality of x-ray sources available to diagnose experiments. To generate an x-ray source in tandem with the NIF beams, for example, the advanced radiographic capability (NIF-ARC) was developed and is used to generate bremsstrahlung and line emission x-ray sources through laser solid interactions. NIF-ARC achieves the relativistic laser intensities needed for high photon flux x-ray sources through chirped pulse amplification (CPA) of 4 NIF beams [14]. This allows NIF-ARC to deliver a 1 to 10 ps laser pulse with > 250 J of energy, reaching a peak laser intensity of $\approx 10^{18}$ W/cm^2. Figure 1.1 shows a comparison of existing x-ray sources on the NIF platform with sources driven by self-modulated laser wakefield accelerated (SM-LWFA) electrons. The existing x-ray sources use K-shell emission [15] for compton radiography, imploding fuel cell continuum emission [16, 17] for EXAFS and opacity measurements, respectively, and bremsstrahlung [18] radiation sources for large area back-lighting. While they provide high photon flux, there are gaps in the energy spectra which, at present, have no competing x-ray source available.

LWFA-driven sources, as shown in figure 1.1, have the potential to enable ultrafast resolution of dynamic experiments and provide measurements with unparalleled spatial resolution [19, 20, 1] at energy ranges where no x-ray source is currently available. While the promise of such x-ray sources is evident, optimization of LWFA-driven x-rays with the picosecond-duration lasers available at HEDS facilities necessitates a detailed understanding of the underlying physics of electron beam generation mechanisms—not in the LWFA regime, but in the self-modulated LWFA (SM-LWFA) regime [21], which is as yet incomplete.

Additionally, a characterization of SM-LWFA-driven x-ray generation mechanisms are needed to determine viability as a compact, versatile x-ray source to probe dense, transient states of matter created during high energy density (HED), inertial confinement fusion (ICF), and laboratory astrophysics studies. To date, research in x-ray source development at NIF and OMEGA has primarily focused on the development and improvement of laser-driven

bremsstrahlung and line emission backlighters [22, 23, 24, 25, 26]. The backlighter sources have been used to provide critical insight into various experimentally unexplored processes like shock propagation through materials [27], instabilities in compressed gas [28], and the shape and velocity of imploding shells [29, 30]. These sources commonly produce energies < 20 keV with laser to x-ray conversion efficiencies of a less than a few percent in some materials, and have large source sizes, > 250 μm [25, 26, 31]. The large source size from these backlighters can be mitigated with pinholes to reduce the effective source size and increase the resolution of radiographic images by sacrificing photon flux and contrast of the image [22, 23]. An improved x-ray source to be used in similar experiments at NIF and OMEGA would need to have a broad energy range (few keV to MeV), high photon flux ($> 10^{10}$ photons/keV/sr), and small source size (< 20 μm).

The work presented in this dissertation will detail the work to develop and characterize an x-ray source driven by SM-LWFA on kilojoule class, ps laser systems and applications to static x-ray radiography experiments. Additionally, work with laser-solid interactions to generate bremsstrahlung radiation is explored and characterized. While additional work is needed to properly compare the laser-solid and SM-LWFA driven MeV x-ray sources, the initial work in characterization and application to static radiography is presented in this dissertation.

Chapter 2

Electron Acceleration with Laser Plasma Accelertors

2.1 Introduction to Laser Plasma Interactions

2.1.1 General Plasma Definitions

Plasma is generally regarded as the fourth state of matter, taught in many primary school curricula after the introduction of solid, liquid, and gas states. Plasma, unlike solids, gases, and liquids, is an introduction to states of matter which are more abstract to our everyday interactions with the world. Plasma is a state of matter which can have densities ranging from a low gas-like density to high solid densities. However, unlike gases and solids, plasma is ionized, allowing the electrons to move unbound to constituent atoms. The unbound, high-energy electrons introduce new physical processes and mechanisms which can be used in applications as far reaching as producing light in homes to the manufacturing of computer processors. Plasma is also a highly abundant state of matter in planetary atmosphere and stars, motivating laboratory experiments which simulate hard to reach cosmic processes.

A plasma can be defined more rigorously through the plasma parameter:

$$\Lambda = 4\pi n_e \lambda_D^3 \tag{2.1}$$

where n_e is the electron number density and $\lambda_D = \sqrt{\frac{k_b T_e \epsilon_0}{n_e e^2}}$ is the Debye length, where $k_b T_e$ is the temperature of the electron population in units of energy, and ϵ_0 is the permittivity of free space. When the plasma parameter is much greater than 1, the plasma

is considered ideal and can be characterized through collective behavior rather than single electron interactions. The plasma parameter is dictated by the Debye length which is the characteristic distance over which the electrostatic potential of a charged particle falls off by $1/e$. A large Debye length, as seen in eqn. 2.1, indicates unbound electrons able to interact over large distances causing collective behavior. For this reason, plasmas can be described through fluid equations, i.e. when describing plasma expansion, as well as kinetic equations, i.e. particle in cell simulations.

There are several plasma parameters of importance to describe a plasma fully. Among this list is the plasma frequency, used to determine the most fundamental time scale of a plasma $\tau_p = \frac{1}{\omega_p}$, which is given by:

$$\omega_p = \left[\frac{n_e e^2}{m_e \epsilon_0}\right]^{1/2} \tag{2.2}$$

where n_e is the electron number density, e is a unit charge of the electron, m_e is the mass of an electron, and ϵ_0 is the permativity of free space. This equation indicates that by controlling the density of the plasma, the fundamental time scales of that plasma will scale as the square root of the density variation. This plays an important role in the control of a LWFA described in future sections.

From the plasma frequency equation, we can now derive the critical density of a plasma by setting the plasma frequency to be equal to the frequency of an interacting light wave.

$$n_{crit} = \omega_0^2 \frac{m_e \epsilon_0}{e^2} \tag{2.3}$$

where ω_0 is the light wave frequency. The critical density dictates the radiation frequency at which the plasma will appear transparent to an incoming light wave or, conversely,

reflective. For a given laser frequency, the plasma density can be varied to be above or below the n_{crit} of a plasma to control the laser plasma interactions. A plasma which is below the n_{crit}, $n_e/n_{crit} << 1$, of an incoming laser is said to be underdense, and a plasma above the n_{crit} value is overdense, $n_e/n_{crit} >> 1$. While the light wave is reflected from the surface of an overdense plasma, there is a characteristic depth in which the light wave can travel into the plasma. This distance is called the skin depth and is given by:

$$l_s = \frac{c}{\omega_p} \tag{2.4}$$

where c is the speed of light. The skin depth of the plasma is an important parameter for laser-solid interactions as solid densities typically create overdense plasmas which will quickly reflect the laser light, sending laser energy away from the intended interaction region.

2.1.2 High Intensity Lasers

One way to create plasma is through the interaction of an intense laser pulse with solid or gaseous matter. The normalized vector potential of a laser field is given by:

$$a_0 = \frac{eE_0}{m\omega_0 c} \approx 0.85 \left[\frac{I_L \lambda^2}{1.4 \times 10^{18}}\right]^{1/2} \tag{2.5}$$

where E_0 is the electric field of the laser, I_L is the intensity of the laser in W/cm^2, and λ is the laser wavelength in μm. The a_0 of a laser is the dimensionless threshold of a laser intensity in which electrons will undergo relativistic oscillations in the laser field. For $a_0 >> 1$ the laser plasma interaction is relativistic.

For $a_0 > 1$, an electron oscillating in the laser electric field will experience a net gain in momentum through the ponderomotive force. This is caused by the magnetic field

component of the laser pulse to no longer be negligible. The force on an electron oscillating in an electric field is given by:

$$\mathbf{F} = m\ddot{\mathbf{x}} = -e\left(\mathbf{E} + \mathbf{v} \times \mathbf{B}\right) \tag{2.6}$$

where $\ddot{\mathbf{x}}$ is the acceleration of the electron, e is the fundemental charge, $\mathbf{E}$ is the electric field, $\mathbf{v}$ is the electron velocify, and $\mathbf{B}$ is the magnetic field. For low laser intensity interactions, the electron motion is dominated by the laser electric field, causing transverse oscillations of the electron in the laser field. This electron motion is called the quiver velocity and is obtained by setting the magnetic field component to zero, $\mathbf{B} = 0$ in equation 2.6. The result is as follows:

$$\frac{\partial \mathbf{v}}{\partial t} = \frac{-e\mathbf{E}}{m} \tag{2.7}$$

where $\mathbf{E} = E_0 cos(\omega_0 t)$. Then:

$$\mathbf{v}_{quiver} = \frac{eE_0}{m\omega_0} sin(\omega_0 t) \tag{2.8}$$

The quiver velocity describes the motion of the electron oscillating in the laser electric field, transverse to the laser propagation direction, where the magnetic field component is negligible. However, for and intense laser pulse with a finite spatial and temporal size, the laser pulse can accelerate electrons through the ponderomotive force. This force can be derived by expanding the electron position into a super position of motion in a fast oscillation caused by the electric field and a slow drift due to a slow changing envelope as follows:

$$\mathbf{x}(t) = \mathbf{x}_f(t) + \mathbf{x}_s(t) \tag{2.9}$$

where $\mathbf{x}_f(t)$ is the fast moving electron in the electric field oscillations, and $\mathbf{x}_s(t)$ is the electron drift caused by the slowly varying envelope, and the time average $\langle \mathbf{x}(t) \rangle = \mathbf{x}_s(t)$. Taylor expanding the electric field around the slow varying electron position results in the following:

$$\mathbf{E}(\mathbf{x}(t), t) = \mathbf{E}(\mathbf{x}_s(t) + \mathbf{x}_f(t), t) \approx \mathbf{E}(\mathbf{x}_s(t), t) + (\mathbf{x}_f(t) \cdot \nabla)\mathbf{E}(\mathbf{x}_s(t), t) \tag{2.10}$$

We then calculate the electron position in the fast oscillating field by inserting the taylor expanded electric field into equation 2.6 where the magnetic field is neglected:

$$m\ddot{\mathbf{x}}_f = q\mathbf{E}(\mathbf{x}_s(t), t) \rightarrow \mathbf{x}_f(t) = \frac{-q}{m_e \omega^2}\mathbf{E}(\mathbf{x}_s(t), t) \tag{2.11}$$

where q is the electric charge, m_e is the electron mass, and ω the oscillation frequency in the field. We then solve for the slow drift of the electron while including the effects of the magnetic field.

$$m\ddot{\mathbf{x}}_s(t) = m\langle \ddot{\mathbf{x}}(t) \rangle = q\langle \mathbf{E}(\mathbf{x}(t), t) + \frac{q}{c}\langle \mathbf{v} \times \mathbf{E}(\mathbf{x}(t), t) \rangle \tag{2.12}$$

where

$$\langle \mathbf{E}(\mathbf{x}(t), t) \approx \langle (\mathbf{x}_f(t) \cdot \nabla)\mathbf{E}(\mathbf{x}_s(t), t) \rangle \tag{2.13}$$

and

$$\langle \mathbf{v} \times \mathbf{E}(\mathbf{x}(t), t) \rangle = \langle \mathbf{v}_f \times \mathbf{B}_s \rangle \approx \frac{-qc}{4m_e \omega^2} \left(\mathbf{E}(\mathbf{x}_s(t) \times (\nabla \times \mathbf{E}(\mathbf{x}_s(t), t)) \right. \tag{2.14}$$

where $\nabla \times \mathbf{E} = \frac{\partial B}{c\partial t}$ is substituted in. Plugging these results into equation 2.12 and using the vector formula $\nabla|E| = (\mathbf{E}\cdot\nabla)\mathbf{E} + \mathbf{E} \times (\nabla \times \mathbf{E})$ results in the final ponderomotive force equation given by:

$$\mathbf{F}_{pond} = -\frac{q^2}{2m_e\omega^2}\nabla\langle\mathbf{E}^2(\mathbf{x}_s(t), t)\rangle \tag{2.15}$$

Therefore, electrons interacting with an intense laser pulse will be pushed away from areas with the largest gradient in laser intensity. Given that $\mathbf{F} = -\nabla\phi_p$, where ϕ_p is the ponderomotive potential. We then get $\phi_p = \frac{I}{2cn_{crit}}$ and we can calculated an expected potential for typical experimental conditions. For a laser wavelength of 1 μm, and a laser intensity of 5×10^{18} W/cm^2 we get that $\phi_p \approx 0.5$ MeV. This force is responsible for many of the processes discussed in this dissertation including the formation of a laser wakefield accelerator and electron acceleration in laser solid interactions.

Another important concept in high intensity laser plasma interactions is that of self focusing. Self focusing of a laser pulse occurs in a plasma when the index of refraction, defined as $n = c/v_p = ck/\omega$ where v_p is the plasma velocity, and k is the wave number, for the plasma increases as laser intensity increases. For a high enough laser intensity, the index of refraction adds a 2nd term which is dependent upon the laser intenstiy, $n = n_1 + n_2 I$. Using the dispersion relation $\omega_0^2 = \omega_p^2 + k^2c^2$ we find the index of refraction in the plasma to be:

$$n \simeq 1 - \frac{\omega_p^2}{2\omega_0^2} \tag{2.16}$$

We then make a correction due to relativistic electron mass effects caused by the transverse oscillations, $\omega_p^2 = \frac{\omega_p^2}{\gamma}$ and convert to experimental variables using the plasma

density and critical density definitions to obtain:

$$n = 1 - \frac{n_e}{2\gamma n_c} \tag{2.17}$$

Setting the 2nd term to be equal to the intensity dependent portion of the index of refraction definition gives us that $n_2 = \frac{2n_e}{\gamma n_c}$. This effect causes the laser pulse to be focused inside the plasma until laser power diminishes too much to sustain the effect or diffraction becomes dominant. For a Gaussian laser pulse to be self focused in a plasma it must then have a greater power than that of the critical power, given by:

$$P_{crit} = 17.4\frac{\omega_0^2}{\omega_p^2}[GW] \tag{2.18}$$

If the laser power is below this value, self focusing will not occur. For a 1 μm laser pulse and a plasma density of 1×10^{18} cm^{-3}, the critical power is $P_c = 1.7 \times 10^{13}$ W.

Self focusing is an important concept for laser wakefield acceleration as it allows a laser pulse to be guided in an under-dense plasma for distances much greater than the Rayliegh length in vacuum.

2.2 Laser Wakefield Acceleration

A laser wakefield accelerator is generated when a laser pulse interacts with an underdense plasma, driving a plasma wave, and accelerating trapped electrons. Through the ponderomotive force, eqn. 2.15, electrons are pushed radially away from the laser pulse and driving a plasma density wave following the laser pulse with a velocity $v_p = \frac{\omega_p}{k_p} = v_g = c\left(1 - \frac{\omega_p^2}{\omega_0^2}\right)^{1/2}$, where v_p is the plasma wave velocity, k_p is the plasma wave number, and v_g is the group velocity of the laser pulse [2]. We can begin describing the laser wakefield

accelerator in the simplest case using a 1D linear regime. We start by assuming a sinusoidal plasma density perturbation as follows:

$$\frac{\delta n_e}{n_e} = \delta sin(k_p x - \omega_p t) \tag{2.19}$$

where $0 < \delta < 1$, and k_p is the plasma wave number. We can then plug this into Poisson's equation:

$$\nabla E = \frac{\rho}{\epsilon_0} = -\frac{e n_e \delta}{\epsilon_0} sin(k_p x - \omega_p t) \tag{2.20}$$

where $\rho = -e\delta n_e$. We then integrate to give:

$$E = \frac{e n_e \delta}{\epsilon_0 k_p} cos(k_p x - \omega_p t) \tag{2.21}$$

and simplifying by using the plasma frequency definition, $\omega_p^2 = \frac{n_e e^2}{m_e \epsilon_0}$, gives:

$$E = \frac{m_e \omega_p c}{e} cos(k_p x - \omega_p t) \tag{2.22}$$

which gives a maximum electric field value of:

$$E_{max} = \frac{m_e \omega_p c}{e} \tag{2.23}$$

While this description of the wakefield is in a simple 1D linear regime, it provides a good understanding of the maximum electric field gained from a sinusoidal electron density perturbation. The maximum electric field can also offer a quick means of calculating the maximum electron energy a simple linear wakefield can provide. For example: an electron accelerated in the electric field created by a plasma density of $n_e = 1 \times 10^{18}$ cm^{-3} over a

length of 1 mm is 97 MeV, assuming the electric field is at maximum for the 1 mm length. One limit to the maximum energy an electron can gain from a LWFA is the dephasing length L_d, which defines the maximum length an electron can travel before out running the accelerating electric field. For the linear wakefield presented above, the density wave and electric field are π out of phase. This means an electron can travel half the length of the plasma wavelength λ_p before it begins to lose energy to the decelerating area of the electric field, $k_p(L_d - v_p t) = \pi$ and $L_d = \frac{\lambda_p}{2(1-v_p/c)}$.

The laser wakefield accelerator can be expended upon to a 3D linear regime ($a_0 << 1$) using cold fluid equations equations given by [3]:

$$\left(\frac{\partial^2}{\partial t^2} + \omega_p^2\right)\frac{\delta n}{n_e} = \frac{c^2\nabla^2 a_0^2}{2} \tag{2.24}$$

and

$$\left(\frac{\partial^2}{\partial t^2} + \omega_p^2\right)\phi = \frac{\omega_p^2 a_0^2}{2} \tag{2.25}$$

where $\frac{\delta n}{n_e}$ is the normalized density perturbation, and ϕ is the electrostatic wake potential. Solutions to these equations describe the wakefield energy and density for $a_0 << 1$ and $E << E_0$ where $E_0 = \frac{m_e c\omega_p}{e}$ is given by [3]:

$$\frac{\mathbf{E}}{E_0} = -\frac{c}{2}\int_0^t dt' sin(\omega_p(t-t'))\nabla a_0^2(\mathbf{r}, t') \tag{2.26}$$

$$\frac{\delta n}{n_e} = \frac{c^2}{2\omega_p}\int_0^t dt' sin(\omega_p(t-t'))\nabla^2 a_0^2(\mathbf{r}, t') \tag{2.27}$$

These solutions indicate that for the linear regime of wakefield acceleration the plasma density wave and energy can be described with a simple sinusoidal oscillation at the plasma frequency. Additionally, for the laser pulse to maximize efficiency in wake generation, the

laser pulse must be on the order of the plasma wavelength and the radius is on the order of the laser spot size.

In practice, operating in the linear regime of laser wakefield acceleration offers the benefit of having an easily control-able interaction over long propagation distances (few cm), but requires electron injection schemes to trap and accelerate electrons. A far more common method of laser wakefield acceleration is that of the non-linear regime where $a_0 >> 1$ and can no longer be described by cold fluid equations. Instead the nonlinear case of LWFA is primarily studied using particle in cell simulations of the laser plasma interaction. In the nonlinear regime of LWFA, the plasma density and electric fields can no longer be described with a simple sinusoidal oscillation and instead have steep nonlinear gradients. Additionally, the nonlinear regime offers a self-injection [32] method of trapping and accelerating electrons through wave breaking [21].

For an electron to become trapped in a wakefield, there is a minimum and maximum electron momentum which is dependent upon the electron velocity and the plasma wave potential ϕ_p. The electron momentum needed for trapping in a wake potential is given by [3]:

$$\mathbf{p_m} = \gamma_p \beta_p (1 + \gamma_p \Delta\phi_p) \pm \gamma_p \left[(1 + \gamma_p \Delta\phi_p)^2 - 1 \right]^{1/2} \tag{2.28}$$

where $\Delta\phi_p = \phi_{max} - \phi_{min}$ and $\phi_{min,max}$ are the minimum and maximum of the wake potential. Initially the electron energy will be out run by the plasma wave, slipping backward with respect to the plasma wave frame. However, if the electron gains enough velocity upon reaching the correct phase of the plasma wave ($\psi \rightarrow -\pi$), determined by eqn. 2.28, the electron will be trapped and accelerated in the plasma wave. This trapping, which is dependent upon the electron velocity and plasma wave electric fields, are described in the phase space separatrix found in [3]. Electrons which have too low momentum upon

reaching $\psi \rightarrow -\pi$ will continue to be overtaken by the plasma wave and electrons with too high a momentum will outrun the wave.

2.2.1 Blowout Regime

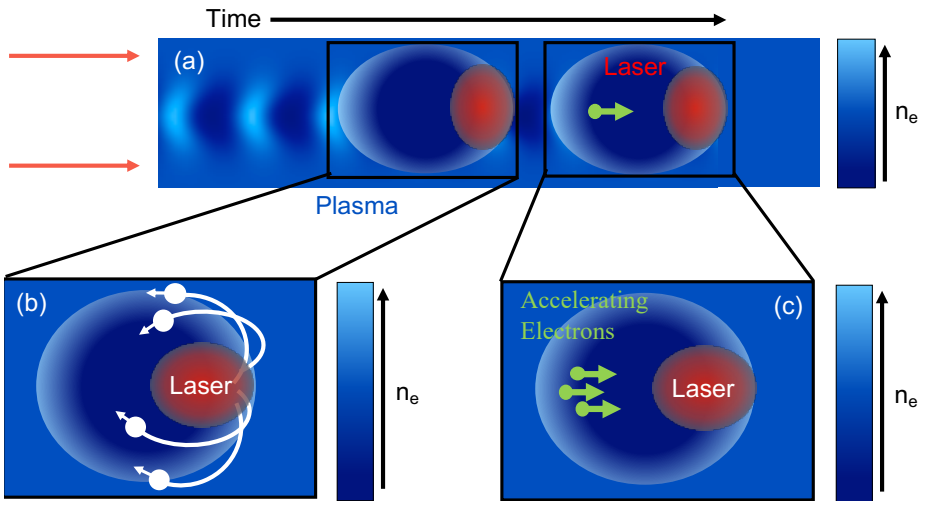

Figure 2.1: (a) Shows the formation of a LWFA in the blowout regime highlighting the formation of the electron free cavity and the trapping of electrons. (b) Shows electrons being expelled radially due to the ponderomotive force of the laser pulse. (c) Highlights the trapping and acceleration of electrons in the electron free bubble caused by the laser pulse.

The most common nonlinear LWFA regime use in university research is the blowout regime. It is the most common due to the prevalence of short pulse (< 50 fs), moderate energy (< 10 J) laser systems in university laboratories. These laser systems can easily produce $a_0 > 1$ entering the nonlinear regimes of LWFA. The blowout regime is created when a laser pulse with an $2 < a_0 < 4$ and pulse length $\simeq 1/2$ the plasma wavelength (λ_p) interacts with an underdense plasma. The laser pulse pushes electrons radially away from regions of high intensity through the ponderomotive force, fig. 2.1 (b), creating a trailing region void of electrons. The powerful, non-linear electric fields generated through the space charge separation reaches a maximum in which electrons are trapped in the blown-out region

and accelerated longitudinally, fig. 2.1 (c).

Operation in this regime can described through a series of matching conditions to allow the short laser pulse to be guided through self focusing in the plasma. By matching the laser pulse size with the plasma following the matching condition [9]:

$$k_p R \simeq k_p w_0 = 2\sqrt{a_0} \tag{2.29}$$

where k_p is the plasma wave number, R is the laser spot radius, and w_0 is the laser waist size. If this matching condition is fulfilled, the front edge of the laser pulse will locally pump deplete and etch backward allowing the remainder of the laser pulse to be self guided inside the plasma.

Through simulation work, the etching speed or pump depletion of the laser pulse is determined to follow the condition [9]:

$$L_{etch} \simeq \frac{\omega_p^2}{\omega_0^2} c\tau_{FWHM} \tag{2.30}$$

where τ_{FWHM} is the laser pulse length. The etching distance describes the distance over which the laser pulse will lose sufficient energy to no longer sustain the LWFA. Additionally, the laser pulse etching causes the wake velocity to be modified such that $v_\phi = v_g - v_{etch}$ where v_g is the group velocity, and v_{etch} is the etching velocity. This modification to the velocity causes the wake to move slower than the group velocity which in turn allows accelerating electrons to outrun the wake. This distance, the dephasing length, dictates the maximum distance an electron will gain energy from the wake and is given specifically for the blowout regime by [9]:

$$L_d \simeq \frac{2\omega_0^2}{3\omega_p^2} R \tag{2.31}$$

Considering these limitations on how much energy a trapped electron can gain from the wake, we can then determine a simple formula for how much energy to expect from such an accelerator. Consider the formula:

$$\Delta E = qE_{wake}L_d \tag{2.32}$$

where E_{wake} is the average accelerating electric field, and $L_d > L_{etch}$ so that electrons gain the maximum energy before the laser has pump depleted. The maximum energy gained during this acceleration has been determined through simulation studies and is given by [9]:

$$\Delta E \simeq 1.7 \left[\frac{P}{100}\right]^{1/3} \left[\frac{10^{18}}{n_e}\right]^{2/3} \left[\frac{0.8}{\lambda}\right]^{4/3} \tag{2.33}$$

where P is the laser power given in TW, n_e is the electron number density given in cm^{-3}, and λ is the laser wavelength in μm. This engineering formula for the maximum energy gain shows that for currently available laser powers, energies of more than a GeV are realistically obtainable in very short distances.

The resulting accelerated bunch of electrons gain the majority of their energy due to the longitudinal electric fields and are guided in a channel with a similar size to that of the laser spot size, assuming matching conditions have been followed. This small angular spread causes the resulting electron beam to be very low divergence, mrad scale, and very small source size, μm scale.

2.2.2 Direct Laser Acceleration

During the acceleration process in the blowout regime of LWFA, there is no overlap of the driving laser pulse with the accelerating electron bunch, fig. 2.2 (a), due to the matching conditions to operate efficiently. However, schemes in which the electron bunch does overlap with a laser pulse, for example the self-modulated laser wakefield acceleration regime, by

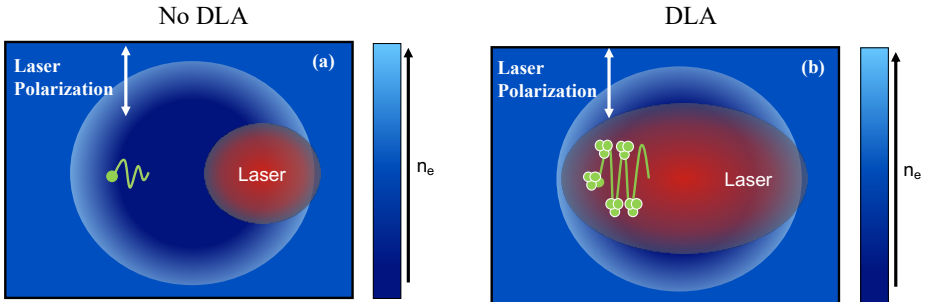

Figure 2.2: (a) Shows that DLA cannont occur when the laser pulse does not overlap the accelerating electrons, typical in the blowout regime of LWFA. (b) Shows that by alongating the laser pulse, the electrons now experience DLA and bunch up along the extremes of the transverse oscillation.

adding a 2nd trailing laser pulse or stretching the laser pulse to create overlap, will introduce an additional acceleration mechanism called direct laser acceleartion (DLA), fig. 2.2 (a).

Electrons which are trapped off axis in a LWFA will undergo transverse oscillations at the betatron frequency ($\omega_\beta = \frac{\omega_p}{\sqrt{2\gamma}}$)caused by restorative forces in the wake. These restoring forces are caused by the high negative charge at the transverse boundary of the wake and the positive charge of the near stationary ions in the wake. The restoring force in a blown out cavity, like that of a wake in an LWFA, can be obtained through Gauss's law as follows:

$$\phi_E = \frac{Q_{enc}}{\epsilon_0} \tag{2.34}$$

where ϕ_E is the electric flux through a surface, and Q_{enc} is the charge enclosed by the surface. Assuming a cylindrical symmetry for the surface choice and plugging in for the enclosed charge:

$$E \cdot dA = \frac{Q_{enc}}{\epsilon_0} \tag{2.35}$$

$$\Rightarrow E \cdot 2\pi r_\perp l_c = \frac{-en_e(\pi r_\perp^2 l_c)}{\epsilon_0} \tag{2.36}$$

$$\Rightarrow E = \frac{-en_e r_\perp}{2\epsilon_0} \tag{2.37}$$

where $r_\perp$ is the radius from the center of the wake, and l_c is the length of the imaginary cylinder. Using the definition of the plasma frequency and coulomb force, $F = qE$, we derive a simple equation for the restoring force of the plasma wake:

$$\mathbf{F}_{res} = -\frac{m_e}{2}\omega_p^2 \mathbf{r}_\perp \tag{2.38}$$

where $\mathbf{r}_\perp$ is the electron vector pointing from the laser axis. Electrons which are trapped off axis will be attracted to the axis of blown out region due to the positive charge, over shoot, and be repulsed by the negative charge at the edge of the boundary with strength described by eqn. 2.38. This restoring force equation shows that by increasing the plasma density, the forces causing the electrons to oscillate will similarly increase as $F_{res} \propto \omega_p^2 \propto n_e$. However, due to the plasma wave size being inversely proportional to the plasma density, $\lambda_p \propto n_e^{-1/2}$, the electron oscillation radius must remain less than the plasma channel radius, R, or it will be expelled from the channel $\mathbf{r}_\perp < R$.

Electrons oscillating at the betatron frequency will gain energy directly from an overlapping laser electric field as long as a resonance condition is met. The resonance condition for an electron oscillating at the betatron frequency and overlaping with a laser electric field is given by:

$$N\omega_\beta = \left(1 - \frac{v_{||}}{v_\phi}\right)\omega_0 \tag{2.39}$$

where N is an integer denoting the harmonic of the betatron frequency, $v_{||}$ is the longitudinal velocity of the electron, and v_ϕ is the phase velocity of the laser. Electrons oscillating in the transverse direction at the betatron frequency following this resonance condition will experience a net gain in energy from the laser electric field. This is because the laser pulse will overtake the electron by one full period of oscillation in the time it takes the electron to complete one oscillation, causing the electron to remain in the accelerating field rather than gaining and losing energy equally.

However, as introduced in the LWFA section through laser etching, the laser frequency evolves throughout its propagation through the wakefield, making the RHS of eqn. 2.39 change as a function of time. Additionally, the betatron frequency will change due to the electrons gaining energy from the wake electric field and the betatron frequency depending on γ. Therefore, an electron which begins oscillations matching the resonant matching condition will quickly become out of phase with the evolving laser frequency. Simulation studies have shown that electrons will undergo complex, discrete "slips" and "jumps" in frequency after losing energy to the laser electric field until all energy gain has been lost or the electron regains the resonance condition at a new matching condition, as shown in [33, 34, 35], and continue to gain energy in the regions where the resonance condition is met.

The work done by the transverse laser electric field is then calculated by [35]:

$$W_\perp = -q \int_0^t dt' E_\perp \cdot v_\perp \tag{2.40}$$

where $E_\perp$ is the transverse laser electric field, and $v_\perp$ is the transverse velocity of the electrons. The work done on an accelerating electron through this mechanism will be positive, energy gained, so long as the electric field or the electron velocity are negative. Additionally, this work calculation shows that the energy gained by the electron scales as a function of the transverse velocity which is primarily caused by the restoring force in the

wake. Therefore, the energy gained through DLA, assuming the resonance conditions are maintained, will scale as a function of plasma density, n_e, as well as the laser electric field.

For electrons in betatron oscillation in a LWFA plasma wave, the net effect is shown to be a positive energy gain [35]. The additional energy gained through DLA increases the radius of the electron oscillation, similar to the diagram in fig. 2.2 (b), due to the increased transverse momentum gained through interaction with the transverse laser electric field. This transverse momentum also increases the electron divergence along the laser polarization axis as explored in [33, 35].

Due to the larger radius of oscillation, electrons which gain an energy enhancement through DLA will have a larger divergence upon exiting the accelerator and, when dispersed in energy, a "forking" feature has been observed in high energy electrons where DLA dominates [35, 36]. This forking feature occurs parallel with the laser polarization due to electrons oscillating in this plane gaining additional transverse momentum from the electric field which is then converted to a higher longitudinal energy through $\mathbf{v} \times \mathbf{B}$. Additionally, due to the larger oscillation radius, electrons will spend more time at the extremes of these oscillations causing a higher density of electrons to maintain the enhanced transverse momentum upon exiting the accelerator. The electrons will also "bunch" at these extremes due to the axial ponderomotive force, similar to effects seen in free electron lasers (FEL) [37]. This combination of enhanced transverse momentum and bunching along the extremes creates the forking features observed experimentally.

This forking features and contribution of DLA will be explored further in Chatper 4.

2.2.3 Self-Modulated Regime

As mentioned in the introduction, large laser facilities do not, currently, have access to short pulse laser systems capable of operating in the blowout regime of LWFA. Instead, these facilities have high energy (> 150 J), long pulse (> 500 fs) laser systems integrated

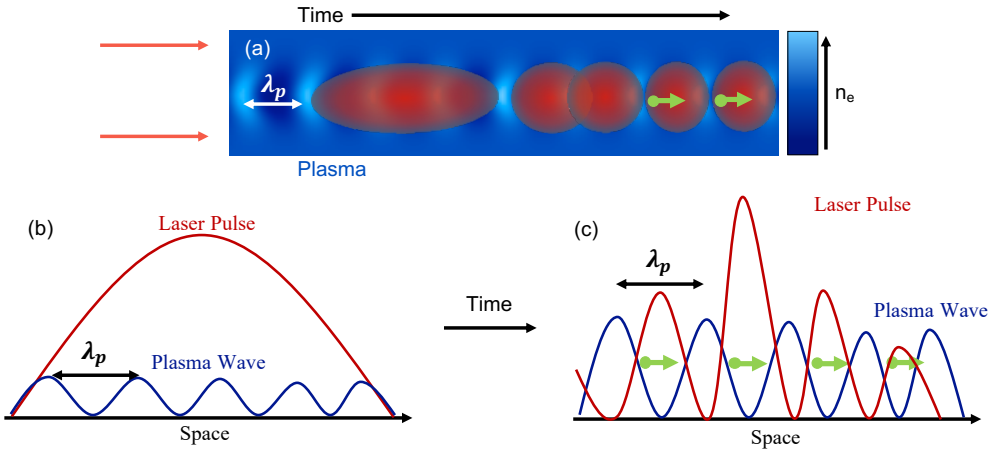

Figure 2.3: Schematic detailing the formation of a SM-LWFA. As the laser pulse propagates through the plasma, it begins to modulate due to Raman and self-modulation instabilities at the plasma frequency until wave breaking in which electrons are trapped and accelerated.

with their facilities. These laser systems are ideal for driving a regime of LWFA called the self-modulate regime.

To operate in the self-modulated regime, the drive laser pulse must have a length greater than that of the plasma wavelength ($\tau >> \lambda_p$). The transverse self-modulation instability resembles the Raman forward scattering instability, which is a longitudinal effect, and occurs simultaneously. Raman scattering is a laser plasma instability which follow the below matching conditions [38]:

$$\omega_0 = \omega_R \pm n\omega_p \tag{2.41}$$

$$k_0 = k_R \pm nk_p \tag{2.42}$$

Electrons in the plasma will scatter off an incident photon and radiate a scattered photon given these matching conditions 2.412.42. The scattered light will then interfere with

an incident electron causing a resonant variation to the laser pulse. The resonant variation is in phase with the plasma density perturbation, δn_e, which increases the amplitude of the scattered light wave, driving an unstable interaction in which the density perturbation and scattered light wave grow in amplitude [38]. Figure 2.4 shows an experimentally measured laser spectra after it has driven a SM-LWFA. The measurement was done using an imaging spectrometer where the central wavelength was aligned off the ccd camera to prevent saturation. This plot has three separate shots under identical laser and plasma conditions each showing intensity peaks at harmonics of the plasma frequency. This measurement is an indication of operating in the SM-LWFA regime due to the characteristic laser modulations caused by Raman scattering.

In 2D self-modulation occurs from the periodic plasma wave generated which creates localized regions of focusing and diffraction causing the laser pulse to break up into a train of smaller pulses and drives multiple wakes [3]. The feedback loop created through the self-modualtion and Raman instabilities occur until a maximum plasma amplitude is reached and wave breaking occurs [21]. Electrons are then injected into the plasma wave and accelerated due to space charge separation in the plasma wave. Fig. 2.3 shows a diagram of this process in 1D and 2D.

Similar to the blow-out regime, a SM-LWFA requires the driving laser pulse to be self guided in the plasma by having a power greater than the critical power of the plasma, $P > P_{crit}$. Additionally, since the SM-LWFA doesn't require the laser pulse to be shorter than the plasma wavelength like that of the blowout regime, operation at higher plasma densities ($> 10^{18}$ cm^{-3}) to increase the electric field strength is more easily achievable. The electron dephasing length is shorter at high plasma densities, aiding in the spread of electron energies typical in a SM-LWFA. The broadband electron energy spectrum produced in a SM-LWFA can be attributed to the continual process of trapping and dephasing in the shorter plasma wavelengths. This broadband electron energy spectrum can be approximated using a two

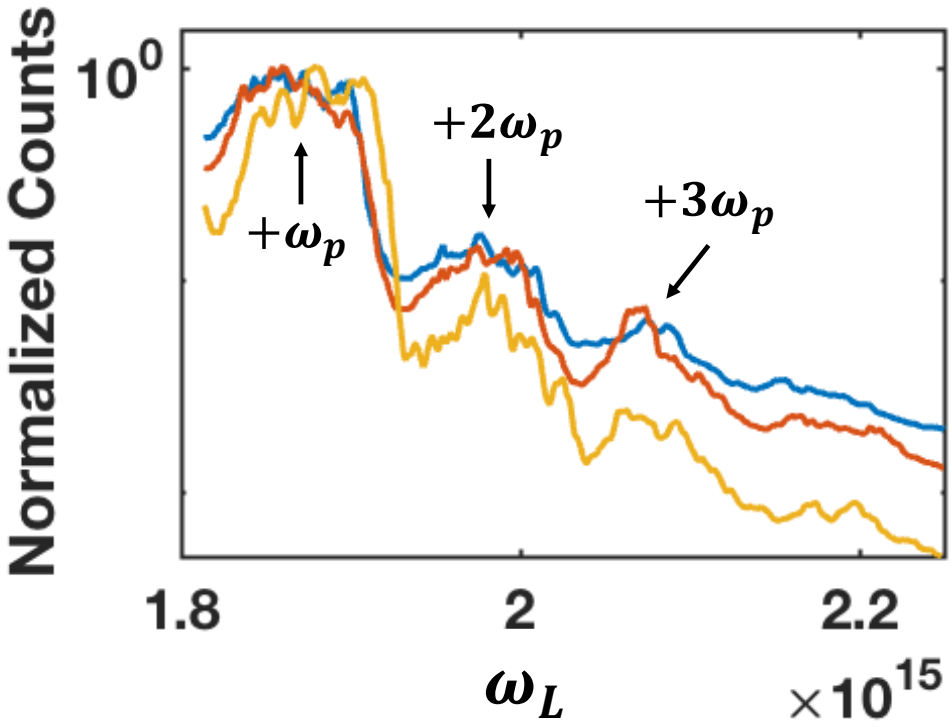

Figure 2.4: Three experimental measurements of the drive laser frequency modulations caused by Forward Raman Scattering. Each curve is a separate laser shot under identical laser and plasma conditions.

temperature exponential fuction: $C_1 e^{-\frac{E_e}{T_1}} = C_2 e^{-\frac{E_e}{T_2}}$, where $C_{1,2}$ are constants defining the amplitude, E_e is the electron energy, and $T_{1,2}$ are the temperatures. The first temperature distribution can be attributed to the wake acceleration caused by the longitudinal electric field in the plasma wave. The second temperature arises from DLA contributions to the high energy electrons.

Due to the long laser pulse used to drive a SM-LWFA, DLA will play a prominent role in the net electron energy gain. Electrons which are trapped off axis of the accelerator will undergo oscillations in the transverse direction caused by restoring forces in the plasma, eqn. 2.38. These oscillations are then converted to a longitudinal energy gain through DLA,

eqn. 2.40 of the overlapping laser pulse. This interplay in acceleration is explored further in chapter 4. The transition energy between the two temperatures is complex and will vary as a function of: 1) plasma density, which scales the size of the plasma wave and determines the strength of both the wake electric field strength and the restoring forces; 2) laser electric field, which determines how much energy can be gained through DLA as well as the plasma wave; 3) Accelerator length, which will determine how many electrons reach the dephasing limit and determine if DLA is maximized. However, a review of experimental results show the transition region to be 75 to 100 MeV for three very different experimental configurations: $\approx$ 80 MeV in a quasi-blowout regime [35], $\approx$ 100 MeV for a high density, high a_0 regime [33], and 70 MeV for a low density SM-LWFA [36]. These results suggest the transition from wake dominated electron acceleration to DLA dominated acceleration is a reasonably stable transition. For extreme parameter changes, like a very high a_0 from a multi-petawatt laser, DLA is expected to dominate at much lower energies due to the ponderomotive force causing ion channel formation much sooner in the accelerator.

The advantages of using a SM-LWFA is due to fewer laser and plasma matching conditions for effective operation and enhanced charge due to trapping electrons in multiple plasma periods. In general terms, the blow-out regime accelerates 10s of pC of charge, whereas the SM-LWFA has deomnstrated beams of electrons containing 10s to 100s of nC [1]. Similar to the blowout regime, the resulting accelerated beam of electrons will have a small (mrad scale) divergence, and a temporal size similar to that of the driving laser pulse.

Chapter 3

X-ray Sources from Laser Plasma Accelerators

3.1 X-ray Generation Mechanisms

The previous chapter discusses the way in which electrons are aceelerated using underdense laser plasma acceleration. This chapter will focus on how to generate high energy photons using these relativistic electron beams. At the most basic level, an electron undergoing an accelerating force will emit a photon to release energy. This idea is expanded upon through various x-ray generation mechanisms. Betatron radiation, for example, is generated when relativistic electrons oscillate transversely within a LWFA plasma. These oscillations cause the electron to emit photons as a means of releasing energy during the deceleration process. Increasing the strength of the oscillation driver as well as starting with a higher energy electron will, in general, increase the emitted photon energy. The greater the number of oscillating electrons, the greater the number of emitted photons.

In general, the photon spectrum emitted along the observation direction $\vec{n}$ given an electron acceleration $\dot{\vec{\beta}}$, velocity $\vec{\beta}$, and position $\vec{r}$ is derived through the Lienard-Wiechert potentials resulting in [39]:

$$\frac{d^2I}{d\omega d\Omega} = \frac{e^2}{16\pi^3\epsilon_0 c}\left|\int_{-\infty}^{\infty} e^{i\omega(t-\vec{n}\cdot\vec{r}/c)}\frac{\vec{n}\times[(\vec{n}-\vec{\beta})\times\dot{\vec{\beta}}}{(1-\vec{\beta}\cdot\vec{n})^2}dt\right|^2 \tag{3.1}$$

which describes the energy radiated per frequency $d\omega$ per solid angle $d\Omega$. There are several general statements that can be made about an electron emitting a photon given this equation. The first is that for an electron experiencing no acceleration, $\dot{\vec{\beta}} = 0$, no

radiation will be emitted. Additionally, the term $\frac{1}{(1-\vec{\beta}\cdot\vec{n})^2}$ indicates maximum emission when the electron is relativistic and travelling parallel to the observation axis, i.e. $\vec{\beta}\cdot\vec{n} \to 1$. These qualitative remarks are especially useful due to the electron source from an LWFA are relativistic and have mrad divergence along the beam axis. The LWFA driven electron beams are then, qualitatively, a valuable tool for x-ray generation.

In this chapter we will explore the main three methods we have explored to generate x-rays using the relativistic electron beams generated in a SM-LWFA. We will first explore the Betatron mechanism which generates x-rays through transverse forces in a plasma channel during the acceleration process in a SM-LWFA. The Inverse Compton Scattering mechanism produces x-rays through electron oscillations in an intense laser field. Finally, bremsstrahlung radiation is produced through scattering events with the nuclei of a high-Z target.

3.2 Betatron Radiation

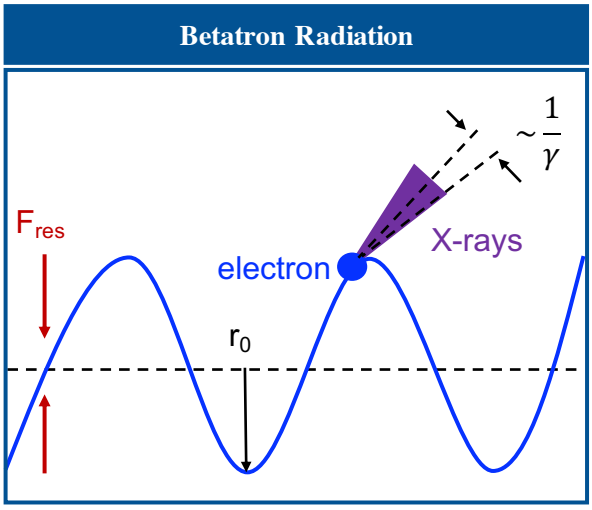

Figure 3.1: Diagram of betatron radiation. Betatron radiation occurs during the acceleration process in a LWFA. Electrons which are trapped off axis oscillate in the transverse direction, due to restoring forces of the plasma wave, and emit high energy photons.

Betatron radiation is emitted by electrons oscillating in the transverse direction during the acceleration process in a LWFA caused by restoring forces described in eqn. 2.38 and shown in fig. 3.1. In the absence of longitudinal acceleration, this motion can be described in the simplest case as a harmonic oscillator of the form:

$$\frac{d^2x}{dt^2} = -\frac{1}{2}\omega_p^2 x \tag{3.2}$$

where oscillations are purely driven by the restoring forces of the wake. We can then derive the betatron frequency by introducing relativistic mass effects which slow the oscillation $\omega_p^2 \rightarrow \frac{\omega_p^2}{\gamma}$, where $\gamma = (1 - \frac{v^2}{c^2})^{-1/2}$ is the lorentz factor. We then apply this relativistic correction to the frequency of eqn. 3.2 to get the betatron frequency:

$$\omega_\beta = \frac{\omega_p}{(2\gamma)^{1/2}} \tag{3.3}$$

Eqn. 3.2 also provides solutions to the electron position and velocity ignoring longitudinal acceleration as follows:

$$x = x_0 sin(\omega_\beta t) \tag{3.4}$$

$$v = x_0 \omega_\beta cos(\omega_\beta t) \tag{3.5}$$

An electron oscillating in the restoring electric field as described will emit photons with a wavlength similar to $\lambda_\gamma \simeq \frac{\lambda_\beta}{2\gamma^2}$, where $\lambda_\beta = \frac{2\pi c}{\omega_\beta}$ [40]. The factor of $2\gamma^2$ comes from the conversion of lab frame to electron frame and back to the lab frame for the emitted radiation. For electron energies typical in a LWFA this scaling indicates high photon energies are easily accessible to moderate laser systems. For a 25 MeV electron, the betatron wavelength is $\lambda_\beta \approx 300\mu$m which is much shorter than mm scale magnetic undulators.

For very high wiggler strengths ($K >> 1$)) where $K = \gamma k_\beta r_0$, the emitted photon spectrum becomes broadband and must be described using a more complex picture which includes the longitudinal components to the equation of motion. The coupled equations of motion in the wave propagation direction, z, are given by [41] to be:

$$\beta_z \simeq \beta_{z0}\left(1 - \frac{k_\beta^2 r_\beta^2}{4}\right) - \beta_{z0}\left(\frac{k_\beta^2 r_\beta^2}{4}\right) cos(k_\beta ct) \tag{3.6}$$

$$\mathbf{z} \simeq z_0 + \beta_{z0}\left(1 - \frac{k_\beta^2 r_\beta^2}{4}\right) ct - \beta_{z0}\left(\frac{k_\beta^2 r_\beta^2}{8}\right) sin(k_\beta ct) \tag{3.7}$$

where $\beta = \mathbf{v}/c$ and r_β is the electron radius.

To calculate the energy distribution of emitted photons per frequency per solid angle we can calculate the integral in eqn. 3.1. For short pulse duration and emission along the observation axis, the electron trajectories can be approximated over small arcs. This integration is given by [39] and results in the general solution for power radiated per frequency per solid angle of a single electron as:

$$\frac{d^2 I}{d\omega d\Omega} = \frac{e^2}{3\pi^2 c}\left(\frac{\omega\rho}{c}\right)^2 \left(\frac{1}{\gamma^2} + \theta^2\right)^2 \left[\mathbf{K}_{2/3}^2(\xi) + \frac{\theta^2}{(1/\gamma^2 + \theta^2)}\mathbf{K}_{1/3}^2(\xi)\right] \tag{3.8}$$

where $\rho = \frac{c^2}{\dot{v}_\perp}$, $\dot{v}_\perp$ is the transverse electron velocity, $\xi = \left(\frac{\omega}{\omega_c}\right)(1 + \gamma^2\theta^2)^{3/2}$ where ω_c is the critical frequency of betatron emission, and $\mathbf{K}$ are modified bessel functions. The critical frequency $\omega_c \simeq 3K\gamma^2\omega_\beta$ is the frequency at which the emitted spectrum is peaked. We can then define the critical energy as the point at which half the energy of a spectrum resides, which is given in practical units by:

$$E_c[keV] = 5 \times 10^{-24}\gamma^2 n_e[cm^{-3}] r_0[\mu m] \tag{3.9}$$

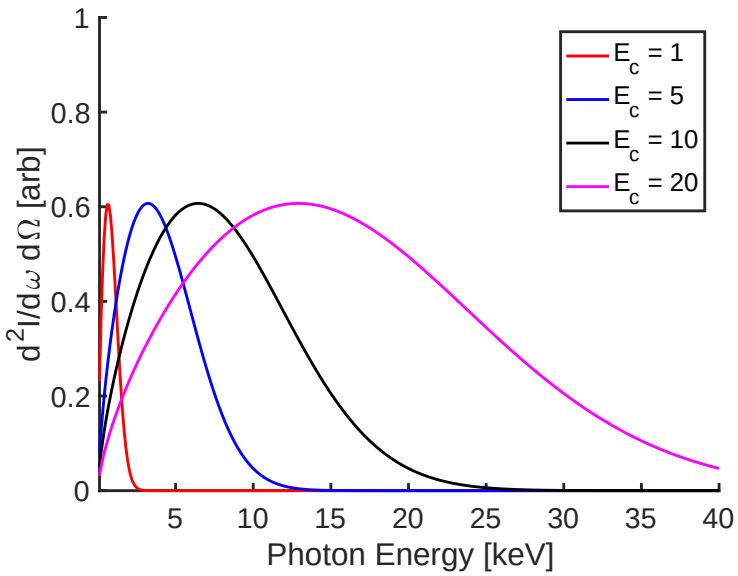

Figure 3.2: Plot of eqn. 3.10 for different critical energies E_c.

The γ of an electron can be quickly calulated using the approximate form $\gamma = \frac{E_e}{m_e c^2}$, where E_e is the energy of the electron, and $m_e c^2$ is the electron rest mass in units of energy. Due to the E_c of the betatron radiation being dependent upon the radius of electron

oscillation, to maximize the energy one seeks to increase the radial size of the LWFA or enhance this radius through transverse electric fields, DLA. In addition, due to the added DLA component during acceleration, the SM-LWFA has been shown to produce betatron radiation with a critical energy of 10 keV and photon number $> 10^9$ photons/ev/Sr [19]. Since the electron oscillations are constrained in size by the LWFA plasma channel forces and the angular spread of the emitted radiation scaling as $\theta \approx 1/\gamma$, this method of x-ray generation has a very small source size (10s of μm scale). It has been measured to be below 40 μm in the SM-LWFA regime and smaller still in the blowout regime at lower plasma densities.

Due to the broadband electron energy spectrum produced in a SM-LWFA and the broadband emission typical for wiggler strengths $K >> 1$, the betatron radiation from a SM-LWFA, similarly, follows a broadband energy distribution. This broadband distribution is given approximately by:

$$\frac{d^2I}{dEd\Omega} \propto \left(\frac{E_\gamma}{E_c}\right)^2 K_{\frac{2}{3}}^2\left(\frac{E_\gamma}{E_c}\right) \tag{3.10}$$

where eqn. 3.8 has been reduced by assuming on axis radiation $\theta = 0$. Here E_γ is the photon energy, and $K_{\frac{2}{3}}$ is the modified bessel function. This distribution is broadband following the electron energy distribution and decays exponentially after the critical energy. An example of this equation is plotted in fig. 3.2 for 4 different values of E_c. This plot shows that for higher E_c the emitted spectrum shifts to higher energies and broadens in energy distribution. The total number of photons emitted depends upon the number of electrons undergoing oscillations and for how many oscillations. The average number of photons emitted per electron per oscillation is $N = \frac{5\pi}{\sqrt{3}\gamma\alpha}$, where α is the fine structure constant. Therefore, to maximize emitted photon number, higher charge and energy in the electron source is desirable. For this reason, the SM-LWFA regime is ideal due to being capable of accelerating > 10 nC of charge to relativistic energies. Due to the critical energy scaling and

decaying energy distribution, this x-ray generation mechanism provides the brightest x-ray source driven by SM-LWFA below ≈ 40 keV [1]. Above 40 keV, x-ray generation mechanisms with higher energy scaling with electron energy produce brighter sources. The first of these mechanisms is Inverse Compton Scatter.

3.3 Inverse Compton Scattering

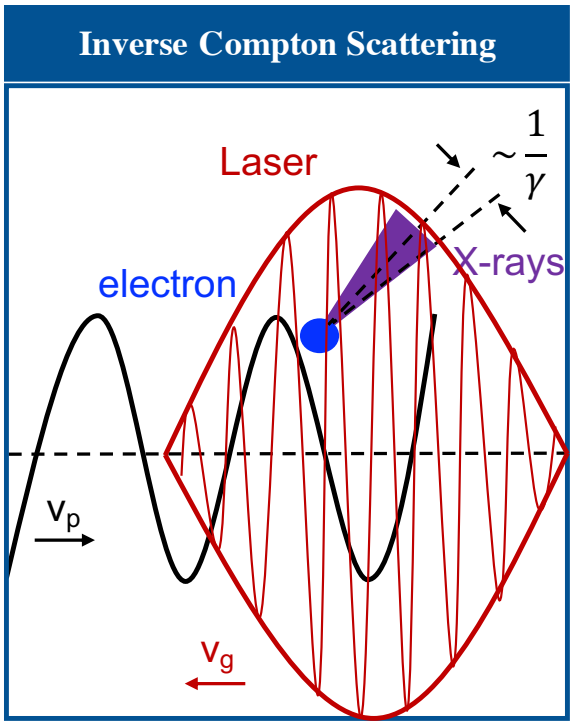

Figure 3.3: Diagram of the Inverse Compton Scattering process. Here a low energy photon collides with a relativistic electron. The photon is upshifted in energy by $\approx 4\gamma^2$, where γ is the electron lorentz factor, and emitted along the path of the high energy electron.

For applications in which higher energy x-rays than the betatron mechanism can provide, Inverse Compton Scattering (ICS) is an attractive mechanism to utilize due to the photon energy scaling with electron energy, $E_\gamma \simeq 4\gamma_e^2 E_l$ where E_l is the laser photon energy,

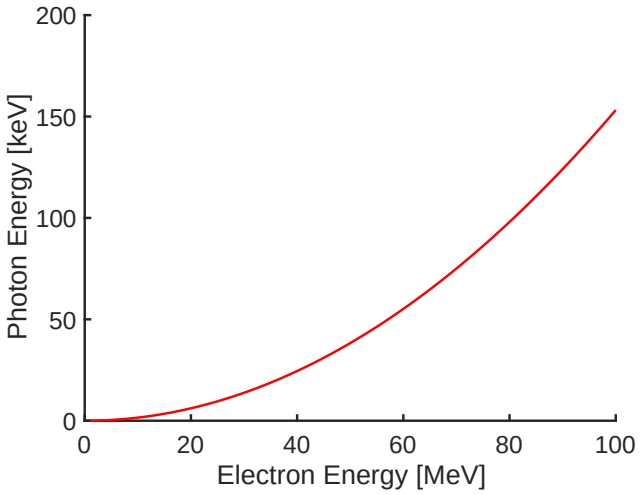

Figure 3.4: Example ICS x-ray energy scaling using equation 3.13.

for non relativistic head on collisions. ICS generates high energy x-rays through low energy photons scattering off of a relativistic electron. This scattering event causes the photon to up-shift in energy and emit along the electron propagation direction, fig. 3.3, due to relativistic conversions. The x-ray spectrum can be described generally through the Lienard-Wiechert potential 3.1 and a more complete description can be found in [4, 42]. However, first we examine the process by assuming a single electron in a non-relativistic laser field, $a_0 << 1$.

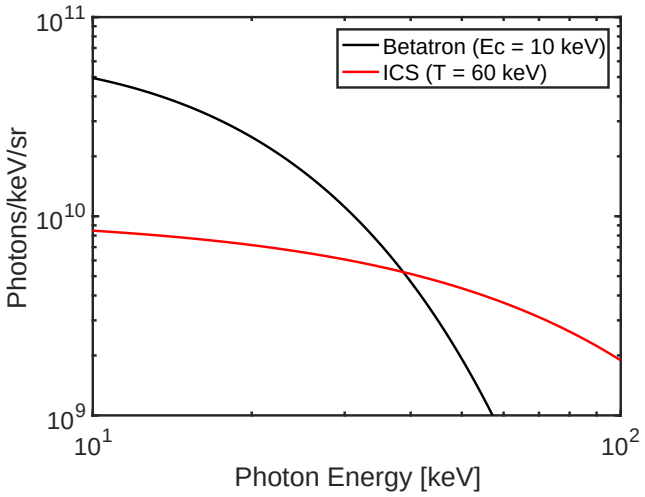

Figure 3.5: An example betatron (black) x-ray spectrum from a SM-LWFA compared with an ICS (red) x-ray spectrum. The betatron spectrum is fit using eqn. 3.10 and the ICS spectrum is fit using a single temperature exponential function, $C_1 e^{\frac{-E_\gamma}{T}}$ where E_γ is the photon energy and T is the photon temperature. A single temperature distribution for ICS is expected due to broadband electron spectrum from a SM-LWFA. Here we see a transition from betatron x-ray emission being dominante below $\approx$ 40 keV at which point ICS produces higher photon number.

Here, for relativistic electrons, $\gamma_e >> 1$ emitting radiation along the laser axis, the power

radiated per frequency per solid angle reduces to [43]:

$$\frac{d^2I}{d\omega d\Omega} \simeq r_e m_e c \left(\frac{\omega}{4\gamma_e^2 \omega_0}\right)^2 \gamma_e^2 N_0^2 a_0^2 R(\omega, \omega_0) \tag{3.11}$$

where r_e is the classic electron radius, N_0 is the number of oscillation periods, and $R(\omega, \omega_0)$ is the resonance function given by [43]:

$$R(\omega, \omega_0) = \left(\frac{sin(\mathbf{k}L/2)}{\mathbf{k}L/2}\right)^2 \tag{3.12}$$

where L is the interaction length, and $\mathbf{k} = k(1 + \gamma_e^2\theta^2)/(4\gamma_e^2) - k_0$, where k is the radiation wave number and k_0 is the laser wavenumber. In the limit where $N_0 \to \infty$ the resonance function $R \to \Delta\omega_r \delta(\omega - \omega_r)$ where $\Delta\omega_r = \omega_r/N_0$, with ω_r being the resonance frequency. This states that for interactions with many laser oscillations, i.e. a 1 ps laser pulse, a single electron of constant energy will emit at one photon energy. This causes the emitted x-ray spectrum to follow a similar energy distribution to that of the electron spectrum, which for a SM-LWFA is broadband. This, combined with the simplified energy scaling for linear scattering events ($a_0 << 1$) along the electron axis ($\theta = 0$) given by [42]:

$$E_\gamma \simeq 4\gamma_e^2 E_l \tag{3.13}$$

where γ_e is the Lorentz factor of the relativistic electron, and E_l is the lower energy photon energy, provides a simple means of approximating the ICS x-ray spectrum given an electron spectrum. This photon energy scaling with an electron distribution is shown in fig. 3.4 for several electron temperatures. This scattering process produces higher energy x-rays than that of betatron radiation due to this $\propto 4\gamma_e^2$ scaling. Whereas the betatron photon number falls off exponentially after the critical energy is reached. The ICS photons energy scaling will fall off as a function of the electron distribution itself, providing high

photon numbers at higher energy. Fig. 3.5 shows a comparison of an example betatron (black) and ICS (red) energy spectrum driven by SM-LWFA [19, 1]. The analysis methods used to generate these spectra will be discussed in chapter 5. The number of ICS photons is dependent upon the number of electrons, number of low energy photons, and the scattering cross section. For this reason, to maximize emitted photon number, the SM-LWFA shows promise due to the large amount of trapped charge and small source size. Care must be taken with the counter propagating photon source so that it overlaps with the electron beam as much as possible to increase scattering events. Similar to betatron, the source size of this x-ray production will be very small, following the size of the electron beam and photon source interaction region and emitting in $\theta \propto 1/\gamma_e$. Note, the x-ray emission will have greater divergence perpendicular to the linear laser polarization [42]. To create the most high energy photons, the electron beam size and counter propagating photon source should be matched, however the effective source size will roughly follow the smaller of the two.

Further discussion of this source will occur in Chapter 5 where ICS is generated using a SM-LWFA.

3.4 Bremsstrahlung Radiation

While ICS is capable of producing very high energy x-rays, the number of photons at high energies utilizing a SM-LWFA tends to be much lower than that of bremsstrahlung radiation. Bremsstrahlung, or breaking radiation, is created when high energy electrons are bent or deflected by the nucleus of a target material. Figure 3.6 shows the bremsstrahlung process where an electron approaches the nucleus of a target material. Due to the electric fields of the nucleus, the electron is deflected and slowed. The downshift in electron energy is emitted through a photon. Bremsstrahlung x-rays can therefore be as energetic as the input electron, though this is highly unlikely as it is more likely a single high energy electron will emit several lower energy photons. Bremsstrahlung radiation does provide a method of

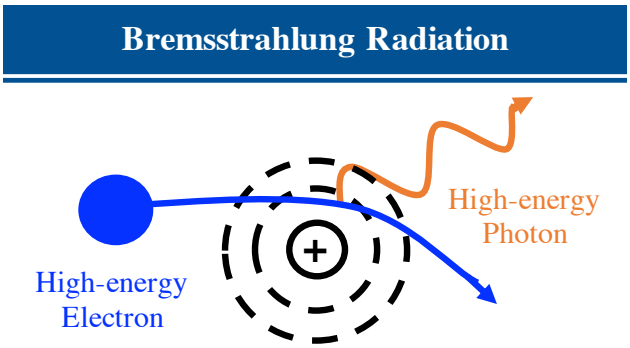

Figure 3.6: Diagram of the bremsstrahlung process. Here a high energy electron is deflected by the nucleus of a target material. The acceleration caused during this delflection produces a high enery photon to be emmitted.

producing a very high number of energetic x-rays above the capabilities of betatron and ICS.

The scattering of a charged particle in a Coulomb field for non-relatvistic cases is given by the Rutherford formula as [39]:

$$\frac{d\sigma_s}{dQ} = 8\pi \left(\frac{zZe^2}{\beta c}\right) \cdot \frac{1}{Q^3} \tag{3.14}$$

where Q is the momentum transfer $Q^2 = 2\mathbf{p}^2(1 - cos(\theta))$. This cross section is then used in the calculation for the frequency spectrum integrated over all emission angles. The differential radiation cross section is then given by [39]:

$$\frac{d^2\chi}{d\omega dQ} = \frac{dI(\omega, Q)}{d\omega} \cdot \frac{d\sigma_s}{dQ} Q \tag{3.15}$$

where $\frac{dI(\omega,Q)}{d\omega}$ is the energy radiated per frequency in a collision with momentum transfer Q. We then integrate over all momentum transfers Q:

$$\frac{d\chi}{d\omega} \simeq \frac{16Z^2e^2}{3c} \left(\frac{z^2e^2}{Mc^2}\right)^2 \cdot \frac{1}{\beta^2} ln \left(\frac{Q_{max}}{Q_{min}}\right) \tag{3.16}$$

These equations, valid for non-relativistic collisions, provides information on how the emitted bremsstrahlung spectrum will scale with experimental parameters. High Z materials are used in bremsstrahlung generation due to the Z^2 scaling of the emission spectrum. Additionally, the emitted photon energy depends on the electron momentum through the Q_{max}/Q_{min} ratio which shows a higher energy electron source will emit higher $\frac{d\chi}{d\omega}$ due to the increase in Q_{max}. A correction for the bremsstrahlung scattering cross section for highly relativistic electron interactions is given by [44]:

$$\left(\frac{d\sigma}{d(\hbar\omega)}\right)_{Born} = \frac{16}{3}\frac{Z^2 r_e^2 \alpha}{\hbar\omega}\left(1 - \frac{\hbar\omega}{E_0} + \frac{3\hbar^2\omega^2}{4E_0^2}\right)\left[ln\left(\frac{2E_0(E_0 - \hbar\omega)}{m_e c^2 \hbar\omega}\right) - \frac{1}{2}\right] \tag{3.17}$$

where relativistic energy corrections have been included. This form of the scattering cross section does not include charge screening which becomes important in highly relativistic interactions.

The angular distribution of emitted photons in both the non-relativistic, dipole emission, and relativistic, peaked along electron motion, is given by [8]:

$$\frac{d^2P}{dEd\Omega} = \frac{dP}{\hbar d\omega}\left[\frac{3}{16\pi}\frac{1}{\gamma_e^2(1 - \beta cos(\theta))^2}\left(2 + \frac{cos^2(\theta) - 1}{\gamma_e^2(1 - \beta cos(\theta))^2}\right)\right] \tag{3.18}$$

Here, for relativistic interactions $cos^2(\theta) - 1 \rightarrow 0$ which causes the angular distribution of emitted photons to be sharply peaked along the electron motion. Given a low divergence, relativistic electron beam, the emitted bremsstrahlung radiation will remain low divergence. These analytic equations show that calculating a bremsstrahlung spectrum is very difficult and calculation intensive. For this reason, Monte-Carlo simulations are relied upon for large scale calculations.

Here, we will discuss further the two methods of producing bremsstralung radiation used for work described later in this dissertation. The first is through laser-solid target inter-

actions where the laser pulse generates a population of hot electrons in the bremsstrahlung target which generate the observed radiation. The second uses a SM-LWFA to first generate a beam of relativistic electrons which then collide with a high-Z target to generate bremsstrahlung radiation.

3.4.1 Laser-Solid Target Bremsstrahlung Radiation

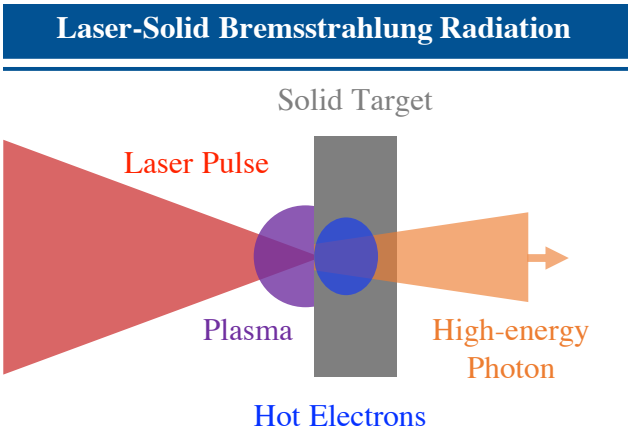

Figure 3.7: Schematic of laser-solid bremsstrahlung interaction. The laser pulse is focused onto the surface of a high-Z target generating a counter propogating plasma and producing a relatividstic electron population which travels through the solid target. The electrons undergo bremsstrahlung collisions on their path through the target emitting high-energy x-rays.

To generate bremsstrahlung radiation through a direct laser-solid interaction a laser pulse is focused directly onto the surface of a high-Z target. The laser pulse ionizes and accelerates the surface of the target through the ponderomotive force, eqn. 2.15. Due to the high density of the target, this produces a very high population of electrons. These electrons then stream through the target generating bremsstrahlung radiation. The population of hot

electrons produced inside a target is given by [45]:

$$\frac{dN_e(E_e,x)}{dE_e} = N_{el}\left[\frac{dN_e^{Oh}(E_e,x)}{dE_e}\right]/N_{elx}e^{-x/X_{el}} \tag{3.19}$$

where N_el is the number of electrons, $\frac{dN_e^{Oh}(E_e,x)}{dE_e}$ is electron energy loss due to ohmic heating inside the target, N_{elx} is the number of electrons at position x inside the target, and X_{el} is the electron mean free path. It is difficult to solve for this spectrum analytically and is frequently approximated using single and double temperature exponential distributions:

$$\frac{d^2N}{dE_e d\Omega} = Ae^{\frac{-E_e}{T_1}} + Be^{\frac{-E_e}{T_2}} \tag{3.20}$$

where A, B are constants to scale the electron yield, E_e is the electron energy, and $T_{1,2}$ are the fitted temperatures. The x-ray spectrum produced over all angles is then given by [45]:

$$\frac{d^2N_\gamma}{dE_\gamma d\Omega} = \frac{n_a N_{el}}{2\pi N_{elx}}\int_{x=0}^{X} e^{\frac{-X-x}{X_\gamma}}\left[\int_{E_e=E_\gamma}^{E_e^{max}}\frac{d\sigma}{dE_\gamma}\frac{dN_e^{Oh}}{dE_e}e^{\frac{-x}{X_{el}}}dE_e\right] \tag{3.21}$$

where n_a is Avagadros number, N_{el} is the number of electrons, N_{elx} is the number of electrons which escape the back of the target of length x, X is the position in the target, X_γ is the photon position in the target, and $\frac{d\sigma}{dE_\gamma}$ is the energy dependent cross section of the photon. This photon distribution is difficult to calculate analytically given the complexity of equations 3.19, 3.21. Therefore, the x-ray spectrum is frequently approximated using Monte Carlo simulations. It is however clear, that the number and energy of photons produced in the laser-solid interaction is dependent upon the laser energy to produce electrons, the resulting hot electron energy and number, and finally the Z and thickness of the bremsstralung target. A higher number and energy electron source will produce a higher energy and photon number using a thick high-Z target.

3.4.2 LWFA driven Bremsstrahlung Radiation

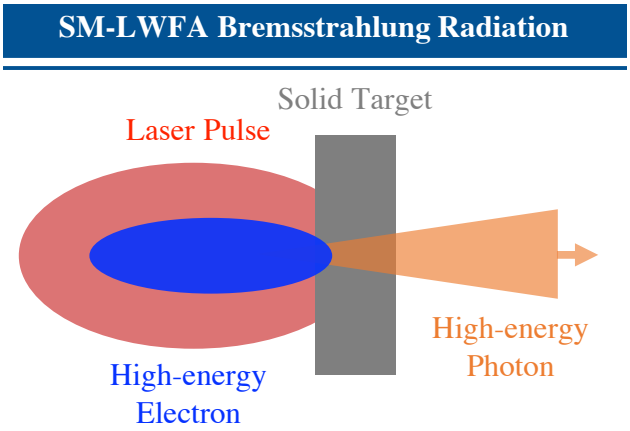

Figure 3.8: Schematic of bremsstrahlung radiation using the electron beam produced in a SM-LWFA. A high-Z target is placed at the end of the SM-LWFA where the accelerated electrons colide with the target producing bremsstrahlung radiation. Due to energy loss and beam divergence generating the SM-LWFA, the laser pulse does not contribute substantially to the bremstrahlung generation.

The method of generating bremsstrahlung radiation through SM-LWFA simply replaces the hot electron distribution found in a laser-solid interaction with the high energy electron beam produced in a SM-LWFA. The electron beam is then fired into a high-Z bremsstrahlung converter as shown in fig. 3.8. As described in eqn. 3.18,in a laser-solid interaction where the hot electron spectrum has a wide divergence, the emitted photon spectrum is emitted in $\approx 2\pi$ with a source size similar to that of the converter target. By providing a tight beam of electrons through SM-LWFA, the emitted x-ray source size is smaller due to the small size of the electron beam cross section and peaked emitted radiation described in eqn. 3.18. There is a trade off in source size vs. x-ray energy with the SM-LWFA bremsstrahlung source. By increasing target thickness more energy is extracted through bremsstrahlung producing collision, however, these collisions cause the emitted x-ray spectrum to have a greater divergence. As with the laser-solid interaction, information on

an expected bremssrahlung spectrum driven by SM-LWFA electrons relies on Monte-Carlo simulations.

Chapter 4

Simulation and Experimental Characterization of SM-LWFA

4.1 Introduction

[1] With the introduction of physical processes used in this dissertation work we turn our attention to experimental work completed to characterize the electron source produced by a SM-LWFA. As introduced in chapter 2, there are two primary acceleration mechanisms at work in a SM-LWFA, i.e. wake acceleration and DLA. This chapter will describe the work done to fully characterize the physics of the SM-LWFA and the consequences of the results. To do this we completed an experimental campaign at the Titan laser facility and through collaborators at UCLA, completed quasi-3D simulations of the experimental parameters.

When the drive laser pulse satisfies $c\tau_l > \lambda_p$ (where c is the speed of light, τ_l is the laser pulse duration and $\lambda_p = 3.3\times10^{10}(n_e)^{-\frac{1}{2}}$ [μm] is the plasma wavelength with electron density n_e [cm^{-3}]) and the plasma is under-dense ($n_e < n_c$, where n_c is the density at which the laser frequency, ω_0, equals the plasma frequency, ω_p), the laser pulse can drive relativistically propagating plasma waves through the combined action of the self-modulation and Raman forward scattering instabilities [46]. The plasma wave amplitude can become large enough

[1] This chapter contains published information from: P. M. King, K. Miller, N. Lemos, J. L. Shaw, B. F. Kraus, M. Thibodeau, B. M. Hegelich,J. Hinojosa, P. Michel, C. Joshi, K. A. Marsh, W. Mori, A. Pak, A. G. R. Thomas, andF. Albert. Predominant contribution of direct laser acceleration to high-energy electronspectra in a low-density self-modulated laser wakefield accelerator.Phys. Rev. Accel.Beams, 24:011302, Jan 2021. of which I am the first author. My contribution to this work included experimental planning, execution, data analysis, and writing the published manuscript.

to inject electrons [47] into the plasma wave and accelerate them due to the longitudinal electric field of the plasma wave [21]. Electrons injected off the main laser axis undergo transverse oscillations due to the restoring forces in the plasma wave. These transverse oscillations can be amplified by the electric field of the overlapping picosecond laser pulse and converted into a longitudinal acceleration through the $\vec{v} \times \vec{B}$ force of the laser in a mechanism known as direct laser acceleration (DLA) [48, 49, 50, 51, 35]. In this situation, the relative contributions of SM-LWFA and DLA to the final electron energy remains poorly understood.

Prior work on SM-LWFA has attributed the copious charge of high-energy electrons to self-trapping and breaking of the longitudinal plasma wave [52, 53]. Electrons with energies larger than the dephasing-limited energy gain were also observed [54, 55], but were always attributed to acceleration by the plasma wave. The role of DLA in LWFA was first suggested by Pukhov [48] and has been experimentally investigated only recently. In a quasi-blowout regime, the laser pulse was lengthened to overlap with a full plasma period, and electrons in the high-energy tail of the accelerated electron spectrum showed a fork-like splitting when dispersed perpendicular to the laser polarization direction [34, 35]. This fork-like structure was attributed to DLA through PIC simulations, but the analysis did not include the contribution of the longitudinal field from the focused laser in the DLA process.. In a high-density ($\sim 10^{20}$ cm^{-3}), short-pulse (50 fs) SM-LWFA regime, the high-energy electron beam tail was experimentally attributed to DLA [56], but without any clear experimental signature. In a long-pulse (650 fs), high-intensity ($I = 3 \times 10^{20}$ W/cm^2) regime, DLA was inferred from PIC simulations to be the main acceleration mechanism in an ion channel [33]. The role of DLA in an SM-LWFA was anticipated in a recent experiment on developing a betatron-radiation-based x-ray source, but no direct experimental evidence for DLA was presented in that work [19, 57].

In this paper [36] we show experimental evidence, verified with quasi-3D particle-in-

cell (PIC) simulations using OSIRIS [58, 59], that DLA occurs concurrently with SM-LWFA but is the dominant contributor to the highest-energy electrons in the low-density ($\omega_p \ll \omega_0$) regime of SM-LWFA, where the laser power—although it is greater than that needed for relativistic self-focusing—is insufficient to produce a totally evacuated ion channel inside the laser pulse. Our experimental work shows that, for a low plasma density ($\omega_0/\omega_p = 57$) and a 1-μm, nominally 1-ps laser with moderate amplitude $a_0 = 8.5 \times 10^{-8}\lambda I^{1/2} \approx 2.2$, the accelerated electrons exhibit a two-temperature distribution. Here a_0 is the normalized vector potential and λ [nm] is the laser wavelength. Full-scale quasi-3D PIC simulations confirm that the longitudinal field of the plasma wave excited by the SM-LWFA process mainly contributes to the low-temperature portion of the spectrum, whereas DLA is the dominant acceleration mechanism for the high-energy (temperature) electrons. When the electrons are dispersed orthogonally to the laser polarization direction, a fork-like structure [35] characteristic of DLA is observed for electrons with energies above 60 MeV. This is the first direct experimental characterization, confirmed by quasi-3D PIC simulations, of DLA in an SM-LWFA in the picosecond, high-energy regime relevant to HEDS experiments.

4.2 Experimental Results

4.2.1 Experimental Configuration and Methods

We conducted the experiment on the Titan laser system at Lawrence Livermore National Laboratory (Fig. 4.1). Titan, a $0.7^{+0.3}_{-0.1}$ ps, 120 J, Nd:Glass laser, was focused with an $f/10$ off-axis parabolic mirror into a 10-mm, supersonic He gas jet with electron density $n_e = 3 \times 10^{17}$ cm^{-3} (measured using interferometry). This configuration created peak laser intensities reaching $I = 6.4 \times 10^{18}$ W/cm^2, in a spot with 50% of the total energy contained in a 30-μm radius. The ratio $P_{\text{peak}}/P_{\text{crit}} \approx 1.6$, where P_{peak} is the peak laser power and $P_{\text{crit}} = 17 \times 10^9 \left(\frac{\omega}{\omega_p}\right)^2 = 56$ TW is the critical power for relativistic self-focusing in the plasma [3, 9].

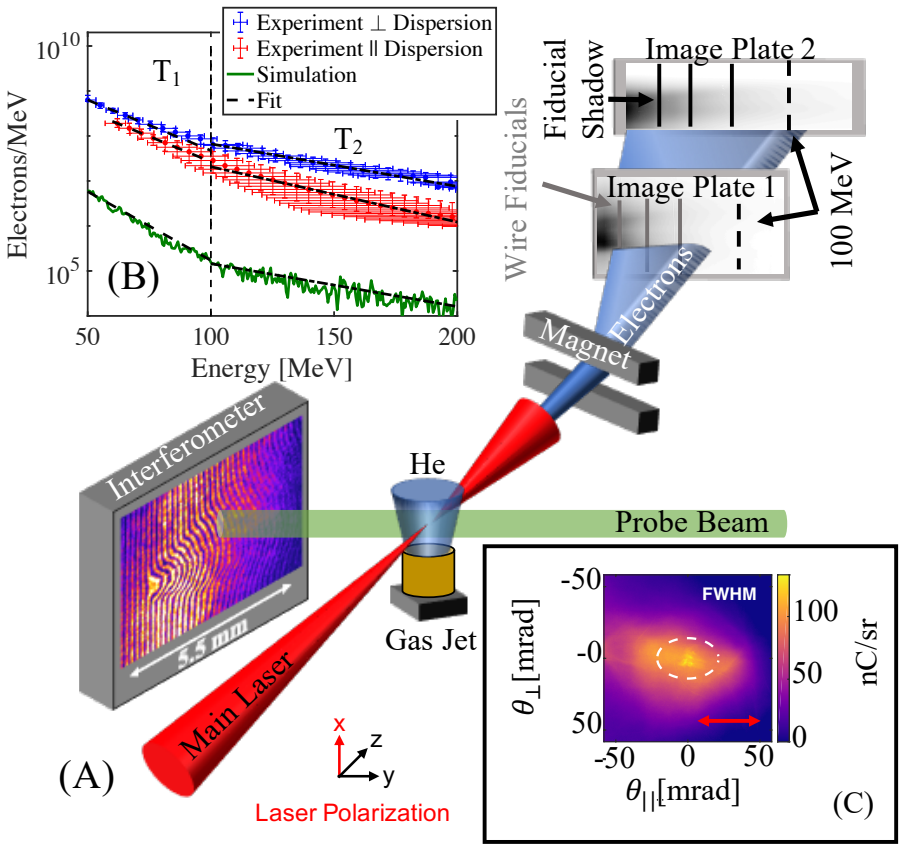

Figure 4.1: (A) Experimental setup. The electron beam is dispersed by a 0.6 T magnet onto two BAS-MS image plates after passing through three wire fiducials. A frequency-doubled probe beam is co-timed with the main pulse and provides on-shot interferometry of the plasma channel with a magnification of 3. (B) The electron energy spectrum for two different shots using identical laser and plasma parameters dispersed perpendicular and parallel to the laser polarization in blue and red, respectively, along with the simulated electron spectrum in green. All three spectra are fit to single-temperature distributions below (T_1) and above (T_2) 100 MeV; the two regions are separated by a dashed black line. The experimental spectra exhibit shot-to-shot variations of the single-shot laser system. (C) An undispersed electron beam profile.

The electron beam is dispersed by a 0.6 T magnet with a large opening aperture (5 cm) perpendicular to the linear laser polarization. A smaller magnet (2.56 cm aperture)

with a 1 T field is used to disperse the electrons parallel to the linear laser polarization. The dispersed electron signal passes through three wire fiducials—used to reduce error in the energy calculation [60]—and is captured on two BAS-MS image plates separated by 30 cm. The difference in the electron energy spectra in Fig. 4.1(B) is caused by shot-to-shot variation in the laser energy, pulse width, and quality of the high-power spot size. In an ideal case, these two spectra would be identical.

To determine the energy mapping of the dispersed electron spectra, a two-dimensional code was developed to propagate a beam of electrons with angular spread θ through a discrete magnetic field (experimentally measured using a hall probe), then map the input electron energy to a location on an image plate. This was done analytically using the following equations:

$$R = \frac{[(E + m_e c^2)^2 - (m_e c^2)^2]^{1/2}}{ecB}, \tag{4.1}$$

where R is the cyclotron radius, E is the electron kinetic energy, m_e is the electron mass, c is the speed of light, e is the electron charge, and B is the magnetic field amplitude. The exit angle, θ_{exit}, at which the electron leaves the discrete magnetic field unit was found as

$$\theta_{\text{exit}} = a\sin\left(\frac{z_m - R\sin\theta_{\text{in}}}{R}\right), \tag{4.2}$$

where θ_{in} is the angle at which the electron entered the magnetic field and z_m is the length of the magnetic field element. The horizontal shift from center, Δx, at which the electron leaves the magnetic field unit was calculated as

$$\Delta x = R\left(\cos\theta_{\text{in}} - \cos\theta_{\text{exit}}\right). \tag{4.3}$$

Summing all of the Δx contributions from each magnetic field element shows where the electron leaves the back of the magnet, given an initial input displacement and angle. From the output displacement and angle, a line can be drawn through the two detector planes and matched with the wire fiducial shadow locations on the image plates. Additionally,

each image plate in the code is able to translate laterally to account for human error during the installation of each image plate during the experiment. By allowing the image plates to laterally translate results in an energy mapping solution for each image plate location. To account for this, any solution where electrons are unable to pass through all three wire fiducials are discarded. This was calculated for electrons with energies ranging from 1 to 1000 MeV and an angular spread of 2 rad FWHM. Following the two-screen wire fiducial method, we are able to bound the angular spread of the input electron beam and reduce the error in the energy mapping. The error shown in Fig. 4.1 (B) is calculated using a combination of electron beam angular spread and uncertainty in image plate lateral location. However, due to space limitations in the target chamber, the experimental data taken using the smaller 1 T magnet did not have the space for a second image plate, resulting in the larger error seen in Fig. 1(B).

4.2.2 Experimental Discussion

The non dispersed electron beam data from our campaign is shown in Fig. 4.2 which shows an elongation of the electron beam along the laser polarization axis. This trend is evident when comparing all shots using both the 4 and 10 mm gas jet diameter nozzles and ranging in plasma density from 3.5×10^{17} to 6.5×10^{18} cm^{-3}. The elongation along the linear laser polarization is evidence of the impact of DLA during the acceleration process as electrons which oscillate along the laser polarization will bunch up at the extremes of the oscillation [35].

Additionally, we fit the electron energy spectra for several nozzle type and plasma density to a 2-temperature spectrum similar to the one shown in Fig.4.1. The results are presented in Fig. 4.3 where the measured hot and cold, T_1 and T_2 respectively, temperatures follow the similar trend where two distinct distributions can be seen above and below 100 MeV. The two temperature distribution is due to SM-LWFA acceleration mechanisms dom-

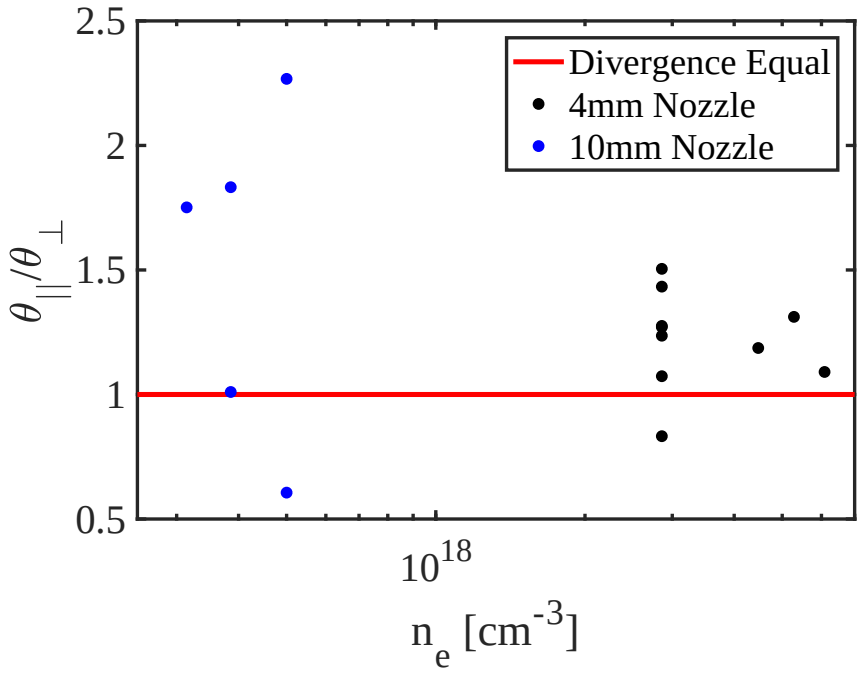

Figure 4.2: The ratio of the measured electron beam divergence parallel ($\theta_{\|}$) and perpendicular ($\theta_{\perp}$) to the linear laser polarization. Ratios greater than 1 indicate an elongation along the laser polarization.

inating the energy gain at lower final energies whereas DLA begins to dominate the energy gain at around 60 MeV.

The electron spectra shown in Fig. 4.4 dispersed (A) perpendicular and (B) parallel to the laser polarization were each fit using a single-temperature function ($Ae^{-\frac{E}{T}}$, with amplitude A and effective temperature T in MeV) below and above 100 MeV [Fig. 4.1(B)], yielding low and high temperatures of $T_1 = 19 \pm 0.65$ MeV and $T_2 = 46 \pm 2.45$ MeV, respectively. The perpendicularly dispersed electron signal in (A) (after it is converted to give a linear energy dispersion) shows a clear fork-like structure that begins at electron energies of ~60 MeV. At 75 MeV, the FWHM of the divergence angle of this fork is 43 mrad

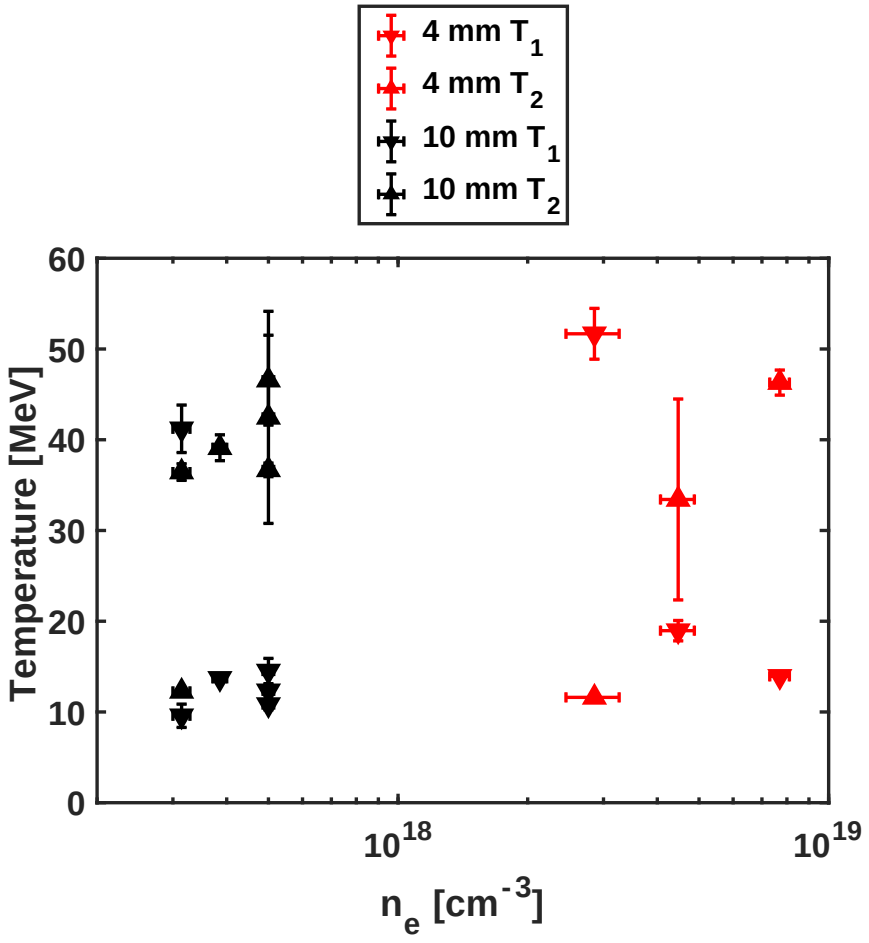

Figure 4.3: All the measured hot (cold), T_1 (T_2) temperatures for the 4 (10) mm gas jet nozzles used in the experiment following the same analysis described in the main text body.

[white curve in Fig. 4.4(A)]. The mean total charge contained in this portion of the spectrum (> 60 MeV) is 1.14 ± 0.69 nC. When the electrons are dispersed in the same plane as the laser electric field [Fig. 4.4(B)], no forking structure is seen, and the FWHM beam divergence is instead 21 mrad [red curve in Fig. 4.4(B)] at the same energy. The elliptical beam profile of the electrons shown in Fig. 4.1(C) gives the overall full-angle divergence at half-maximum

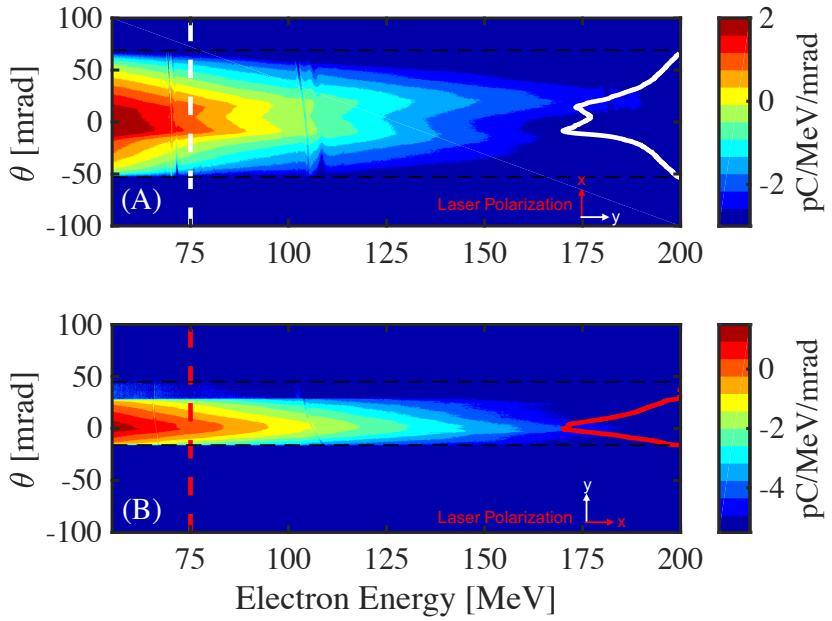

Figure 4.4: Measured electron energy spectra for a plasma with electron density $n_e = 3 \times 10^{17}$ cm^{-3} dispersed (A) perpendicular and (B) parallel to the linear laser polarization direction. The contrast is adjusted and a line-out along the dashed line is plotted (solid line) to emphasize the forking feature in the dispersed electron profile. The dashed black line indicates the acceptance aperture of the magnet. Note that (A) and (B) were taken on two different shots with similar laser energies.

charge of the electron beam in the two planes as 47 and 27 mrad in the x and y directions, respectively, consistent with the dispersed spectra.

The forking structure gives clear evidence that electrons above 60 MeV are gaining some or most of their energy by the DLA process [34, 35]. Electrons accelerated mainly through DLA generally exhibit higher energy and greater divergence along the laser polarization direction compared to electrons accelerated predominantly through SM-LWFA. This larger divergence is evident in the forking structure seen only for high-energy electrons dispersed perpendicular to the laser polarization, as in Fig. 4.4(A).

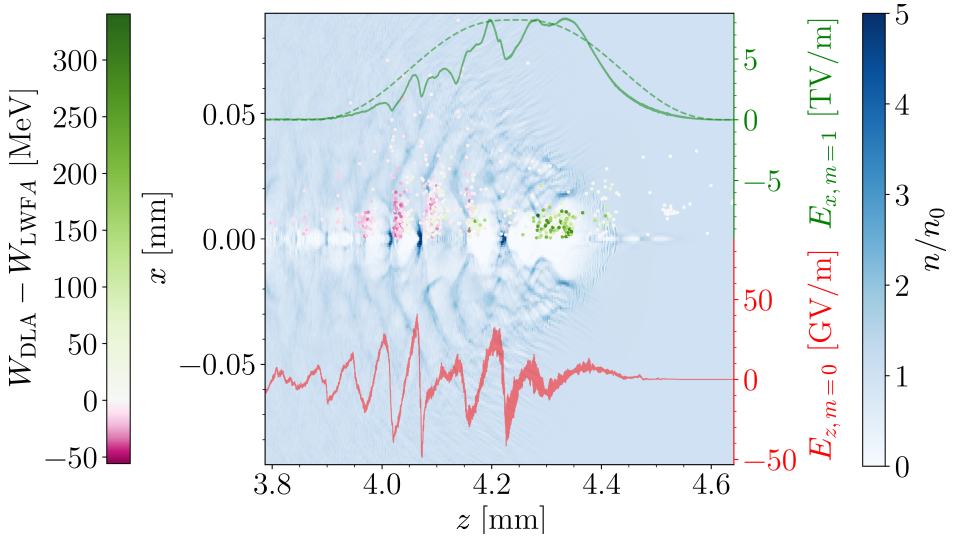

Figure 4.5: Snapshot of the electron density profile after 4.64 mm of propagation (left to right) through the plasma; z and x are the longitudinal and transverse directions, respectively. Also shown are the $m = 0$ longitudinal electric field (SM-LWFA) overlaid in red and the $m = 1$ transverse electric field envelope (DLA) in green. The dashed green line shows the vacuum laser field envelope at the focus. The tracked electrons, with x positions given by their radial distance (only half-space is shown), indicate where in space each acceleration mechanism is dominant. The charge density has been integrated in θ.

4.3 Simulation Results

4.3.1 Simulation Configuration

To discern the relative contribution of the various mechanisms to the final energy of the electrons, we simulated the full acceleration process with particle tracking using the quasi-3D algorithm of the Osiris PIC simulation framework [58, 59] for laser and plasma parameters similar to those used in the experiment. This algorithm allows us to unambiguously determine the work done by the longitudinal field of the plasma wave ($E_{z,m=0}$), as well as the transverse ($E_{x,m=1}$) and longitudinal ($E_{z,m=1}$) fields of the laser. This has allowed us to more correctly determine the overall DLA contribution. Here $m = 0$ and $m = 1$ refer to the cylindrical modes corresponding predominantly to the wake and the laser, respectively.

The quasi-3D algorithm uses fields and currents defined on an r-z grid and expanded in azimuthal modes; to simulate LWFA we used modes 0 and 1, where mode 0 (1) mainly captures the wake (laser) fields. In addition, we used a customized field solver that corrects both for dispersion errors of light in vacuum and the time-staggering error of the magnetic field in the Lorentz force [61]. The simulations were carried out in the speed-of-light frame (moving window) with a box of size $95 \times 23.6\, c/\omega_p = 854 \times 212\,\mu\text{m}$ (the second dimension corresponding only to a half-slice, r starting at 0), where $c/\omega_p = 8.991\,\mu\text{m}$ for a density of $3.5 \times 10^{17}\,\text{cm}^{-3}$. The number of grid points used was $48000 \times 256 = 1.2 \times 10^7$, with a time step of $\Delta t = 5 \times 10^{-4}\omega_p^{-1} = 30$ fs. The laser pulse had an amplitude of $a_0 = 2.7$, intensity FWHM of 1 ps, spot size of $w_0 = 25.5\,\mu\text{m}$ and Rayleigh length of $z_R = 1.94$ mm. We used a preformed plasma with a density upramp of $500\,\mu\text{m}$ followed by a constant-density region, with the laser focused halfway through the upramp. Mobile ions were included along with electrons, with each species having 4 particles per r-z cell and 8 particles in the θ direction, making for a total of 7.9×10^8 particles.

Though the experimental gas jet was 10 mm in length, we found electron energies comparable to those from the experiment after a propagation distance of only 4.68 mm in the simulation. This discrepancy is likely caused by the non-ideal laser spot used in the experiment, while the simulation used an ideal Gaussian spatial profile at the laser focus. The non-ideal laser spot could necessitate additional time to form an SM-LWFA and begin trapping electrons in the experiment, whereas this happened over a shorter distance in the simulation.

4.3.2 Simulation Discussion

Figure 4.5 shows the envelope of the transverse laser field $E_{x,m=1}$ (green), the plasma density (blue) and the on-axis longitudinal electric field of the plasma wave $E_{z,m=0}$ (red) 4.64 mm into the plasma. Clear modulation of both the laser envelope and plasma waves is

evident. However, a hydrodynamic channel is not fully formed (not shown) within the laser pulse; the ion density remains above $0.9n_0$ across the first bucket (potential well) and above $0.7n_0$ where the laser field is of significant amplitude, where n_0 is the initial plasma density. The wavelength of the plasma wave is increased for the first three buckets by strong beam loading, but for subsequent buckets it is close to $2\pi c/\omega_p$. The plasma electrons trapped by the plasma wave are color-coded to indicate which acceleration mechanism is at work (see subsequent paragraphs). The accelerated electrons group together in the later plasma buckets, where they gain energy predominantly by interacting with the longitudinal field of the wave associated with SM-LWFA. However, the electrons trapped in the front three buckets of the wake gain net energy predominantly through the DLA process as they interact with the peak-intensity portion of the laser pulse. Relativistic self-focusing helps to maintain the peak intensity of the laser pulse (see dashed green line).

To quantify the contribution of each acceleration mechanism (i.e., SM-LWFA and DLA), we use electron tracking in OSIRIS to calculate the work done on each electron by the different spatial components of mode 0 (wake) and mode 1 (laser). Separating the fields by mode clearly shows which longitudinal field component is from the plasma wave ($E_{z,m=0}$) and which is predominantly from the evolving laser field ($E_{z,m=1}$). Without separating the fields by mode, effects from the longitudinal laser electric field can be misattributed to wakefield energy gain or loss—for instance, the total work done on some electrons by the $E_{z,m=1}$ field was -100 MeV. This energy loss occurs because the longitudinal component of the laser electric field is roughly $\pi/2$ out of phase with the transverse laser electric field, $E_{x,m=1}$. In fact, the ratio f of average energy gained during betatron oscillation from the parallel ($\left\langle W_\parallel \right\rangle$) and perpendicular ($\langle W_\perp \rangle$) fields of a Gaussian laser is given [62] as

$$f \equiv \frac{\left\langle W_\parallel \right\rangle}{\langle W_\perp \rangle} = -\frac{2c^2\sqrt{2\gamma}}{\omega\omega_p w_0^2}, \tag{4.4}$$

where w_0 is the beam waist and γ is the gamma factor of a particle. The ratio is negative,

indicating that an electron in phase with the transverse laser electric field ($E_{x,m=1}$) loses energy due to the longitudinal laser electric field ($E_{z,m=1}$). Prior to this work, the LWFA and DLA processes were differentiated by longitudinal and transverse field components, respectively, rather than separated by mode. Consequently the energy loss from the longitudinal laser electric field was often attributed to SM-LWFA electric fields. Experiments and 2D PIC simulations have shown some contribution of the longitudinal laser field to the acceleration of electrons, but for a near-critical-density plasma using foam targets [63], and similar simulation work has shown evidence of energy loss due to the longitudinal laser fields [64].

The work done on each electron is then calculated as follows: $W_{\mathrm{LWFA}} = \int \vec{E}_{m=0} \cdot \vec{v}\, dt$ and $W_{\mathrm{DLA}} = \int \vec{E}_{m=1} \cdot \vec{v}\, dt$. We subtract the work done by each mechanism to obtain a relative energy contribution for each electron (see color of tracked electrons in Fig. 4.5), where a positive (negative) value indicates that the net final energy of the electron is mainly coming from DLA (LWFA). DLA is the dominant energy transfer mechanism for electrons trapped in the front two buckets (Fig. 4.5), whereas SM-LWFA dominates in the later buckets of the plasma wave. As mentioned earlier, due to the low-density plasma, a substantial ion channel—where prior results show DLA dominating the acceleration scheme [33]—does not form within the laser fields.

Figure 4.6 clearly shows that DLA dominates the energy gain for higher-energy electrons where the forking is observed. The accelerated electrons from OSIRIS are dispersed (A) perpendicular and (B) parallel to the linear laser polarization using a geometry identical to that shown for the experimental results in Fig. 4.4. In this direct comparison to the experimental data, a forking structure is evident only when the electrons are dispersed perpendicular to the laser polarization. Figure 4.6(C) shows that the longitudinal field, $E_{z,m=0}$, of the self-modulated wake (purple dots and curve) dominates energy gain for electrons with energies up to about 40 MeV, at which point the net DLA contribution (red dots and curve) becomes comparable. At around 60 MeV, the dominant acceleration mechanism

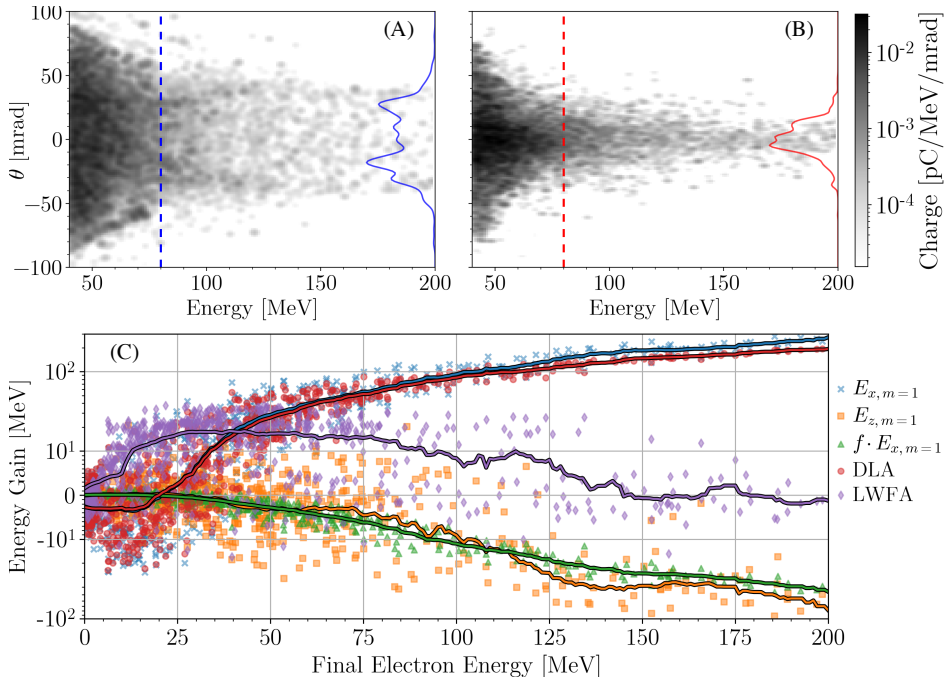

Figure 4.6: Simulated electron spectra dispersed (A) perpendicular and (B) parallel to the linear laser polarization direction. A line-out along the dashed line is plotted (solid line) to emphasize the "horns" of the dispersed beam. (C) The final energy gain due to different field components and mechanisms is shown for numerous tracked electrons (solid lines showing the mean within 20-MeV windows). All data is shown after 4.68 mm of propagation.

in the simulation shifts to DLA, with the fork becoming visible at about the same energy for the perpendicularly dispersed electrons both in the experiment [Fig. 4.4(A)] and simulation [Fig. 4.6(A)]. The energy loss from the longitudinal laser field [orange dots and curve in Fig. 4.6(C)] is reasonably approximated for many electrons by the calculation $f \cdot E_{x,m=1}$ shown in green (assumed focused spot size of $w_0 = 19\,\mu\text{m}$), which could be used to estimate the energy loss from the longitudinal laser field in simulations where it is difficult to differentiate between longitudinal wake and laser fields. Regardless, this energy loss is significant and should not be ignored when considering the energy contribution due to DLA.

The simulated electron spectrum is shown alongside the experimental spectra in

Fig. 4.1(B), with T_1 and T_2 fits of 14.2 and 45.5 MeV, respectively. Both the number of electrons and the fitted temperatures are similar to the experimental values. The temperature transition, however, occurs near 100 MeV and not 60 MeV (where the DLA mechanism becomes dominant) since the population of electrons accelerated by the DLA mechanism is much smaller than that accelerated by the LWFA mechanism.

4.4 Summary

In conclusion, we have demonstrated that a picosecond-laser pulse undergoes SM-LWFA in a low-density plasma and that DLA dominates the energy gain of the highest-energy electrons in the absence of a trailing ion channel. This contribution is shown experimentally—and reproduced with PIC simulations—by the forking structure evident in the dispersed electron beam at high electron energies, as well as through the transition between two temperatures in the measured electron spectra at around 100 MeV. This work provides the first direct experimental characterization, confirmed through quasi-3D PIC simulations with mode separation of fields, of DLA in a picosecond, high-energy regime of SM-LWFA, an important result in the development of x-ray sources for HEDS experiments.

Chapter 5

X-ray source characterization using SM-LWFA

5.1 Introduction

[1] Now that we have discussed the underlying physical mechanisms used during this dissertation work we focus on the charicterization and developement of x-ray sources using SM-LWFA as the electron driver. The prior chapter discussed the electron beam characteristics of a SM-LWFA and the underlying accelerator physics. This chapter will describe the development of analytical tools and diagnostics used to measure the resulting x-ray spectra.

A SM-LWFA offers a compact means of generating relativistic electron beams [3, 21] using existing picosecond lasers in operation at NIF (ARC), OMEGA (OMEGA-EP), LMJ (PETAL), and GEKKO (LFEX). The electrons produced in a SM-LWFA can be used to generate x-rays through several processes like betatron emission [41, 65], electron-driven bremsstrahlung radiation [66], and inverse Compton scattering [67, 68].

Betatron x-rays are generated during the acceleration process in a SM-LWFA. Electrons trapped off axis and accelerated longitudinally also oscillate in the transverse direction due to space charge separation and produce x-rays in the laser propagation direction. Betatron x-rays from SM-LWFA and direct laser acceleration have been shown to reach photon

[1] This chapter contains published information from: P. M. King, N. Lemos, J. L. Shaw, A. L. Milder, K. A. Marsh, A. Pak, B. M. Hegelich, P. Michel, J. Moody, C. Joshi, and F. Albert. X-ray analysis methods for sources from self-modulated laser wakefield acceleration driven by picosecond lasers. Review of Scientific Instruments, 90(3):033503, 2019. of which I am the first author. My contribution to this work included experimental planning and execution, data analysis, and writing the published manuscript.

fluxes $> 10^{10}$ photons/keV/sr with x-ray energies > 15 keV and a source size < 35 μm [19, 69].

Inverse Compton scattering is produced when an electron collides with a photon up-shifted by 2γ in the electron frame, where γ is the Lorentz factor of the electron. The electron oscillating in this Doppler shifted radiation field re-emits a photon, which in the laboratory frame is in the forward direction and is frequency up-shifted by an additional 2γ for a total of $4\gamma^2$, in the case of head on collision. A common method of producing Compton x-rays in a laser wakefield experiment is to place a plasma mirror at the exit of the gas jet and reflect the drive laser pulse back onto the electrons [67]. In the SM-LWFA regime, this method can produce x-rays of energies > 100 keV with small source sizes <100 μm and high photon flux $> 10^8$ photons/keV/sr [20].

Bremsstrahlung radiation is achieved by colliding the electron beam produced in a SM-LWFA with a high Z foil target. The electrons collide with the nuclei of the high Z foil producing high energy x-rays with a large divergence. Bremsstrahlung radiation produced through electron interactions has shown an increased x-ray generation efficiency over the previously discussed laser-generated bremsstrahlung sources and is capable of reaching temperatures of > 1 MeV with a photon flux $> 10^9$ photons/keV/sr [66, 70].

The optimization of x-ray emission properties, which vary based upon generation mechanism, motivates the development of robust analysis methods to be used for any SM-LWFA x-ray source in a spectral range between 10 keV and 1 MeV. This paper describes three of them: forward fit, Ross pair, and differential average transmission (DAT), for three different diagnositics, each sensitive to a different range of x-ray energies (thin filters, stacked image plate spectrometer [71], and step wedge [72]). This paper is organized as follows: Section II presents an overview of the experiments; Section III details and compares each of the analysis methods and diagnostics using a laser-driven bremsstrahlung source; Section IV applies these methods and diagnostics to quantify x-ray sources driven by SM-LWFA on

a > 100 J, ps laser system, the Titan Laser at LLNL.

5.2 Experimental Overview

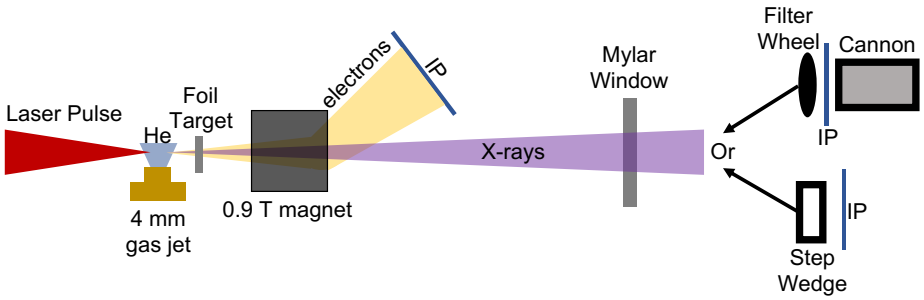

Figure 5.1: Experimental set up for SM-LWFA experiment on the Titan Laser at JLF.

The Titan laser, located at the Jupiter Laser Facility (JLF) at Lawrence Livermore National Laboratory (LLNL), has a beam energy of 120 J, pulse length of $0.7^{+0.3}_{-0.1}$ ps, and central wavelength of 1053 nm. In our experiment, shown in figure 5.1, the laser is focused 1 mm above a 4 mm He gas jet using a $F/10$ off axis parabolic mirror to obtain a spot size of $\sim$ 29 μm and an intensity of $\sim 10^{19}$ W/cm^2. The laser pulse ionizes the He gas and creates a plasma with a density of $\sim 5 \times 10^{18}$ cm^{-3} and drives a SM-LWFA, which produces a beam of electrons with a maximum energy of $\sim$ 380 MeV. Betatron x-rays are generated during the acceleration of electrons in the SM-LWFA, and by placing a 100 μm polyethylene target at the exit of the jet or a 500 μm W target 15 mm from the exit of the gas jet, inverse Compton scattered or bremsstrahlung x-rays are generated, respectively. The electrons produced in the SM-LWFA are bent away from the propagation axis using a 0.9 T magnetic spectrometer. The electron signal is captured on a Fujifilm BAS-IP MS image plate (IP), the type of IP used for all the diagnostics, and an energy spectrum is determined by mapping the displacement in horizontal direction on the IP to the expected location given the spectrometer calibration.

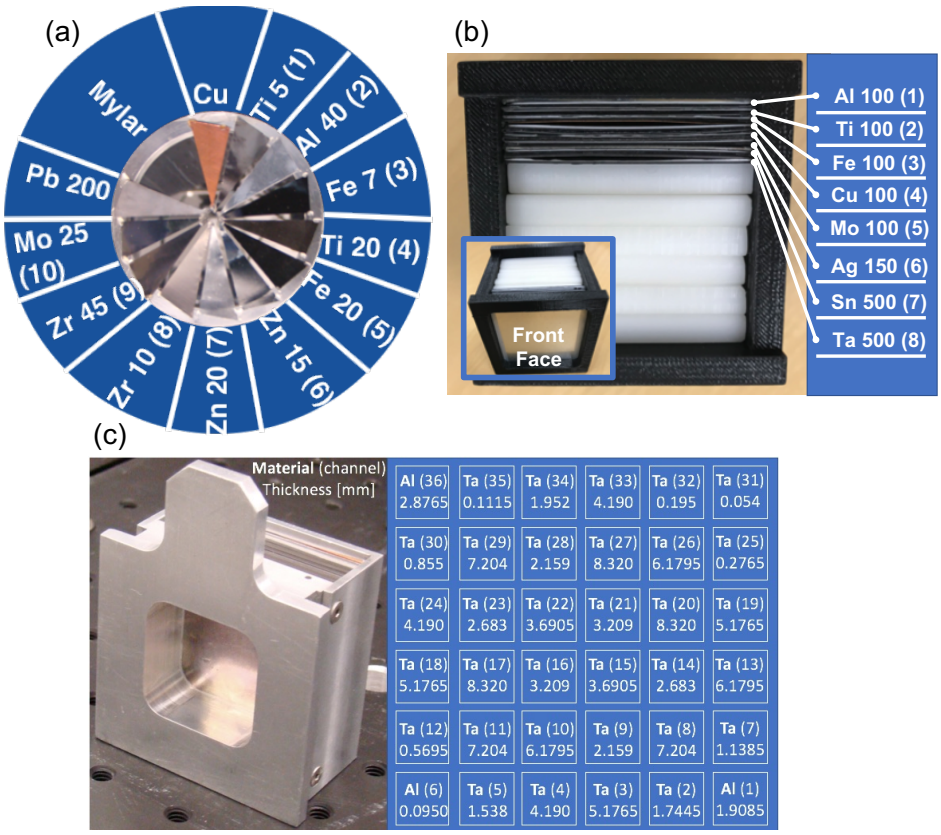

Figure 5.2: (a) The filter wheel diagnostic channels are labeled clockwise from the top right, each corresponding to a different material and thickness. The image is labeled with the material type, thickness in μm, and the channel number, respectively. (b) The cannon diagnostic channels are labeled from the front of the detector to the back, each corresponding to a different material and thickness, labeled with the material type, thickness in μm, and channel number, respectively. The inset shows a view of the cannon from the front. (c) The step wedge diagnostic uses varying thicknesses of Ta to attenuate the x-ray signal.

The x-rays exit the target chamber via a 200 μm mylar window located 1.5 m from the gas jet and enter the filter wheel, figure 5.2a, located 4 cm from the mylar window. The filter wheel is a set of 10 materials, differing in thicknesses, that are sensitive to x-ray energies up to $\sim$ 40 keV. The transmission of all the channels, shown in figure 5.3, reaches 100% at roughly 40 keV, preventing x-rays above this energy to be differentiated. The materials,

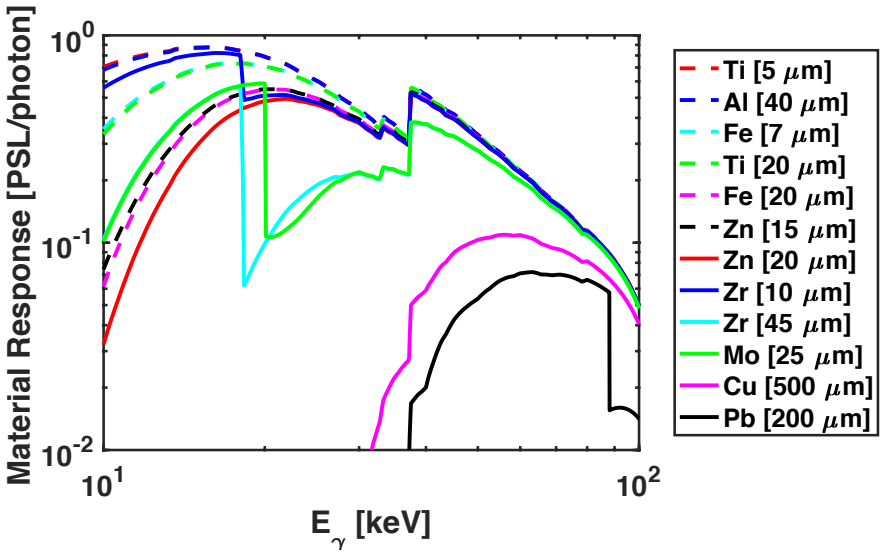

Figure 5.3: Filter wheel material response curves as a function of x-ray energy converted to PSL/photon.

thicknesses, and channel number are detailed in figure 5.2a. The transmitted x-ray signal is collected by an IP placed at the back of the filter wheel. The x-rays pass through the filter wheel and into the cannon, shown in figure 5.2b, which uses 8 filters stacked behind one another with an IP between each material to capture the x-ray signal in each layer [71, 73]. The cannon is sensitive to a higher energy range, 30 to $\sim$ 200 keV, and is used in tandem with the filter wheel to improve the energy detection range. For higher expected x-ray energies (up to a few MeV), the step wedge diagnostic replaces both the filter wheel and cannon along the beam axis. The step wedge uses stacked plates of Ta with holes cut into them creating channels of varying thickness to alter the x-ray attenuation through each. The signal is then collected on an IP placed behind the diagnostic [72].

The IPs are all scanned using a Fuji model FLA7000 scanner at a 200 μm pixel size. The scanner provides a measure of counts per pixel that is then converted to photo stimulated luminescence (PSL) using the calibration equation provided by ref. [74].

5.3 Analysis Methods

This section presents the diagnostics results and associated analysis methods in the case of a laser-driven bremsstrahlung source. Laser-driven bremsstrahlung is used here because it is a well understood x-ray production mechanism that can be generated without creating additional x-ray noise. To ensure only laser bremsstrahlung is generated, the gas jet is not operated for these shots ensuring there is no LWFA generation. The laser focus is positioned 1 mm into the entrance of the 4 mm gas jet and a 100 μm Al target was placed at the exit of the jet, 3 mm from laser focus, so that the focal spot size is $\sim$ 50 μm and the laser intensity is 2×10^{18} W/cm^2.

5.3.1 Forward Fit Method

The forward fit method uses the x-ray attenuation properties of thin filters to fit a measured set of data and extrapolate the energy spectrum using an assumed analytical distribution function [75, 19, 20]. Equation 5.1 describes how to calculate a synthetic PSL value for each material using an assumed analytical distribution function, $f_{E,A}(E_\gamma)$, and a material response function, $Y_i(E_\gamma)$, shown in figure 5.3.

$$Y_i(E_\gamma) = T_i \times IP_{resp}$$

$$PSL_i = \int Y_i f_{E,A} dE_\gamma \times \theta, \tag{5.1}$$

where T_i is the calculated transmission of material i, IP_{resp} is the response function of the image plate [76], E_γ is the photon energy, and θ is the angle subtended by each pixel from the source. The material response is a product of each material the x-rays interact with on the way to the detector and the energy-dependent response of the detector used. Here, $f_{E,A}$ is the chosen analytical distribution function to describe the x-ray generation mechanism

where E is the energy and A the amplitude. Calculated PSL values are fit to a measured data set by varying the amplitude and energy using weighted least squares fitting tools.

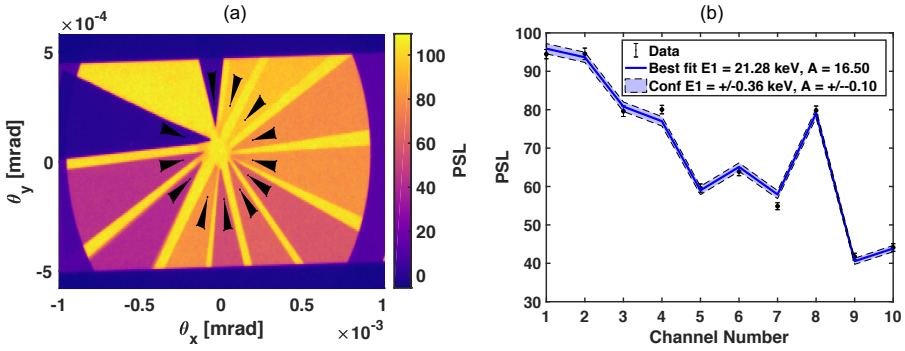

Figure 5.4: (a) Raw data of the filter wheel diagnostic on bremsstrahlung x-ray data. The black triangles show the areas in which the data was sampled to obtain mean PSL values for the fit. (b) Results of the forward fit method on bremsstrahlung x-ray data described in the text.

Bremsstrahlung emission is modeled with a single temperature distribution function, $f_{E,A} = A \times 10^{10} \times e^{-E_\gamma/E}$, that is used with equation 1 to calculate a PSL value for each channel. An example, a laser-driven bremsstrahlung source measured with the thin filter wheel, is shown in figure 5.4. The best fit for this laser bremsstrahlung data results in a temperature of 21.2 ± 0.36 keV with an amplitude of 16.5 ± 0.10, giving a total flux of 16.5 ± 0.10 $\times 10^{10}$ photons/keV/sr, plotted in blue in figure 5.4b. The mean PSL signal for each material is taken from within the area of each small triangle shown in figure 5.4a and plotted as black data points in figure 5.4b. The error in PSL is the standard deviation of the signal in each channel. The error in temperature, E1, and amplitude, A, are obtained from the best fit of the upper and lower error in PSL.

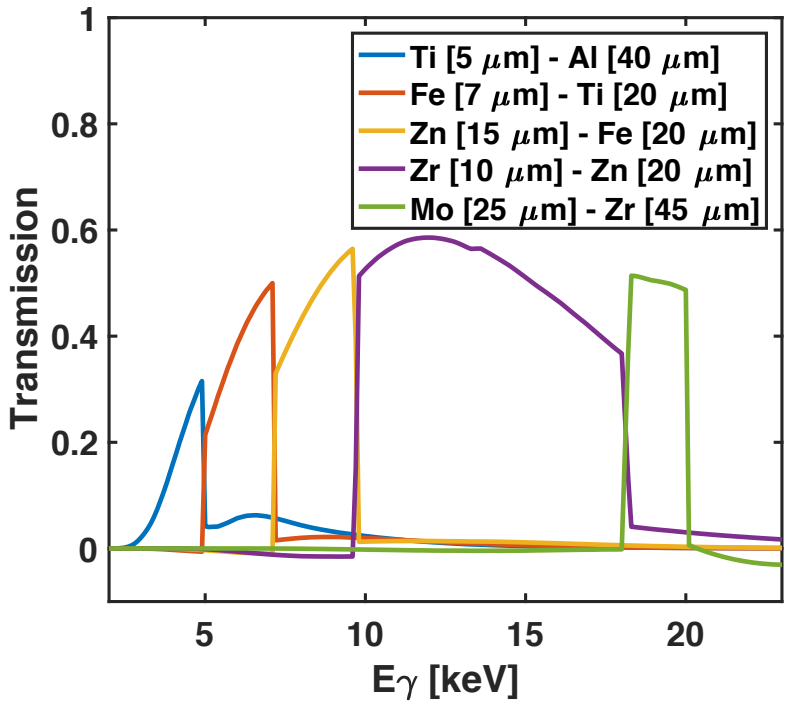

Figure 5.5: Subtraction of channels 1-2, 3-4, 6-5, 8-7, and 10-9 corresponding to 5 μm Ti - 40 μm Al, 7 μm Fe - 20 μm Ti, 15 μm Zn - 20 μm Fe, 10 μm Zr - 20 μm Zn, and 25 μm Mo - 45 μm Zr results in the remaining signal appearing in small energy bins.

5.3.2 Ross Pair Method

The materials that make up the filter wheel were designed to take advantage of the Ross Pair analysis method [77]. Each material was chosen such that the K-edge location and thickness would provide a difference in signal equal to zero everywhere except for a small energy bin determined by the difference in K-edge location. The thickness of each material controls the total attenuation of the x-ray signal and can be used to ensure the signal outside each bin is as close to zero as possible. By choosing materials correctly, the Ross Pair method can provide a direct measurement of x-ray flux in a small energy range. Figure 5.5 shows the energy bins for the materials in the filter wheel diagnostic used in our experiment and the

attenuation of the signal in each bin. By subtracting channels 1-2, 3-4, 6-5, 8-7, and 10-9 corresponding to 5 μm Ti - 40 μm Al, 7 μm Fe - 20 μm Ti, 15 μm Zn - 20 μm Fe, 10 μm Zr - 20 μm Zn, and 25 μm Mo - 45 μm Zr, the flux in 5 energy bins spanning 3 to 20 keV can be directly measured.

As can be seen on the blue curve in figure 5.5, the signal outside the bin is not always exactly zero, which accounts for error in the photon number measurement. The ratio of integrated signal outside/inside is calculated as the error in photon count.

The difference in PSL values from the filter wheel data in figure 5.4a, following the same subtraction scheme that created figure 5.5, is converted to photon flux by following equation 5.2.

$$\left[\frac{d^2N}{dEd\Omega}\right]_i = \frac{PSL_i}{Tr_i^{mean} \times IP_i^{mean} \times \theta \times W_i^{bin}} \tag{5.2}$$

Here Tr_i^{mean} is the mean transmission value of each bin, IP_i^{mean} is the mean image plate response value for each bin, θ is the angle subtended by each pixel from the source, and W_i^{bin} is the bin width in keV.

5.3.3 Differential Averaged Transmission Method (DAT)

The DAT method [67] is similar to the Ross Pair method in that it utilizes the subtraction of the transmission signal from two different materials to provide a measured data point and does not rely on a particular spectral distribution. This method works well when materials in the diagnostic are the same element with varying thicknesses but may provide poor results when subtracting different elements due to the different K-edge locations. The subtracted material transmission curves of the desired materials should create a broad distribution for this method to work properly.

Figure 5.6 shows this method applied to the filter wheel diagnostic. The energy

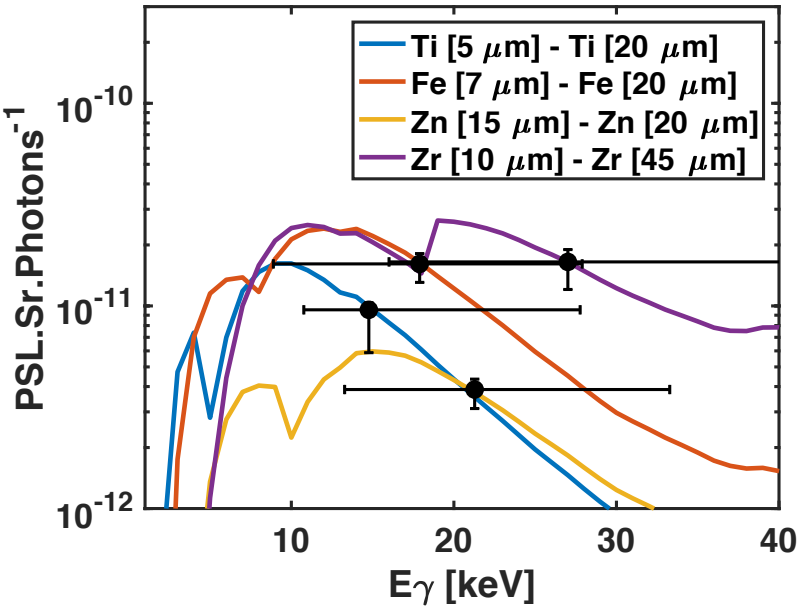

Figure 5.6: DAT bins are created by subtracting channels 1-4, 3-5, 6-7, and 9-10 corresponding to 5 μm Ti - 20 μm Ti, 7 μm Fe - 20 μm Fe, 15 μm Zn - 20 μm Zn, and 10 μm Zr - 45 μm Zr resulting in broad transmission distributions. The mean energy and full width half maximum is determined for each distribution and are used for error calculation. See text for details.

assigned to each pair corresponds to the mean energy of that pair's distribution. The bin size, corresponding to the region which contains 50% of the pair's signal, is plotted as the error in energy. The error in photon flux is determined by integrating the signal outside of the energy bin and converting the results to percentages of the total signal. The percentages are used to represent the error in measured photon flux caused by excluding the regions outside of the 50% energy bin in the calculation.

The photon number is then calculated as follows:

$$\left[\frac{d^2N}{dEd\Omega}\right]_k = \frac{(S_1 - S_2)}{\int f_k dE_\gamma} \tag{5.3}$$

$$f_k = (T_1 - T_2) \times R \times \theta$$

Here, N is the number of photons, dE is per photon energy, dΩ is per solid angle, $S_{1,2}$ are the measured signals being subtracted, $T_{1,2}$ are the calculated transmission curves through the same materials, R is the response of the detector being used, and θ is the angle subtended by each pixel in the detector.

By using the PSL values shown in figure 5.4 and the filter wheel material pairs described in figure 5.6, the photon flux is calculated and plotted in figure 5.7 along with the results of the Ross Pair method. As shown in figure 5.5 there are five possible data points which can be calculated using the Ross pair method, however figure 5.7 only has two data points plotted. The missing data points are from the first three low energy pairs which, when created through subtracting the signal from the pair's corresponding materials, resulted in a zero or negative flux. This can be caused either by x-rays with energies above the pair's sensitivity region, or by low energy x-rays which are blocked on the way to the detector. In this experiment, we were unable to resolve the Ross Pair signals below 10 keV due to the mylar window on the target chamber attenuating the signal of low energy x-rays to a level below our detection threshold.

5.3.4 Fitting the Discrete Data Points

The discrete data points, determined by the Ross Pair and DAT methods, are fit using weighted least squares fitting tools and the same distribution function as the forward fit method, $f_{E1,A} = A \times 10^{10} \times e^{-E_\gamma/E1}$ for a laser-driven bremsstrahlung source. This fit

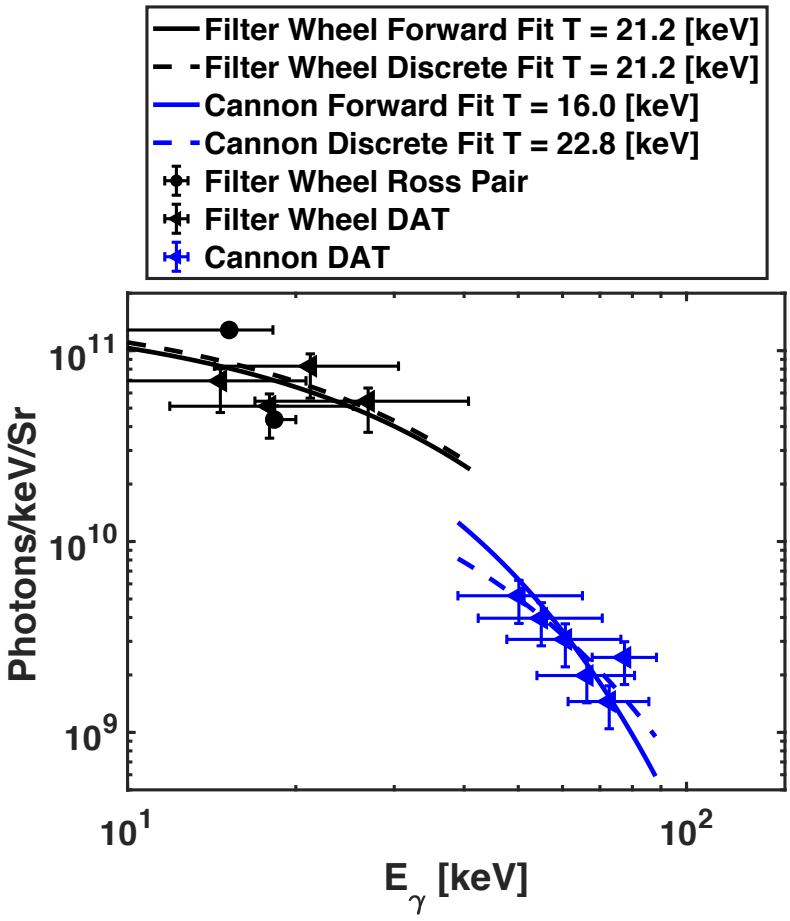

Figure 5.7: Results of forward fitting (solid) and discrete fitting (dashed) analysis for a laser-driven bremsstrahlung source using the filter wheel (black), and cannon (blue) diagnostics. Data points are the result of Ross pair (circles) and DAT (triangles) analysis methods described in the text.

provides an additional independent method of determining the temperature and amplitude of the x-ray energy spectrum. The best fit results in a temperature and amplitude of E1 = 21.2 ± 4.23 (22.9 ± 0.67) keV A = 15.9 ± 0.62 (4.5 ± 1.15) photons/keV/sr for the filter wheel (cannon) diagnostic, shown in black in figure 5.7. The error in the temperature, E1, and amplitude, A, of this fit is determined through the best fit of the upper and lower photon

flux errors of the discrete data set. The energy bins, represented by energy error bars, are not explicitly included in the fitting as the flux error accounts for signal not included within this bin. If the energy bin gets bigger or smaller, the flux error will change by an equal percentage to compensate, as detailed in section C. Like the discrete data points, their fits agree very well with the forward fit results inside each detectors sensitivity range.

5.3.5 Stacked Image Plate Spectrometer Analysis

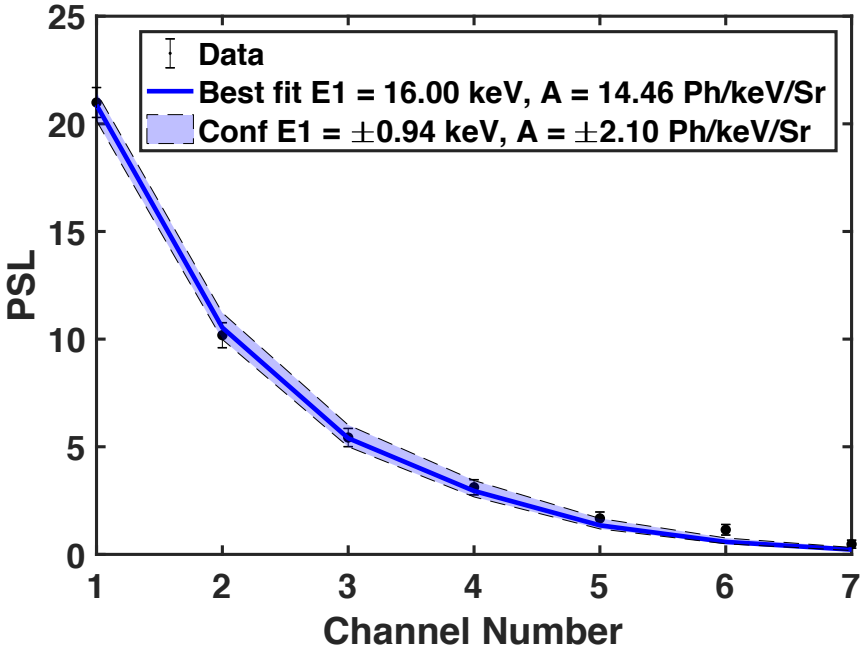

Figure 5.8: Results of the forward fitting method using the cannon diagnostic. Here E1 is the temperature and A is the amplitude of the single temperature distribution.

Sub sections A-D have detailed three analysis methods applied to a bremsstrahlung source using the filter wheel diagnostic. This section will apply the same analysis methods to the cannon, a stacked image plate spectrometer, and highlight the differences between the two diagnostics. As shown in figure 5.1, the cannon can be fielded at the same time as

the filter wheel allowing for a greater range of the x-ray spectrum to be measured. Similar to the prior sections, figure 5.8 shows the results of the forward fitting method, where the channels are detailed in figure 5.2b. The bremsstrahlung energy spectrum was again modeled using a single temperature distribution, $f(E1, A) = A \times 10^{10} \times e^{-E_\gamma/E1}$, and resulted in a temperature E1 = 16.0 ± 2.17 keV and amplitude A = 13.44 ± 3.9 Photons/keV/Sr as shown in figure 5.7. The DAT method is computed the same way as in subsection C, however, since the cannon has stacked materials S_i and T_i as defined in equation 3 represent channels rather than materials. For example, channel 1 is Al and channel 2 is 100 μm Al× Image plate transmission × 100 μm Ti. The resulting measured x-ray energies are shown in blue in figure 5.7 with the forward fit results.

5.3.6 Combining Methods and Diagnostics

The prior sections have detailed three separate methods of analyzing measured x-ray energy spectra and shown the methods applied to two diagnostics. Applying the three methods to measured x-ray data results in two valid temperature and amplitude solutions. Optimally, the two solutions will exactly agree with one another. However, due to noise in the raw data, the solutions more often will be different. Therefore, the results are combined to produce a solution band which encompasses the results from both fitting methods, forward fit and discrete fit. The results of both fits are plotted with their maximum and minimum errors, and the highest and lowest solution, regardless of fitting method, is chosen. The two temperature and amplitude solutions are then presented as the final measured x-ray energy spectrum.

As an example, figure 5.9 shows the solution band for the filter wheel (black) and the cannon (blue) on the same laser-driven bremsstrahlung shot. The solution band for the filter wheel is created by combining the lowest (T = 15.0 keV and A = 16.01 photons/keV/sr) and the highest (T = 26 keV and A = 15.28 photons/keV/sr) temperature and amplitude fit from

the forward fit and discrete fit methods. In this instance, the discrete fit fully encompasses the forward fit solution and error, so both the highest and lowest temperature and amplitude solutions are from the discrete fit.

The same method of choosing the highest and lowest fit is then applied to the cannon diagnostic resulting in temperatures, T, of 16 and 23 keV and amplitudes, A, of 16.6 and 3.8 photons/keV/sr from the forward fit and discrete fit, respectively. The cannon solution band is then combined with the filter wheel solution band to create a measured x-ray spectrum spanning 10 to 100 keV.

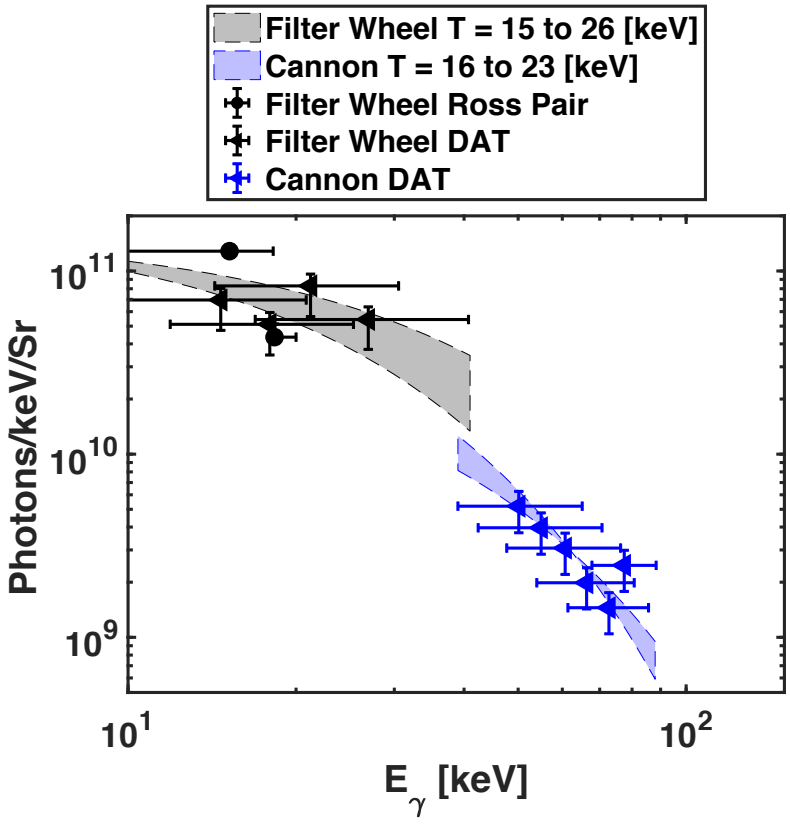

Figure 5.9: The solution bands for a laser bremsstrahlung source. The bands are created by combining forward fitting and discrete fitting as explained in the text.

5.4 SM-LWFA X-ray Sources

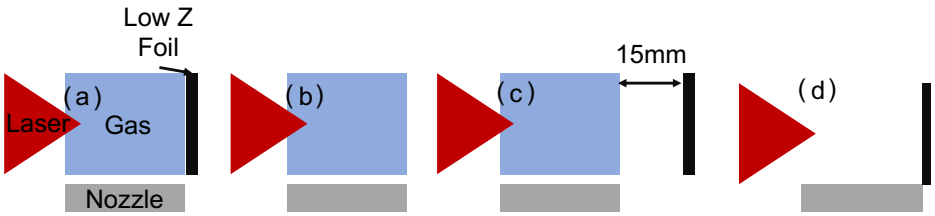

Figure 5.10: Experimental set up for each SM-LWFA x-ray generation mechanism: a) Inverse Compton b) Betatron c) electron-driven bremsstrahlung and d) laser-driven bremsstrahlung. Each method is isolated by controlling the gas and foil placement as detailed in the text.

This section presents the analysis of x-ray sources generated through SM-LWFA following the experimental schemes shown in figure 5.10. X-ray characterization from SM-LWFA generated sources generally have far more noise to mitigate than the laser-only bremsstrahlung data presented above due to the large amount of charge being diverted into the target chamber walls, and proper accounting for this noise is instrumental in correctly determining the energy spectrum of LWFA-driven x-ray sources. The filter wheel diagnostic includes a 500 μm Cu and 200 μm Pb filter to be used for background subtraction. These filters prevent any transmitted signal from x-rays above $\sim$ 40 keV from contributing to the overall data. Since the sensitivity of the filter wheel has a maximum of $\sim$ 40 keV, any signal behind these filters can be assumed as background. For data with a uniform background level, the signal level from behind the Cu and Pb filters is subtracted from the whole image to reduce the noise level and improve accuracy of the analysis. For non-uniform backgrounds, a mask is created by selecting the perimeter of each filter and removing it from the image as shown in figure 5.11. The background is smoothed over the whole image and normalized such that the maximum value of the smoothed image is equal to the signal behind the Cu or Pb filter. The smoothed image is subtracted from the main image to remove non-uniform backgrounds, vastly improving the accuracy of the analysis methods detailed above.

5.4.1 Betatron Radiation

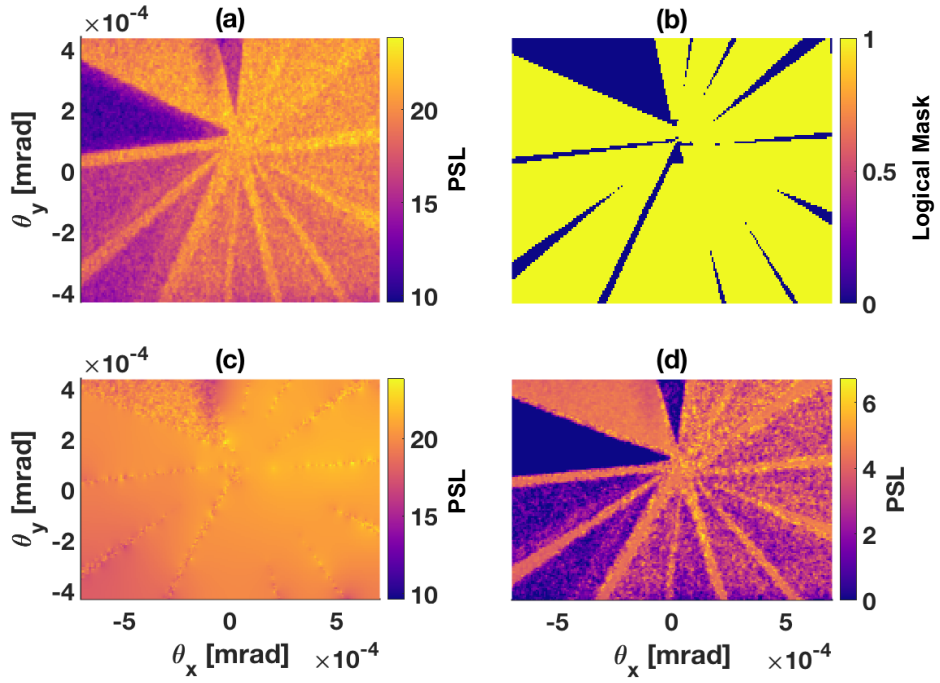

Figure 5.11: (a) Experimental data with no background subtraction (b) 2D mask created to remove filters from the background signal (c) Using the 2D mask, the background signal is smoothed over the filter regions and normalized to the PSL signal behind the copper or lead filter (d) The final image after subtracting the smoothed background from the original image

Here, betatron radiation is generated during the SM-LWFA electron acceleration process. The laser is focused as described in section II with no foil placed after the gas jet (figure 5.10b). The data analysis begins by first following the background subtraction technique detailed in figure 5.11 and then applying the three analysis methods described in section III. Figure 5.12 shows the results of these methods using $f_{E1,A} = A{\times}10^{10}\frac{E_\gamma}{E1^2}K^2_{\frac{2}{3}}[\frac{E\gamma}{E1}]$ [41, 78] as the analytic equation describing the x-ray energy spectrum. The expected energy range for betatron radiation is < 40 keV due to the critical energy scaling ($\sim 5\times10^{-21}\gamma^2 n_e[\mathrm{cm}^-3]r_0[\mu\mathrm{m}]$) where the maximum electron energy is measured to be ~300 MeV, so the filter wheel and

cannon diagnostics were used. The noise in this signal is higher than the laser bremsstrahlung example due to the large non-uniform background produced from stray electrons in the target chamber. The combined analysis methods result in a critical energy (the point in which half the energy in the spectrum lies below this value), E1, between 25 and 34 keV and an amplitude, A, between 15.7 and 16.5 photons/keV/sr. This result is combined with the Ross pair (circles) and DAT (triangles) methods in figure 5.12. Due to noise in the later channels of the cannon diagnostic which could not be mitigated, the cannon did not provide fitted critical energies to combine with the filter wheel results.

5.4.2 Inverse Compton Scattering

We generate inverse Compton radiation by placing a 100 μm polyethylene target at the exit of the gas jet as shown in figure 5.10a. The laser, after generating the SM-LWFA and accelerating electrons, exits the gas jet and ionizes the polyethylene target, creating a plasma mirror [67]. The laser pulse is reflected back onto the relativistic electrons, producing x-rays in the electron propagation direction. Here, we have contribution from four different mechanisms: betatron from the SM-LWFA, bremsstrahlung from interaction of the laser and the electrons with the foil, and the Compton radiation we seek to measure. To account for the x-rays generated from the first three mechanisms, we measure the radiation energy spectrum produced by isolated betatron, f_{Beta}, and bremsstrahlung, f_{Brem}, emissions under the same experimental conditions and include the results in the Compton analysis. The laser-driven and electron-driven bremsstrahlung components are differentiated by placing the foil at the exit and 15 mm from the exit of the gas jet, respectively, as shown in figure 5.10. In the latter case, the laser has diverged more than the electron beam ensuring the electron-driven bremsstrahlung is dominant.

Compton scattering is likely to produce higher energy x-rays than betatron radiation, as inverse Compton scattering scales as $\sim 4\gamma^2 E_l$, where E_l is the laser photon energy, and

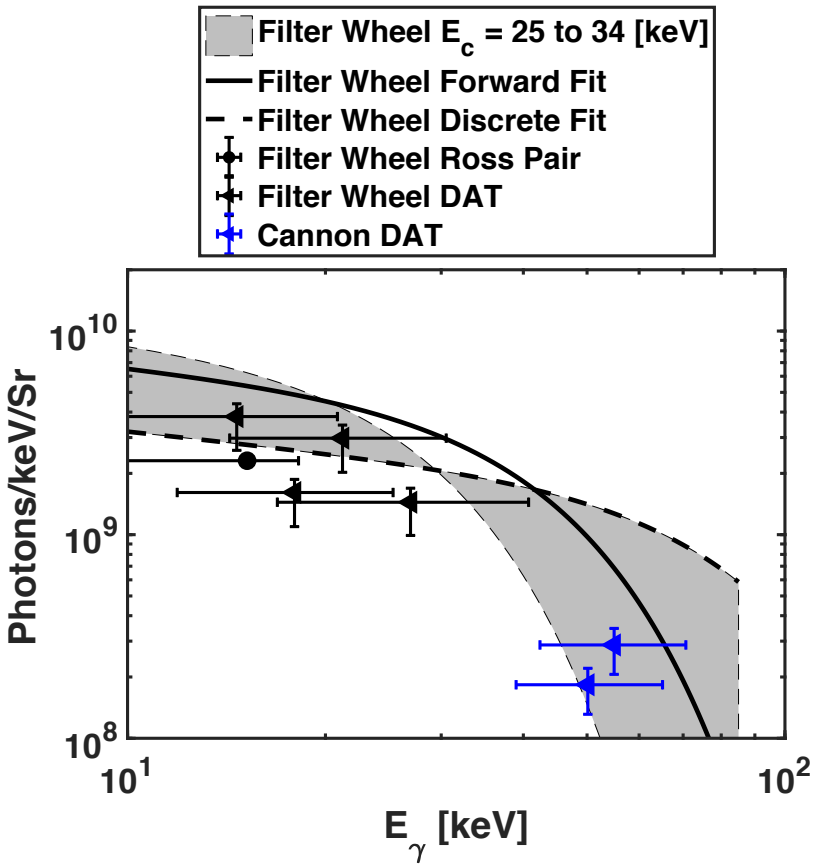

Figure 5.12: Combining the forward fit, Ross pair, and DAT analysis methods from the filter wheel and cannon diagnostics, create a band of solutions between critical energies of 25 and 34 keV using the filter wheel diagnostic. Only the first three channels of the cannon had signal above the detection threshold, resulting in two data points using the DAT method. These data points are not sufficient to use the fitting method but are plotted here to show agreement with the filter wheel solution band, which is extrapolated to 65 keV.

betatron radiation drops exponentially after its critical energy $5 \times 10^{-21}\gamma^2 n_e[\mathrm{cm}^{-3}]r_0[\mu\mathrm{m}]$. Hence, we use the step wedge [65]. A single temperature spectrum, $f_{E1,A} = f_{Beta}+f_{Brem}+A\times 10^{10}e^{\left(-\frac{E\gamma}{E1}\right)}$, is used for the forward fit and discrete fit methods after first using the background subtraction technique detailed in figure 5.11. The Compton emission is approximated as a

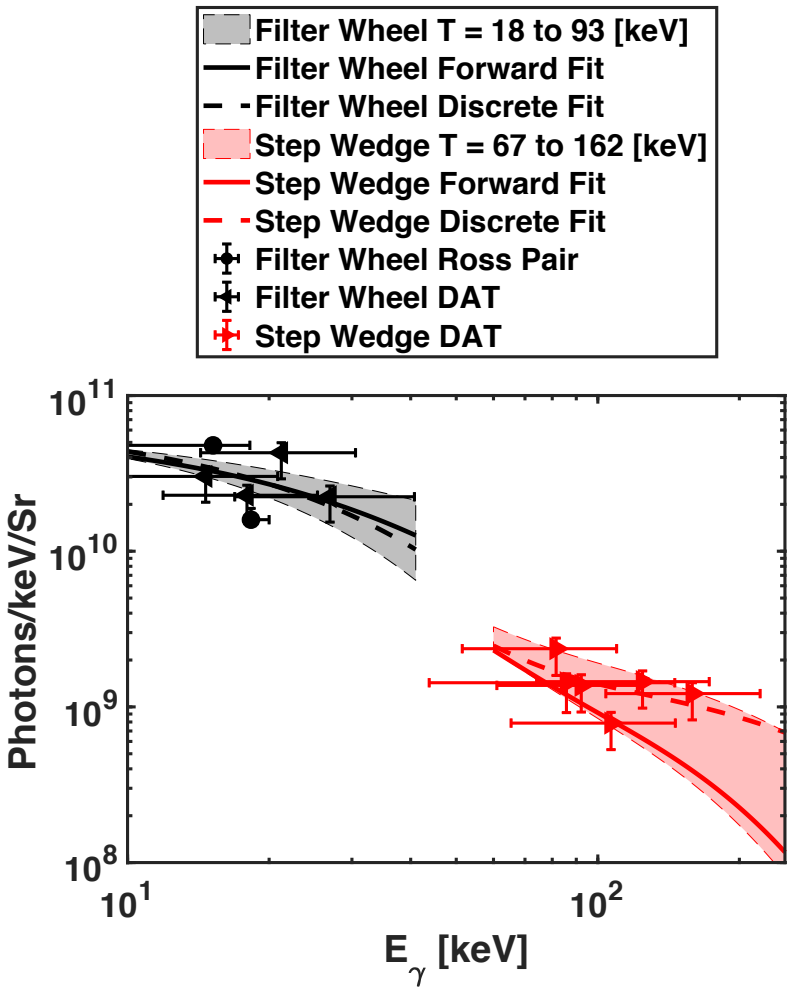

Figure 5.13: The filter wheel (black) and step wedge (red) were used to measure the low and high energy regions of the Inverse Compton x-ray spectrum respectively. The filter wheel measured a temperature band of 18 to 93 keV in the 10 to 40 keV region while the step wedge measured a temperature band of 67 to 162 keV between 60 to 250 keV.

single temperature distribution in the narrow range of sensitivity for both the filter wheel and step wedge. The resulting temperature bands, found by following the analysis methods described in section III, are shown in figure 5.13 to be E1 = 18 to 93 keV and E1 = 67 to 162 keV between 10 to 40 keV and 60 to 250 keV respectively. These sensitivity regions are

dictated by the diagnostics and not the spectrum being measured. The lower energy region measured by the filter wheel has large components of laser bremsstrahlung and betatron signal, however, the signal in the higher energy region measured by the step wedge can only be x-rays produced through Inverse Compton [20].

5.4.3 Electron Bremsstrahlung Radiation

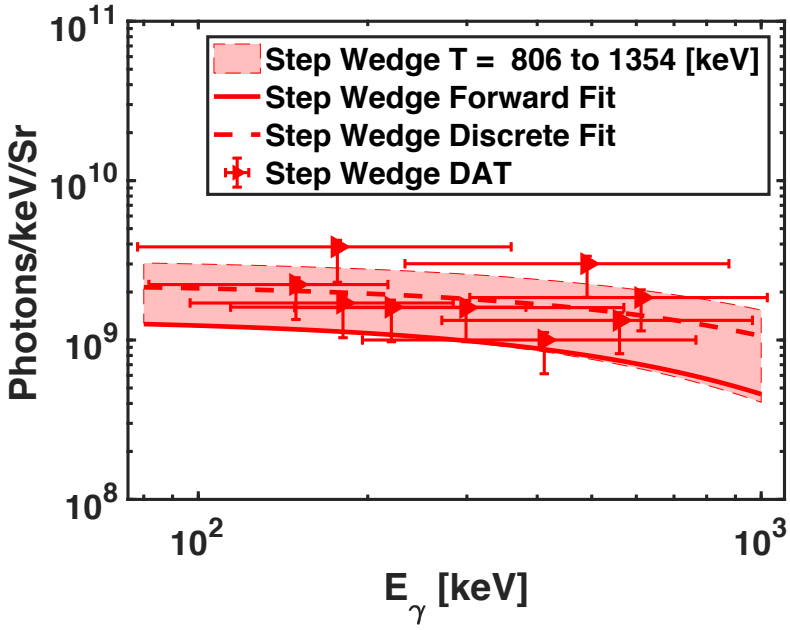

Figure 5.14: The forward fit and discrete fit for electron-driven bremsstrahlung x-rays produce a solution band with temperatures between 806 and 1354 keV (red shaded region).

Electron-driven bremsstrahlung radiation is generated by colliding the relativistic electrons from a SM-LWFA with a 500 μm thick W target placed 15 mm from the exit of the gas jet, mitigating laser bremsstrahlung and inverse Compton emissions, as shown in figure 5.10c. A 500 μm target is chosen for this mechanism to convert as much of the electron energy into x-rays as possible, without being too thick so that x-rays are re-absorbed.

By choosing the correct high-Z foil, much of the electron energy can be converted to x-rays through collisions in the foil, producing a high temperature (MeV) emission spectrum. Due to the expected high energy x-ray production, the step wedge diagnostic is used to analyze the electron-driven bremsstrahlung emission spectrum. The temperature bands for this mechanism are found to be T = 806 to 1354 keV by fitting to a single temperature distribution, $f_{E1,A} = A \times 10^{10} e^{\left(-\frac{E\gamma}{T}\right)}$, following the analysis methods detailed in section III. The result of this analysis is plotted with data points following the DAT method in figure 5.14.

5.5 Summary

In conclusion, we have shown the analysis methods employed to fully characterize x-ray energy spectra generated through SM-LWFA. These methods were applied to three diagnostics, each sensitive to a different energy range: the filter wheel (10 to 40 keV), cannon (30 to 80 keV), and step wedge (60 keV to >1 MeV). These diagnostics were used together to characterize four distinct x-ray generation mechanisms: Betatron, laser and electron driven bremsstrahlung, and inverse Compton scattering. These x-ray sources span a total energy range of more than 1 MeV proving useful in a wide variety of applications.

The forward fit method provides a way to extrapolate an energy spectrum given an analytical function to describes the x-ray energy distribution. The Ross Pair and DAT methods provide a way to directly measure the photon flux in a narrow energy bin without needing to assume a distribution function. These discrete points are then fit using the same equation used in forward fitting to provide a separate independent measure of the x-ray energy spectrum. Combining all of these methods provides a solution band in which the x-ray spectrum can exist. This technique allows a robust method of characterizing an x-ray source in a high noise environment, like that of SM-LWFA.

Large laser facilities like NIF and OMEGA, are capable of creating experimentally

unexplored conditions and states of matter valuable to HED, ICF, and laboratory astrophysics. These new experimental capabilities bring with them a need for a broadband x-ray source capable of probing the various transient states of matter being created. Laser wakefield accelerators are a promising tunable driver for x-ray sources at these facilities and have been demonstrated to produce a broad range of x-ray energies.

Chapter 6

Applications of SM-LWFA driven x-ray sources using picosecond lasers

6.1 Introduction

Using the understanding gained from work on the contribution of DLA in a SM-LWFA as well as the tools created for analyzing x-ray sources, we begin work on applications of the SM-LWFA x-ray source. In this chapter we will explore three static radiography objects used to demonstrate the ability to tune x-ray energy and photon number to fit an intended application. This is accomplished by choosing a target material which utilizes the strengths of betatron, ICS, and bremsstrahlung radiation for an intended radiography test object. For example, a high-Z, dense radiography target requires high energy x-rays to pass through the object and create and image necessitating the use of a thick bremsstrahlung converter target.

6.2 Experimental Configuration

The experiments focusing on applications for SM-LWFA driven x-ray sources were preformed on the Titan laser system at Lawrence Livermore National Laboratory. Here, we modified our experimental configuration after the gas jet to allow for static radiography, shown in fig. 6.1. We have the option of placing solid targets directly after the gas jet which drives the SM-LWFA allowing for inverse compton scattering and electron driven bremsstrahlung radiation to be utilized. One of three possible radiography test objects are placed 65 cm from the gas jet, after a 1 T magnet used to sweep electrons out of the x-ray

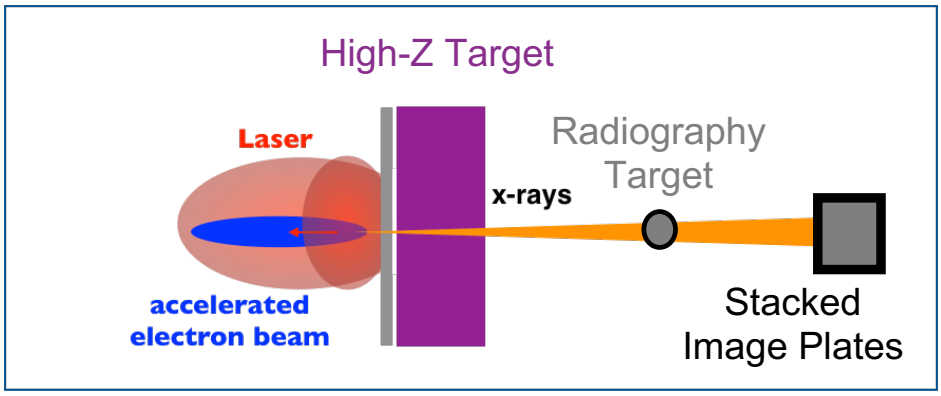

Figure 6.1: Experimental configuration. A high-Z target is placed after the SM-LWFA to generate bremsstrahlung radiation. A radiography target is placed after the high-Z target and the image is captured on a stack of 12 BAS-MS image plates.

beam path, and the signal is collected in a stacked BAS-MS image plate (IP) [76] detector. The IP detector uses a stack of 12 100 μm tin and IP pairs. The images captured on each IP is corrected for rotation, magnification, and position in post processing to create a final image with improved signal to noise (SNR) than a single IP can provide.

The first radiography object used in this experiment are the Kings Resolution Target (KRT) shown in fig. 6.2 (a). This target has variable slit spacing from 1 mm at the largest to 50 μm in sets of 5 for each size. There is also a pinhole array located next to the lines which have diameters from 500 μm at largest to 50 μm at the smallest. These are arranged from bottom to top in sets of 10 pinholes for each size. The KRT pattern was laser cut into a 500 μm W blank that is 2 by 6 cm by General Atomics (GA). This radiography is designed for low to medium keV x-ray energies and can be used to determine the resolution of the x-ray source.

The second radiography target, the halfraum, used is a 5.75 by 4.72 mm hollow Au cylinder with 30 μm thick walls. To imitate a large fuel capsule inside a gold hahlraum used in many ICF experiments at the NIF, a 400 μm radius W sphere was suspended inside the

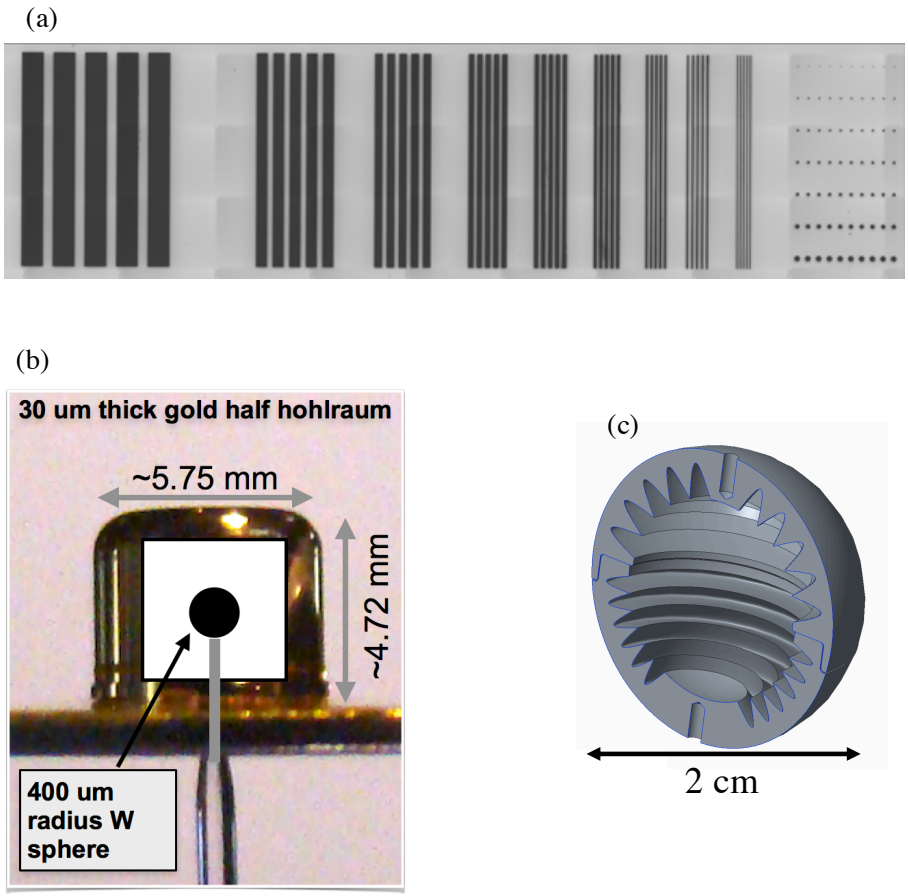

Figure 6.2: (a) Metrology image of the KRT which has variable line width slits on the left and a pinhole array on the right. (b) An image of a 30 μm thick gold half hahlraum with a 400 μm radius W sphere suspended inside by a glass stalk. (c) CAD image of the IQI which is a hollow lead sphere with a circular patter cut into the inside edges.

gold cylinder. The halfraum can be seen in fig. 6.2 (b). The halfraum is used to demonstrate the tuning of the SM-LWFA driven x-ray source by varying the target type and thickness after the SM-LWFA. The clarity of the radiograph produced is representative of large fuel cell and double shell experiments on the NIF.

The image quality indicator, IQI, shown in fig. 6.2 was the final target used and is

modeled after the radiography target used in prior MeV x-ray experiments [79]. This object is a 2 cm hollow lead sphere with a radial patter cut into the inside walls of the object. The average radial density for the object is 7.65 g/cm^2. This radiography object is used to test the highest energy x-rays produced in our experiments and to show improvement over direct laser-solid bremsstrahlung x-ray sources.

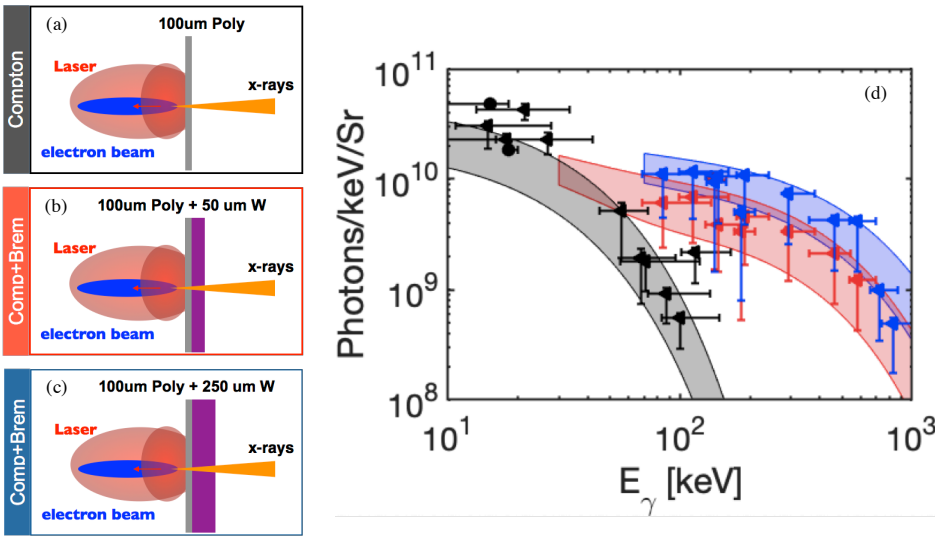

Figure 6.3: Shows how the x-ray spectrum changes with the chosen x-ray generation mechanism and target choice. (a-c) is a cartoon representation of each target used where the laser pulse is shown in red, the SM-LWFA electrons are in blue, the target is grey, and the emitted x-rays are in orange. The main x-ray mechanism is listed on the left: Compton (black), and Compton plus Bremsstrahlung (orange and blue) corresponding to the spectra in (d) of the same color.

Fig. 6.3 shows example x-ray spectra, using the techniques detailed in chapter 5, from this experiment demonstrating how we tune the x-ray energy and photon number by changing the dominant x-ray generation mechanism. Fig. 6.3 (a) shows the configuration used for Inverse Compton scatter. Here we use a 100 μm plastic target to act as a plasma mirror, reflecting the main laser pulse back on the accelerated electron beam, and generating an x-ray spectrum shown in black (d). This x-ray mechanism provides the highest photon

number,$\approx 3 \times 10^{10}$ photons/keV/Sr at 10-30 keV and should be utilized for radiography applications of low to medium density. By placing high-Z targets, 50 and 250 μm W, after the SM-LWFA we convert more high energy electrons into x-rays and enhance the high energy, > 100 keV, photon production. Shown in fig. 6.3 (d) as red, 50 μm, and blue, 250 μm, the addition of a high-Z W target increases the high energy photons to MeV energies while maintaining $> 10^9$ photons/keV/Sr. The abilitiy to change the x-ray energy spectra to fit an intended application in this fashion using the same electron beam driver shows great promise.

6.3 Radiography Applications and Results

6.3.1 KRT Radiography

The KRT is a radiography test object designed to provide information on the source size of the x-ray mechanism used. The varying width slits were laser cut by General Atomics into a 500 μm thick tungsten blank. Fig. 6.4 (a) shows an experimental radiograph of this object using a 250 μm W target to generate SM-LWFA bremsstrahlung radiation. Due to manufacturing limitations, the material width between each of the slits is not the same width as that of the slit. Additionally, due to the extreme focus needed in the laser to cut through 500 μm W, the edges of each slit are not straight edges. The V shape caused by the laser cutting causes a gradient accross the edge of the slit as a function of x-ray energy.

To more accurately determine the x-ray source size from this radiography object, an x-ray ray tracing program, HADES, was utilized. A model of the KRT was created in CAD and used as the target in a HADES simulation. The experimentally measured x-ray spectrum and photon number for a 250 μm bremsstrahlung source is used as the input to generate the image in fig. 6.4 (b). Lineouts from the center of each image, black and red in (a) and (b) respectively, are plotted in fig. 6.4 (c) to directly compare the experimental radiograph with the synthetic HADES image. By varying the source size of the x-rays in HADES and

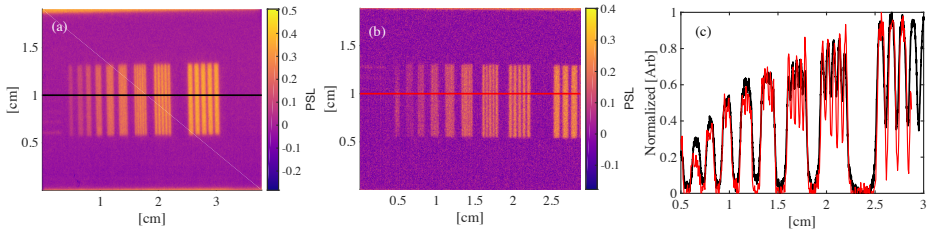

Figure 6.4: (a) Experimental radiograph of the KRT using a 250 μm W foil target at the end of the gas jet. The lineout region for (c) is indicated as a black line. (b) HADES synthetic radiograph of the KRT using experimentally measured x-ray distribution and photon number. A lineout taken accross the image is indicated in red. (c) Comparing the normalized lineouts from (a) and (b), black and red respectively.

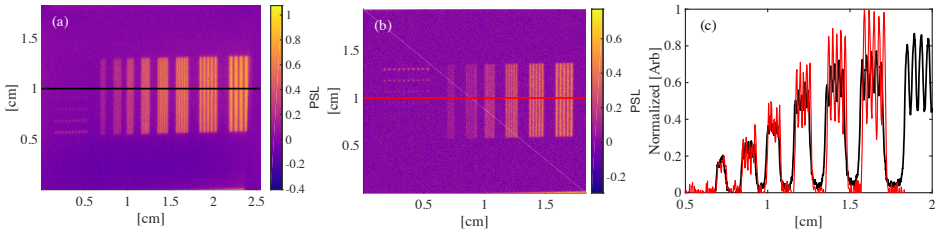

Figure 6.5: (a) Experimental radiograph of the KRT using a 25 μm Al foil target at the end of the gas jet. The lineout region for (c) is indicated as a black line. (b) HADES synthetic radiograph of the KRT using experimentally meausred x-ray distribution and photon number. A lineout taken accross the image is indicated in red. (c) Comparing the normalized lineouts from (a) and (b), black and red respectively.

comparing the KRT features, the experimental source size can be determined. Additional work is needed on this method to produce accurate results, however, the method shows promise and the simulation framework has for HADES simulations is complete. As shown in (c), the resolution of the HADES image doesn't match perfectly with the experimental image. Additional work can be done to the KRT CAD model to improve the tapering at the edges of each slit as well as iterations to more accuratly capture the photon yield.

Fig. 6.5 shows a second example KRT radiograph using a 25 μm Al target to generate SM-LWFA driven bremsstrahlung radiation. The thinner, lower-Z material was expected

to produce a softer x-ray spectrum with a smaller source size than that of the 250 μm target shown in fig. 6.4. The photon number and and x-ray energy using the Al target does appear to be lower in comparison, however, the impact on the KRT radiograph seems small. Additional work is needed to more accurately determine the source size using HADES synthetic radiographs.

6.3.2 Halfraum Radiography

The halfraum radiography object is a static target with similar attributes to an intended application on the NIF during ICF experiments. Some NIF experiments use dense, double shell fuel capsules suspended inside a high-Z hahlraum. To simulate this object we used half of a 30 μm thick walled Au cylinder as shown in fig. 6.1 (b). A 400 μm radius W sphere was suspended inside this cylinder on a glass stalk. Radiographs of this object were taken using several different targets to demonstrate and study the abilitiy to tune the SM-LWFA driven x-ray source.

Following the schematic in fig. 6.6 (a), the Inverse Compton scattering x-ray mechanism was utilized by placing a 100 *upmu*m plastic target at the exit of the SM-LWFA to generate a radiograph of the halfraum. The expected x-ray spectrum generated through this mechanism is shown in fig. 6.3. The resulting radiograph is shown in fig. 6.6 (d) and a lineout of the radiograph in (g). The ICS spectrum does not generate high enough x-ray energies with a great enough photon number to generate a radiograph of the tungesten sphere in the halfraum. instead, we see a shadowfraph of the gold cylindar with a $\times 6$ signal to noise (SNR) ratio. The edges of the cylinder are well defined suggesting a small source size, however, additional work is needed to determine the source size using the rounded edge of the gold cylinder.

Placing a 50 *upmu*m W target at the end of the SM-LWFA, shown in fig. 6.6 (b), allows additional energy to be extracted from the SM-LWFA electron beam and generates a

higher energy x-ray spectrum. This source is used to radiograph the halfraum, fig. 6.6 (e), and a similarly a lineout is taken from the center, fig. 6.6 (h). An improvement of the ICS source is imedietly apparent, as now the W sphere can be seen through the gold cylinder walls. The lineout indicates a $\times 3$ SNR between the vacuum and gold wall as well as the gold wall and W sphere. Additional work is needed to determine the source size for this source using the W sphere and the edge of the gold cylinder.

Finally, the x-ray spectrum is pushed to higher energies by using a 250 μm W target,fig. 6.6 (c), and the resulting radiograph is shown in fig. 6.6 (f,i). This x-ray source is now becoming to high energy to provide an optimal radiograph of the halfraum which can be seen through the diminishing SNR of $\times 2$ between the vacuum and gold walls and $\times 1.5$ between the gold and W sphere. The SNR is reduced in this radiograph for two reason: First, the x-ray energies are becoming too high to be attenuated by the halfraum object allowing the x-ray photons to pass through the object unobstructed; and second, the image plate detector used to capture the radiograph is not as sensitive to the high energy x-rays requiring higher x-ray numbers to result in a similarly clear radiograph. These complications can be accounted for by using different x-ray detectors and choosing a higher-Z radiogrpahy object.

6.3.3 IQI Radiography

The halfraum radiography object and single image plate detector began to show its limitations when using thick, high-Z bremmstrahlung targets requiring a high-Z radiography object and new detector to be used to continue testing the SM-LWFA x-ray source. For this, we use the image quality indicator (IQI) radiography test object which has an average areal density of 7.65 g/cc. To radiograph this object, a near MeV x-ray spectrum is needed and so we used 1 mm thick W targets to generate MeV bremsstrahlung radiation. Fig. 6.7 (a) shows the resulting radiograph using the 1 mm thick W target driven by SM-LWFA electrons.

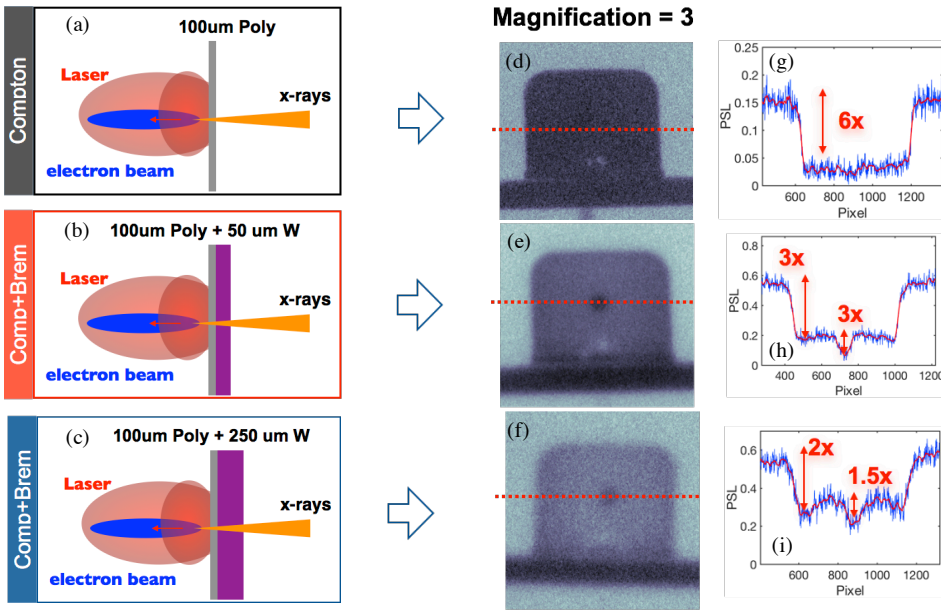

Figure 6.6: Shows how the radiograph of a W sphere shielded by 60 µm of gold changes with x-ray generation mechanism and target. (a-c) is a cartoon representation of each target used where the laser pulse is shown in red, the SM-LWFA electrons are in blue, the target is grey, and the emitted x-rays are in orange. The main x-ray mechanism is listed to the left of the cartoon: Compton (black), and Compton plus Bremsstrahlung for 50 (orange) and 250 µm W (blue) corresponding to the radiograph and lineout in (d,g), (c,h), and (f,i) respectively. The lineout locations plotted in (g-i) are indicated as red lines in (d-f).

The image was captured on a stack of 12 image plates which are corrected for rotation, magnification, and translation before being summed in post proccessing. Since each image plate individually detects a small number of the high energy x-rays, the summation of 12 image plates allows for an image with a much higher SNR. The resulting radiograph clearly shows features of the IQI interior and a lineout is plotting in (c), black. Shown in fig. 6.7 (b) is a radiograph generated using a laser-solid interaction by placing a 1 mm W target directly at laser focus. The resulting radiograph has a lower SNR and contrast than that of the SM-LWFA source and can be seen directly in (c) where lineouts for both sources are plotted together. The conlusion drawn from this comparison is that using a SM-LWFA to first

generate electrons produces a better radiograph of the IQI image than that of a laser-solid interaction.

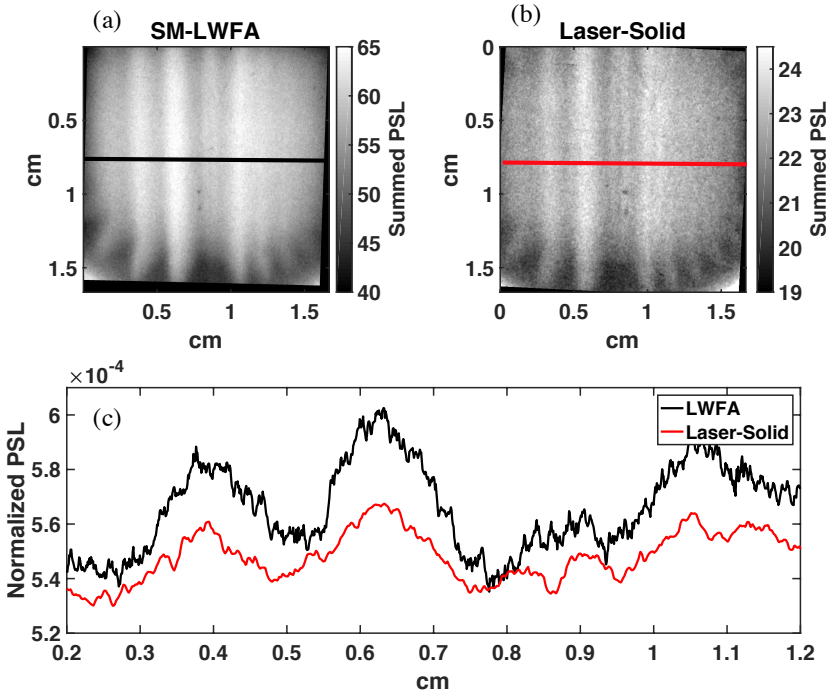

Figure 6.7: Experimental radiographs of the IQI using SM-LWFA (a) driven x-rays and direct laser-solid (b) with a 1.5 mm W target to generate MeV bremsstrahlung x-rays. The normalized signal is shown as a lineout in (c) and indicates a higher contrast and signal to noise ration with the SM-LWFA driver.

6.4 Summary

In conclusion, the SM-LWFA x-ray source developed on the Titan laser systems provides a radiography platform for several applications. We have shown in this chapter the versatility of this x-ray source from low keV x-ray energy applications with the KRT to MeV energies by imaging the IQI. The halfraum radiography target demonstrates the ability to image dense fuel capsules through high-Z shielding typical in ICF experiments at NIF. The

source is tune-able by varying the bremstrahlung converter target material and thickness with enough versatility to match an intended application. This source also improves upon existing laser-solid methods of generating MeV radiography sources. While additional work is needed to fully characterize the results presented in this chapter, the SM-LWFA x-ray source has demonstrated versatility in a wide variety of applications.

Chapter 7

X-Ray Characterization from Over-dense Plasma Acceleration

7.1 Introduction

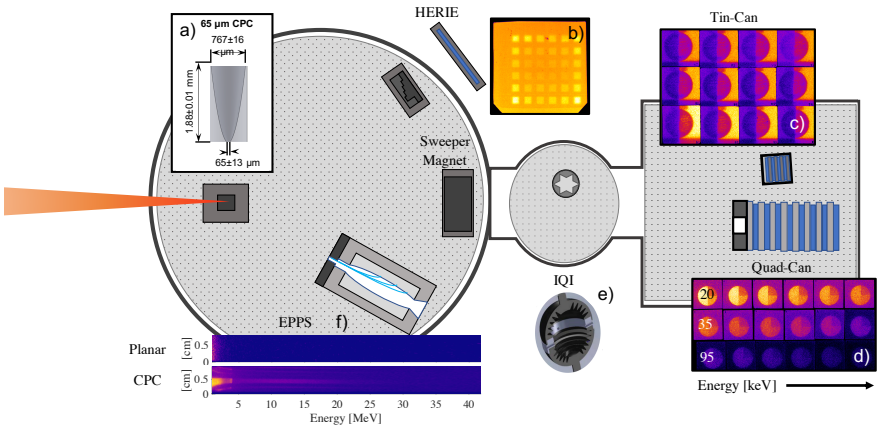

Figure 7.1: Experimental Set up. (A) Image of the 65 µm CPC which is then fixed to a 2 mm Ta target. (B) Raw image plate data from the LTSF diagnostic placed at a -35 degree angle from laser axis. (C) Raw image plate data from the radiography stacked image plate detector. (D) Raw image plate data from the high energy x-ray detector, the quad-can. (E) Cad model of the IQI radiography test object. (F) Raw electron Spectra measured with the EPPS for Planar (top) and CPC (bottom) targets.

[1] X-ray sources driven by SM-LWFA has been shown in prior chapters to generate high energy photons useful for a variety of static radiography applications. In this chap-

[1]This chapter contains published information from: P. M. King, et. al., Submitted to High Energy Density Science (2021) of which I am the first author. My contribution to this work included experimental planning, execution, data analysis, and writing the published manuscript.

ter we will explore MeV x-rays and radiography applications using laser-solid interactions. Bremsstrahlung radiation, produced by the interaction of a relativistic laser pulse with a solid target, provides a promising method of producing compact, MeV x-ray sources with sub millimeter source sizes enabling radiographic capabilities of high areal density objects while maintaining high resolutions [31]. To date, laser-solid bremsstrahlung sources have been limited in their yields, reducing the abilitiy to radiograph high-areal density objects in the most demanding MeV radiography applications in industry, high energy density (HED), and inertial confinement fusion (ICF) experiments while maintaining a small enough source size [80, 81]. On approach to improving the low photon number and MeV photon energy, experimental efforts have focused on designing complex targets to increase and control the hot electron population and energy of the laser-solid interactions. X-ray photon number and energy through bremsstrahlung radiation increases proportionally with electron number and energy [45]. These target schemes include adding preformed plasma to the front of a high-Z bremsstrahlung target [82, 79, 83], as well as more complex nano-wire and micro channel array targets [84, 85, 86, 87]. These methods seek to increase the laser to hot electron energy coupling through a low density plasma [84] or guiding the laser pulse to increase the high intensity interaction length [88] before reaching the solid density surface of the high-Z bremsstrahlung target. While several of these methods have shown promise, they require relativistic laser intensities ($>> 10^{18}$ W/cm^2) typically generated with a low $f\#$ focusing optic not available at all laser facilities. Additionally, many of these targets haven't been tested at picosecond, kilojoule class laser facilities or have fallen short in being able to produce high enough photon counts for some of the most demanding applications [89].

A novel approach approach to increasing the photon production in a laser-solid interaction utilizes the addition of a compound parabolic concentrator (CPC) fixed to the surface of a high-Z target [90]. Assuming geometrical focusing, the CPC curvature re-points the incident rays within a given angular tolerance to a smaller radius in a single reflection, for

sufficiently short laser pulses with steep or short pre-plasma conditions. Work with longer pulse laser systems show that plasma confinement in the CPC adds additional enhancements not related to the geometric focusing [91]. Additionally, due to the large area of acceptance, the CPC targets concentrate additional laser energy from the edges of the laser pulse which are normally of a lower intensity. The combined geometric focusing and capture of additional laser energy provide a large increase in laser intensity at the tip of the CPC. CPC-enhanced targets are options for facilities which do not have access to low $f\#$ focusing optics, like NIF-ARC, and facilities with long focal length lasers.

Bremmstrahlung x-ray emission from a laser-solid interaction can be approximated by an exponential distribution ($Ae^{-E/T}$, where A is the photon number, E is the energy of the photon, and T is the effective temperature of the distribution). A depends upon the hot electron number and temperature in the solid target. By increasing the hot electron number and temperature, the resulting bremsstrahlung radiation will be similarly enhanced [45]. When interacting with a solid target, laser energy is transferred to the electrons primarily through the ponderomotive force. In cases of steep density gradients, the resulting Maxwellian electron distribution can be described by a ponderomotive scaling where: $T_{pond} = m_e c\left(\sqrt{1+a_0^2/2}-1\right)$ [MeV] where m_e is the electron rest mass, c is the speed of light, and the normalized vector potential of the laser $a_0 \approx 0.85\left(I_{18}\lambda_\mu^2\right)^{1/2}$, where I_{18} is the laser intensity [10^{18} W/cm^2] and λ_μ is the laser wavelength [μm] [92]. The ponderomotive scaling is accurate for high intensity laser-solid interactions with steep density profiles.

Here, we show a direct improvement in the production of hot electron temperature and number compared to planar interactions, using an identical drive laser and high-Z target [93]. By including a CPC, this work reports an average electron temperature increase of x9 from a planar $kT_e = 0.51 \pm 0.25$ MeV to a CPC $kT_e = 4.4 \pm 1.3$ MeV target using identical laser parameters. In this manuscript, we show that the CPC target improves high energy bremmstrahlung emission in photon number, integrated energy, and fitted tempera-

ture by x2 over planar target interactions while maintaining the same, or better, source size during the same experimental campaign as the electron enhancement. This improvement in bremsstrahlung emission shows an enhancement of 1.53 in the signal to noise (SNR) of high areal density static radiography applications. Additionally, utilizing x-ray ray tracing programs enhances our ability to predict the quality of high areal density radiographs and plan applications accordingly.

7.2 Experimental Overview

Our experiment was conducted on Texas Petawatt (TPW) laser system at the University of Texas at Austin. The TPW is a 1057 nm, 153 ± 13 fs, 109.2 ± 7.6 J laser system with an $f/40$ spherical focusing optic with 50% of the energy contained in a 89.6 ± 7.4μm radius. As shown in figure 7.1, the main laser pulse is focused onto the surface of a target package consisting of 2mm thick tungsten disks with and without CPCs. The CPCs are 3D printed plastic made by General Atomics and designed by scientists at LLNL [90]. The CPC targets have an entrance aperature of 805μm and a tip size of 65μm, focusing >90% of the laser energy into the spot with perfect alignment. An electron positron spectrometer (EPPS [94]) is fielded at a -35 degree angle from the laser axis. There are 2 different x-ray diagnostics fielded to provide angular source information as well as redundancy in x-ray energy measurements. The quad-can, a modular stack calorimeter made of alternating absorbers and image plates (IP) designed by University of Texas at Austin and Helmholtz-Zentrum Dresden-Rossendorf scientists [cite paper], is placed 2 degrees from the laser axis 2 meters from the source to provide the spectral information used for the radiography simulations. An IP-based detector, Livermore tantalum step filter (LTSF) [72], sensitive to x-ray energies < 2 MeV, is fielded -35 degrees from the laser axis in the main target chamber. Finally, a radiography test object, the image quality indicator (IQI), is placed behind a wide aperture 0.2 T magnet, used to remove on-axis electrons, -1 degree from the laser axis 50 cm from the

source. The Tin-Cannon, a 12 layer stacked 100 μm tin - IP pair detector, used to increase image resolution [95], records the high energy radiograph of the IQI.

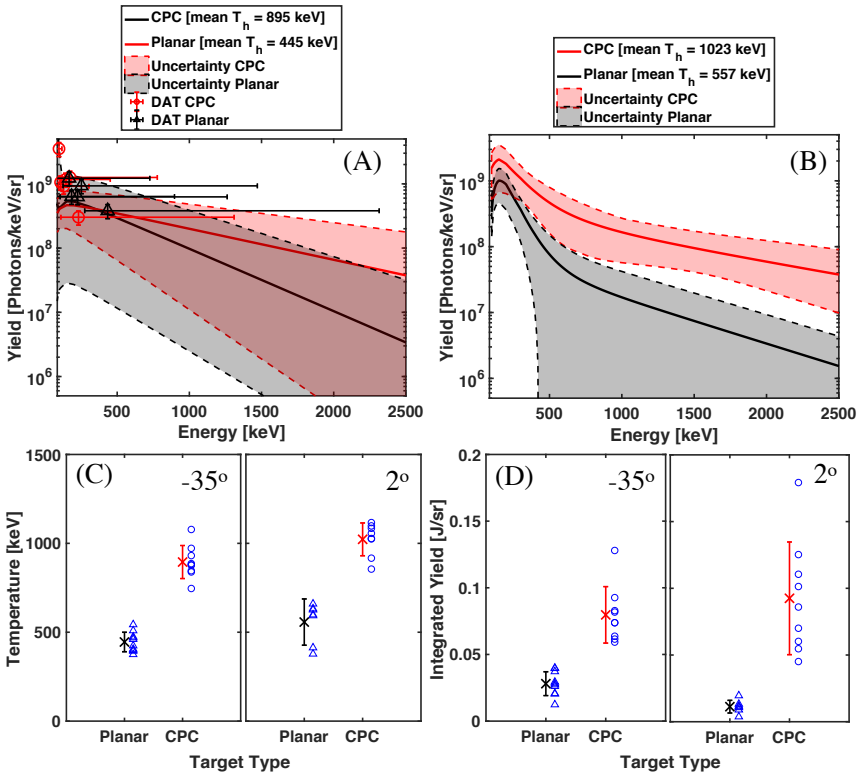

Figure 7.2: (A) The mean x-ray spectrum from the LTSF diagnostic for CPC and planar targets, solid lines and the uncertainty due to detector energy sensitivity, shaded regions. The data points are experimentally obtained through the DAT analysis method [1]. (B) The mean x-ray spectrum from the quad-cann diagnostic for CPC and planar targets, solid lines, and the detector uncertainty, shaded regions. (C) The high energy temperature, T_h for planar and CPC targets measured at -35 and 2 degrees from laser axis. The blue open circles are the individual data points with the mean values and standard deviation plotted in black (red) for planar (CPC) targets. (D) The integrated yield for planar and CPC targets at -35 and 2 degrees from laser axis. The blue open circles are the individual data points with the mean values and standard deviation plotted in black (red) for planar (CPC) targets.

7.3 CPC Bremsstrahlung X-ray Source Characterization

The use of CPCs in laser solid interactions shows up to ×9 improvement in the hot electron [93] production and ×2 in x-ray energy and yield above 1 MeV compared to the planar targets. Figure 7.2 shows the mean result of 9 (10) shots using CPCs (planar) on 2mm thick Ta targets during this campaign. The x-ray spectrum for each shot is approximated as a two temperature spectrum of the form $C_1 e^{-E/T_c} + C_2 e^{-E/T_h}$, where $C_{1,2}$ are fitting parameters for the photon number [photons/keV/Sr], E is the photon energy [keV], and T_c, T_h are fitting parameters for the temperature [keV]. (A) and (B) show the mean x-ray spectrum from the -35 and 2 degree x-ray spectrometers using forward fitting analysis methods [1, 96]. The analysis results in a mean measured x-ray hot temperature (T_h) of 895±93 keV and 1023±111 keV for the LTSF and quad-can detectors, respectively. The results from both detectors agree very closely with one another while indicating up to a 3x reduction in photons/keV/Sr in the LTSF detector compared to the quad-can. This reduction in photon number between the detectors is likely caused by the angular distribution of the emitted bremsstrahlung radiation, but may also be due to added background noise in the raw LTSF data due to not being behind a sweeper magnet to deflect low energy electrons. Both detectors show an increase in production of high energy photons over that of a planar target interaction, ×2 (×1.8) for the LTSF (quad-can) detector. The mean T_h for CPC and Planar interactions for each detector is plotted in (C) and indicates a ×2 increase in the fitted temperature when using a CPC. Additionally, the integrated yield of each measured spectrum is plotted in (D) which again shows an improvement, $>$ ×2, in CPC photon production over planar target interactions. We hypothesize that the larger uncertainty in the integrated energy measurement between the CPC and planar targets is caused by target alignment and laser pointing fluctuations causing the laser to focus off center of the CPC. Improvement in CPC target alignment and laser pointing stability will improve the CPC uncertainties.

Target and x-ray detection limitations are the likely cause for the discrepancy in the

×2 improvement over planar targets in high energy bremsstrahlung photons and the ×9 improvement in hot electron production seen in [93]. Our x-ray spectrometers become less sensitive at x-ray energies above a few MeV and depend upon the low energy content to provide spectral reconstruction. We hypothesize that, while the 2 mm Ta target used to generate bremsstrahlung radiation in this experiment is a good match for generating high energy x-rays for the measured 4 MeV hot electron temperatures, low energy electrons and x-rays wont escape the target thus reducing our detection sensitivity. More work in optimizing target thickness with laser driver is needed to more closely match the photon enhancements with the measured ×9 electron improvement. Additionally, Future work to measure the high energy tail of the x-ray distribution is needed to better understand the production disparity. This may be accomplished using nuclear activation measurements.

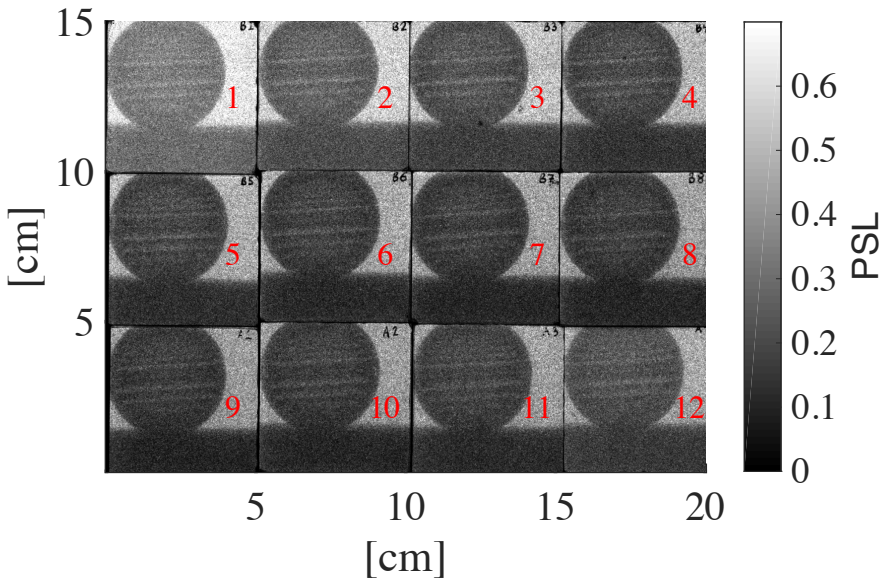

Figure 7.3: Raw experimental images of the IQI recorded on the Tin-Cannon detector. 1 through 12 indicates the IP location in the stack with 1 being the front and 12 being the back IP.

7.4 Simulated and Experimental MeV Radiography

The high energy x-ray production of CPC-enhanced laser-solid interactions show an improvement in the quality of radiographs possible for high-Z objects. Figure 7.3 shows experimental radiographs of the IQI test image using the Tin-Cannon. To increase the absorption of MeV x-rays in IP [76], a stacked detector is used to improve the signal to noise (SNR) via enhancements in florescence and Compton scattering in a high-Z material. Each image plate records a radiograph which is then corrected for rotation, translation, and magnification in post processing before being summed to improved the signal to noise of a final radiograph.

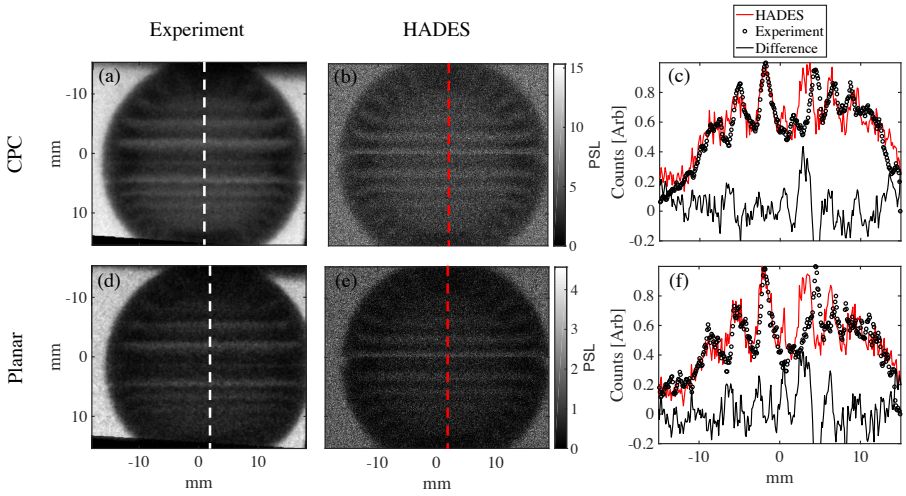

Figure 7.4: (A, B) Experimental IQI radiograph of the CPC and Planar target (left and right, respectively) after summing the deposited signal on all 12 layers of the stack detector. (C, D) Synthetic radiograph of the IQI using the CPC and planar target, respectively, created using the HADES code with experimentally measured x-ray energy and photon number. Line-outs through the center of the CPC (E) and planar (F) experimental and synthetic radiographs (indicated as dashed lines in A-D).

An ideal radiograph will have a high SNR, determined by comparing the peak signal to the noise floor of an image, as well as high contrast, comparing local peak to trough signal

of a feature. A low temperature x-ray spectrum will provide high contrast images of the shadow of an object, shadography, but have low contrast of internal features. However, an x-ray spectrum with too high a temperature will not attenuate enough through an object providing a low contrast image inside and out. An ideal radiograph will have the correct x-ray spectral content and photon number to provide high contrast inside and outside of the target object while maintaining a high SNR. Figure 7.4 shows the resulting combined IP radiograph of one shot each using a CPC (A) and planar (d) target. The SNR of the experimental CPC and planar radiographs is 16.5 and 10.8, respectively, and a peak contrast of the internal features of 1.8 (2.5) for the CPC (Planar) source. The higher contrast from the planar source is due to the lower energy content of the planar x-ray spectrum.

7.4.1 Source Size Calculation

The source size of each target is obtained by using a forward fitting method of the radially averaged edge of the IQI image [97]. The radial lineout of each radiograph is compared to an analyical lineout obtained through the following equations:

$$Sig(x) = I_0 \int Spec(E) e^{-\mu(E)\rho dl(x)} IPs(E) dE \tag{7.1}$$

Where $Sig(x)$ is the analytic signal, $Spec(E)$ is the x-ray spectrum, $\mu(E)$ is the attenuation coefficient, ρ is the material density, $dl(x)$ is the x-ray pathlength, and $IPs(E)$ is the energy dependant IP absorption. $Signal(x)$ is then convolved with a Gaussian source where the width of the Gaussian is a fit variable. The convolved solution is compared to the experimental image to determine the source size assuming a guassian source profile. Using this methodology results in a source size of 706 and 730 μm for CPC and planar targets, respectively. This result is similar to the measured source size of prior experiments [31] providing confidence in the measurement.

7.4.2 HADES Simulations

To improve upon radiography target design and experimental planning of the CPC x-ray source, an x-ray ray tracing program developed at Lawrence Livermore National Laboratory, HADES [98], is utilized. The experimentally measured x-ray energy spectra, source size, and integrated photon number are used as inputs to HADES. An IQI model, using a configuration with an Al band installed in the center, which was not present for the experiment was used. This creates a high signal region separating the two hemispheres. The energy deposition and point spread function of each of the 12 layers of the IP detector stack used in the experiment were simulated using a monte-carlo code, Monte-Carlo N-Particles (MCNP) [99], and included in the HADES program. HADES then outputs 12 images, one for each IP in the stack, which are run through the same post processing as the experimental image to correct for translation, rotation, and magnification before being summed to produce a single synthetic radiograph. The results of this process are shown in figure 7.4 (b, e) using the x-ray characteristics for a CPC and planar target, respectively. These images have been altered in post processing to remove the Al ring between each IQI hemisphere to more closely match the experimental image. Additionally, the CPC (planar) HADES radiographs have been multiplied by a factor of 500 (1000) to be plotted on the same color scale as the experimental images, Fig. 7.4 (a,d).

7.4.3 Radiography Discussion

The HADES synthetic radiographs qualitatively are a good match to the experimentally obtained images shown in figure 7.4 (a, d). A lineout through the center of each experimental (white dashed line) and HADES (red dashed line) radiograph is presented in fig. 7.4 for the CPC (c) and planar (f) sources. The synthetic lineouts were modified to remove signal from the Al ring in the CAD model that wasn't present in the experimental IQI. The synthetic lineouts show good agreement to the experimentally measured radiographs in

the top hemisphere (negative positional values [mm]) but diverge where the CAD model differs from the experimental object in the lower hemisphere (positive positional values [mm]). This close agreement provides confidence in the measured x-ray spectra, photon number, and source size which were used as input data to the HADES code. The added statistical noise of the synthetic HADES radiographs is likely due inaccuracies in the image plate modeling and work to improve this statistical noise is ongoing.

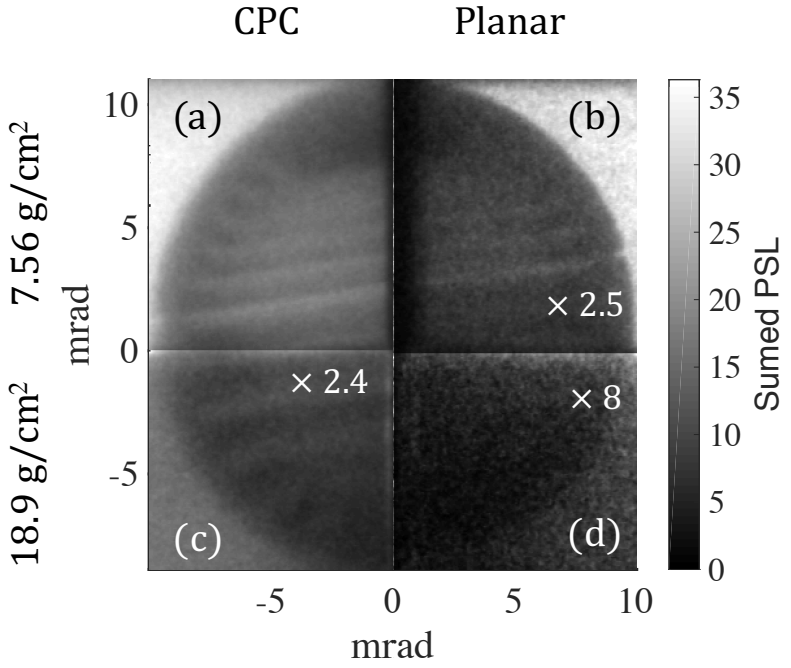

Figure 7.5: Experimental radiograph using a CPC (left) and planar target (right) through 0 (a,b) and 1 (c,d) cm of lead. The areial densiy of the IQI (lead) is 7.56 (11.34) g/cm^2 which totals 7.56 and 18.9 g/cm^2 in regions i and ii, respectively. The numbers indicate the multiplicative factor used to plot on the same color bar.

To further explore the higher energy photons generated by the CPC source, additional high-Z material is placed in front of the Tin-Cannon. Shown in fig 7.5, the CPC (left) and planar (right) sources are used to radiograph the IQI with 0, and 1 cm of lead in front of the detector, resulting in a total areal density of 7.56 and 18.9 g/cm^2 for quadrants (a,b), and

(c,d), respectively. Comparing the experimental results in quadrants for the CPC (c) and planar (d) sources indicates an improvement of the CPC radiograph to the planar radiograph by a factor of 3 in yield. Features can still be seen through the additional 1 cm (11.34 g/cm^2) of lead shielding for the CPC source while it is already difficult to see the edge of the IQI for the planar source. Additionally, the signals in quadrants (b) and (d) of the planar source had to be enhanced by multiplicative factors, 2.5 and 8 respectively, to be plotted on the same color scale as the higher yield CPC source.

7.5 Summary

In summary, CPC enhanced targets show a more than 2× improvement over planar targets in the production of MeV photons while maintaining the source size for high resolution radiography applications. The enhanced MeV x-ray source is capable of radiographing high-Z objects through as much as 18.9 g/cm^2 of shielding using 120 J of laser energy. Increasing the laser energy to those found at large laser facilities like NIF-ARC and OMEGA-EP, promise to increase the MeV x-ray production further and solidifies the usefulness of CPC targets to meet the needs of indusrial, HED, and ICF applications. The robustness of the HADES package also provides a valuable tool to design experiments and radiography targets for future experiments while also acting as a redundant source of verifying experimentally measured x-ray characteristics.

Bibliography

[1] P. M. King, N. Lemos, J. L. Shaw, A. L. Milder, K. A. Marsh, A. Pak, B. M. Hegelich, P. Michel, J. Moody, C. Joshi, and F. Albert. X-ray analysis methods for sources from self-modulated laser wakefield acceleration driven by picosecond lasers. *Review of Scientific Instruments*, 90(3):033503, 2019.

[2] T. Tajima and J. M. Dawson. Laser electron accelerator. *Phys. Rev. Lett.*, 43:267–270, Jul 1979.

[3] E. Esarey, C. B. Schroeder, and W. P. Leemans. Physics of laser-driven plasma-based electron accelerators. *Rev. Mod. Phys.*, 81:1229–1285, Aug 2009.

[4] S. Corde, K. Ta Phuoc, G. Lambert, R. Fitour, V. Malka, A. Rousse, A. Beck, and E. Lefebvre. Femtosecond x rays from laser-plasma accelerators. *Rev. Mod. Phys.*, 85:1–48, Jan 2013.

[5] J. M. Cole, J. C. Wood, N. C. Lopes, K. Poder, R. L. Abel, S. Alatabi, J. S. J. Bryant, A. Jin, S. Kneip, K. Mecseki, D. R. Symes, S. P. D. Mangles, and Z. Najmudin. Laser-wakefield accelerators as hard x-ray sources for 3d medical imaging of human bone. *Scientific Reports*, 5:13244 EP –, 08 2015.

[6] J. C. Wood, D. J. Chapman, K. Poder, N. C. Lopes, M. E. Rutherford, T. G. White, F. Albert, K. T. Behm, N. Booth, J. S. J. Bryant, P. S. Foster, S. Glenzer, E. Hill, K. Krushelnick, Z. Najmudin, B. B. Pollock, S. Rose, W. Schumaker, R. H. H. Scott, M. Sherlock, A. G. R. Thomas, Z. Zhao, D. E. Eakins, and S. P. D. Mangles. Ultra-fast imaging of laser driven shock waves using betatron x-rays from a laser wakefield accelerator. *Scientific Reports*, 8(1):11010, 2018.

[7] A. E. Hussein, N. Senabulya, Y. Ma, M. J. V. Streeter, B. Kettle, S. J. D. Dann, F. Albert, N. Bourgeois, S. Cipiccia, J. M. Cole, O. Finlay, E. Gerstmayr, I. Gallardo González, A. Higginbotham, D. A. Jaroszynski, K. Falk, K. Krushelnick, N. Lemos, N. C. Lopes, C. Lumsdon, O. Lundh, S. P. D. Mangles, Z. Najmudin, P. P. Rajeev, C. M. Schlepütz, M. Shahzad, M. Smid, R. Spesyvtsev, D. R. Symes, G. Vieux, L. Willingale, J. C. Wood, A. J. Shahani, and A. G. R. Thomas. Laser-wakefield accelerators for high-resolution x-ray imaging of complex microstructures. *Scientific Reports*, 9(1):3249, 2019.

[8] Félicie Albert and Alec G R Thomas. Applications of laser wakefield accelerator-based light sources. *Plasma Physics and Controlled Fusion*, 58(10):103001, sep 2016.

[9] Wei Lu and et al. *Phys. Rev. ST - Accel. Beams*, 10:061301, 2007.

[10] John Lindl. Development of the indirect-drive approach to inertial confinement fusion and the target physics basis for ignition and gain. *Physics of Plasmas*, 2(11):3933–4024, 1995.

[11] J. D. Lindl and E. I. Moses. Special topic: Plans for the national ignition campaign (nic) on the national ignition facility (nif): On the threshold of initiating ignition experiments. *Physics of Plasmas*, 18(5):050901, 2011.

[12] Kanani K. M. Lee, L. Robin Benedetti, Raymond Jeanloz, Peter M. Celliers, Jon H. Eggert, Damien G. Hicks, Stephen J. Moon, Andrew Mackinnon, Luis B. Da Silva, David K. Bradley, Walter Unites, Gilbert W. Collins, Emeric Henry, Michel Koenig, Alessandra Benuzzi-Mounaix, John Pasley, and David Neely. Laser-driven shock experiments on precompressed water: Implications for "icy" giant planets. *The Journal of Chemical Physics*, 125(1):014701, 2006.

[13] S. Bulanov, T. Esirkepov, D. Habs, F. Pegoraro, and T. Tajima. Relativistic laser-matter interaction and relativistic laboratoryastrophysics. *The European Physical Journal D*, 55(2):483, 2009.

[14] J K Crane, P Arnold, R J Beach, S Betts, C Boley, M Chang, M Chrisp, W Clark, J W Dawson, A Erlandson, M Henesian, J E Hernandez, I Jovanovic, V Kanz, M Key, A Lucianetti, M J Messerly, R Page, M Rushford, V Semenov, L Seppala, C Siders, C Stolz, D J Trummer, W Williams, J N Wong, G Tiebohl, and C J Barty. Status of the "arc", a quad of high-intensity beam lines at the national ignition facility. Technical report, United States, Jun 2006.

[15] M A Barrios, S P Regan, K B Fournier, R Epstein, R Smith, A Lazicki, R Rygg, D E Fratanduono, J Eggert, H-S Park, C Huntington, D K Bradley, O L Landen, and G W Collins. X-ray area backlighter development at the national ignition facility (invited). *Rev Sci Instrum*, 85(11):11D502, Nov 2014.

[16] A. Krygier, F. Coppari, G. E. Kemp, D. B. Thorn, R. S. Craxton, J. H. Eggert, E. M. Garcia, J. M. McNaney, H.-S. Park, Y. Ping, B. A. Remington, and M. B. Schneider. Developing a high-flux, high-energy continuum backlighter for extended x-ray absorption fine structure measurements at the national ignition facility. *Review of Scientific Instruments*, 89(10):10F114, 2018.

[17] Y. P. Opachich, R. F. Heeter, M. A. Barrios, E. M. Garcia, R. S. Craxton, J. A. King, D. A. Liedahl, P. W. McKenty, M. B. Schneider, M. J. May, R. Zhang, P. W. Ross, J. L. Kline, A. S. Moore, J. L. Weaver, K. A. Flippo, and T. S. Perry. Capsule implosions for continuum x-ray backlighting of opacity samples at the national ignition facility. *Physics of Plasmas*, 24(6):063301, 2017.

[18] R. Tommasini, C. Bailey, D. K. Bradley, M. Bowers, H. Chen, J. M. Di Nicola, P. Di Nicola, G. Gururangan, G. N. Hall, C. M. Hardy, D. Hargrove, M. Hermann,

M. Hohenberger, J. P. Holder, W. Hsing, N. Izumi, D. Kalantar, S. Khan, J. Kroll, O. L. Landen, J. Lawson, D. Martinez, N. Masters, J. R. Nafziger, S. R. Nagel, A. Nikroo, J. Okui, D. Palmer, R. Sigurdsson, S. Vonhof, R. J. Wallace, and T. Zobrist. Short pulse, high resolution, backlighters for point projection high-energy radiography at the national ignition facility. *Physics of Plasmas*, 24(5):053104, 2017.

[19] F. Albert, N. Lemos, J. L. Shaw, B. B. Pollock, C. Goyon, W. Schumaker, A. M. Saunders, K. A. Marsh, A. Pak, J. E. Ralph, J. L. Martins, L. D. Amorim, R. W. Falcone, S. H. Glenzer, J. D. Moody, and C. Joshi. Observation of betatron x-ray radiation in a self-modulated laser wakefield accelerator driven with picosecond laser pulses. *Phys. Rev. Lett.*, 118:134801, Mar 2017.

[20] N Lemos, F Albert, J L Shaw, D Papp, R Polanek, P King, A L Milder, K A Marsh, A Pak, B B Pollock, B M Hegelich, J D Moody, J Park, R Tommasini, G J Williams, Hui Chen, and C Joshi. Bremsstrahlung hard x-ray source driven by an electron beam from a self-modulated laser wakefield accelerator. *Plasma Physics and Controlled Fusion*, 60(5):054008, 2018.

[21] A. Modena, Z. Najmudin, A. E. Dangor, C. E. Clayton, K. A. Marsh, C. Joshi, V. Malka, Darrow. C.B., C. Danson, D. Neely, and F.N. Walsh. *Nature*, 377:606, 1995.

[22] C. M. Huntington, C. M. Krauland, C. C. Kuranz, R. P. Drake, H.-S. Park, D. H. Kalantar, B. R. Maddox, B. A. Remington, and J. Kline. Development of a short duration backlit pinhole for radiography on the national ignition facility. *Review of Scientific Instruments*, 81(10):10E536, 2010.

[23] C. C. Kuranz, B. E. Blue, R. P. Drake, H. F. Robey, J. F. Hansen, J. P. Knauer, M. J. Grosskopf, C. Krauland, and D. C. Marion. Dual, orthogonal, backlit pinhole radiography in omega experiments. *Review of Scientific Instruments*, 77(10):10E327, 2006.

[24] Reed Hollinger, Clayton Bargsten, Vyacheslav N. Shlyaptsev, Vural Kaymak, Alexander Pukhov, Maria Gabriela Capeluto, Shoujun Wang, Alex Rockwood, Yong Wang, Amanda Townsend, Amy Prieto, Patrick Stockton, Alden Curtis, and Jorge J. Rocca. Efficient picosecond x-ray pulse generation from plasmas in the radiation dominated regime. *Optica*, 4(11):1344–1349, Nov 2017.

[25] M.A. Barrios, K.B. Fournier, S.P. Regan, O. Landen, M. May, Y.P. Opachich, K. Widmann, D.K. Bradley, and G.W. Collins. Backlighter development at the national ignition facility (nif): Zinc to zirconium. *High Energy Density Physics*, 9(3):626 – 634, 2013.

[26] D. Babonneau, M. Primout, F. Girard, J.-P. Jadaud, M. Naudy, B. Villette, S. Depierreux, C. Blancard, G. Faussurier, K. B. Fournier, L. Suter, R. Kauffman, S. Glenzer, M. C. Miller, J. Grün, and J. Davis. Efficient multi-kev x-ray sources from laser-exploded metallic thin foils. *Physics of Plasmas*, 15(9):092702, 2008.

[27] A. B. Reighard, R. P. Drake, K. K. Dannenberg, D. J. Kremer, M. Grosskopf, E. C. Harding, D. R. Leibrandt, S. G. Glendinning, T. S. Perry, B. A. Remington, J. Greenough, J. Knauer, T. Boehly, S. Bouquet, L. Boireau, M. Koenig, and T. Vinci. Observation of collapsing radiative shocks in laboratory experiments. *Physics of Plasmas*, 13(8):082901, 2006.

[28] B. E. Blue, H. F. Robey, S. G. Glendinning, M. J. Bono, S. C. Burkhart, J. R. Celeste, R. F. Coker, R. L. Costa, S. N. Dixit, J. M. Foster, J. F. Hansen, C. A. Haynam, M. R. Hermann, J. P. Holder, W. W. Hsing, D. H. Kalantar, N. E. Lanier, D. A. Latray, H. Louis, B. J. MacGowan, G. R. Maggelssen, C. D. Marshall, E. I. Moses, A. J. Nikitin, D. W. O'Brien, T. S. Perry, M. W. Poole, V. V. Rekow, P. A. Rosen, M. B. Schneider, P. E. Stry, B. M. Van Wonterghem, R. Wallace, S. V. Weber, B. H. Wilde, D. T. Woods, and B. K. Young. Three-dimensional hydrodynamic experiments on the national ignition facility. *Physics of Plasmas*, 12(5):056313, 2005.

[29] F. J. Marshall, P. W. McKenty, J. A. Delettrez, R. Epstein, J. P. Knauer, V. A. Smalyuk, J. A. Frenje, C. K. Li, R. D. Petrasso, F. H. Séguin, and R. C. Mancini. Plasma-density determination from x-ray radiography of laser-driven spherical implosions. *Phys. Rev. Lett.*, 102:185004, May 2009.

[30] J. R. Rygg, O. S. Jones, J. E. Field, M. A. Barrios, L. R. Benedetti, G. W. Collins, D. C. Eder, M. J. Edwards, J. L. Kline, J. J. Kroll, O. L. Landen, T. Ma, A. Pak, J. L. Peterson, K. Raman, R. P. J. Town, and D. K. Bradley. 2d x-ray radiography of imploding capsules at the national ignition facility. *Phys. Rev. Lett.*, 112:195001, May 2014.

[31] C. Courtois, R. Edwards, A. Compant La Fontaine, C. Aedy, S. Bazzoli, J. L. Bourgade, J. Gazave, J. M. Lagrange, O. Landoas, L. Le Dain, D. Mastrosimone, N. Pichoff, G. Pien, and C. Stoeckl. Characterisation of a mev bremsstrahlung x-ray source produced from a high intensity laser for high areal density object radiography. *Physics of Plasmas*, 20(8):083114, 2013.

[32] S. Corde, C. Thaury, A. Lifschitz, G. Lambert, K. Ta Phuoc, X. Davoine, R. Lehe, D. Douillet, A. Rousse, and V. Malka. Observation of longitudinal and transverse self-injections in laser-plasma accelerators. *Nature Communications*, 4:1501 EP –, 02 2013.

[33] S. P. D. Mangles, B. R. Walton, M. Tzoufras, Z. Najmudin, R. J. Clarke, A. E. Dangor, R. G. Evans, S. Fritzler, A. Gopal, C. Hernandez-Gomez, W. B. Mori, W. Rozmus, M. Tatarakis, A. G. R. Thomas, F. S. Tsung, M. S. Wei, and K. Krushelnick. Electron acceleration in cavitated channels formed by a petawatt laser in low-density plasma. *Phys. Rev. Lett.*, 94:245001, Jun 2005.

[34] J L Shaw, F S Tsung, N Vafaei-Najafabadi, K A Marsh, N Lemos, W B Mori, and C Joshi. Role of direct laser acceleration in energy gained by electrons in a laser

wakefield accelerator with ionization injection. *Plasma Physics and Controlled Fusion*, 56(8):084006, jul 2014.

[35] J. L. Shaw, N. Lemos, L. D. Amorim, N. Vafaei-Najafabadi, K. A. Marsh, F. S. Tsung, W. B. Mori, and C. Joshi. Role of direct laser acceleration of electrons in a laser wakefield accelerator with ionization injection. *Phys. Rev. Lett.*, 118:064801, Feb 2017.

[36] P. M. King, K. Miller, N. Lemos, J. L. Shaw, B. F. Kraus, M. Thibodeau, B. M. Hegelich, J. Hinojosa, P. Michel, C. Joshi, K. A. Marsh, W. Mori, A. Pak, A. G. R. Thomas, and F. Albert. Predominant contribution of direct laser acceleration to high-energy electron spectra in a low-density self-modulated laser wakefield accelerator. *Phys. Rev. Accel. Beams*, 24:011302, Jan 2021.

[37] David H. Whittum, William M. Sharp, Simon S. Yu, Martin Lampe, and Glenn Joyce. Electron-hose instability in the ion-focused regime. *Phys. Rev. Lett.*, 67:991–994, Aug 1991.

[38] Christine Ann Coverdale. The interaction of intense subpicosecond laser pulses with underdense plasmas. 5 1995.

[39] John David Jackson. *Classical electrodynamics; 2nd ed.* Wiley, New York, NY, 1975.

[40] I. Kostyukov, S. Kiselev, and A. Pukhov. X-ray generation in an ion channel. *Physics of Plasmas*, 10(12):4818–4828, 2003.

[41] E. Esarey, B. A. Shadwick, P. Catravas, and W. P. Leemans. Synchrotron radiation from electron beams in plasma-focusing channels. *Phys. Rev. E*, 65:056505, May 2002.

[42] Eric Esarey, Sally K. Ride, and Phillip Sprangle. Nonlinear thomson scattering of intense laser pulses from beams and plasmas. *Phys. Rev. E*, 48:3003–3021, Oct 1993.

[43] P. Catravas, E. Esarey, and W. Leemans. Femtosecond x-rays from thomson scattering using laser wakefield accelerators. *Measurement Science and Technology*, (12):LBNL–47678, 2001.

[44] H. Bethe, W. Heitler, and Paul Adrien Maurice Dirac. On the stopping of fast particles and on the creation of positive electrons. *Proceedings of the Royal Society of London. Series A, Containing Papers of a Mathematical and Physical Character*, 146(856):83–112, 1934.

[45] A. Compant La Fontaine, C. Courtois, F. Gobet, F. Hannachi, J. R. Marquès, M. Tarisien, M. Versteegen, and T. Bonnet. Bremsstrahlung spectrum and photon dose from short-pulse high-intensity laser interaction on various metal targets. *Physics of Plasmas*, 26(11):113109, 2019.

[46] C. Joshi, T. Tajima, J. M. Dawson, H. A. Baldis, and N. A. Ebrahim. Forward raman instability and electron acceleration. *Phys. Rev. Lett.*, 47:1285–1288, Nov 1981.

[47] John M. Dawson. Nonlinear electron oscillations in a cold plasma. *Phys. Rev.*, 113:383–387, Jan 1959.

[48] A. Pukhov, Z.-M. Sheng, and J. Meyer-ter Vehn. Particle acceleration in relativistic laser channels. *Physics of Plasmas*, 6(7):2847–2854, 1999.

[49] C. Gahn, G. D. Tsakiris, A. Pukhov, J. Meyer-ter Vehn, G. Pretzler, P. Thirolf, D. Habs, and K. J. Witte. Multi-mev electron beam generation by direct laser acceleration in high-density plasma channels. *Phys. Rev. Lett.*, 83:4772–4775, Dec 1999.

[50] Xi Zhang, Vladimir N. Khudik, and Gennady Shvets. Synergistic laser-wakefield and direct-laser acceleration in the plasma-bubble regime. *Phys. Rev. Lett.*, 114:184801, May 2015.

[51] Xi Zhang, Vladimir N Khudik, Alexander Pukhov, and Gennady Shvets. Laser wakefield and direct acceleration with ionization injection. *Plasma Physics and Controlled Fusion*, 58(3):034011, feb 2016.

[52] Z. Najmudin, K. Krushelnick, E. L. Clark, S. P. D. Mangles, B. Walton, A. E. Dangor, S. Fritzler, V. Malka, E. Lefebvre, D. Gordon, F. S. Tsung, and C. Joshi. Self-modulated wakefield and forced laser wakefield acceleration of electrons. *Physics of Plasmas*, 10(5):2071–2077, 2003.

[53] C. D. Decker, W. B. Mori, and T. Katsouleas. Particle-in-cell simulations of raman forward scattering from short-pulse high-intensity lasers. *Phys. Rev. E*, 50:R3338–R3341, Nov 1994.

[54] D. Gordon, K. C. Tzeng, C. E. Clayton, A. E. Dangor, V. Malka, K. A. Marsh, A. Modena, W. B. Mori, P. Muggli, Z. Najmudin, D. Neely, C. Danson, and C. Joshi. *Phys. Rev. Lett.*, 80:2133–2136, Mar 1998.

[55] V. Malka, S. Fritzler, E. Lefebvre, M.-M. Aleonard, F. Burgy, J.-P. Chambaret, J.-F. Chemin, K. Krushelnick, G. Malka, S. P. D. Mangles, Z. Najmudin, M. Pittman, J.-P. Rousseau, J.-N. Scheurer, B. Walton, and A. E. Dangor. Electron acceleration by a wake field forced by an intense ultrashort laser pulse. *Science*, 298(5598):1596–1600, 2002.

[56] Masahiro Adachi, Eisuke Miura, Susumu Kato, Kazuyoshi Koyama, Shin ichi Masuda, Takayuki Watanabe, Hiromi Okamoto, Atsushi Ogata, and Mitsumori Tanimoto. Cascade acceleration of electrons by laser wakefield and direct laser field. *Japanese Journal of Applied Physics*, 45(5A):4214–4218, may 2006.

[57] N Lemos, J L Martins, F S Tsung, J L Shaw, K A Marsh, F Albert, B B Pollock, and C Joshi. Self-modulated laser wakefield accelerators as x-ray sources. *Plasma Physics and Controlled Fusion*, 58(3):034018, feb 2016.

[58] R. A. Fonseca, L. O. Silva, F. S. Tsung, V. K. Decyk, W. Lu, C. Ren, W. B. Mori, S. Deng, S. Lee, T. Katsouleas, and J. C. Adam. Osiris: A three-dimensional, fully relativistic particle in cell code for modeling plasma based accelerators. In Peter M. A. Sloot, Alfons G. Hoekstra, C. J. Kenneth Tan, and Jack J. Dongarra, editors, *Computational Science — ICCS 2002*, pages 342–351, Berlin, Heidelberg, 2002. Springer Berlin Heidelberg.

[59] A. Davidson, A. Tableman, W. An, F.S. Tsung, W. Lu, J. Vieira, R.A. Fonseca, L.O. Silva, and W.B. Mori. Implementation of a hybrid particle code with a pic description in r–z and a gridless description in ϕ into osiris. *Journal of Computational Physics*, 281:1063 – 1077, 2015.

[60] C. E. Clayton, J. E. Ralph, F. Albert, R. A. Fonseca, S. H. Glenzer, C. Joshia, W. Lu, K. A. Marsh, S. F. Martins, W. B. Mori, A. Pak, F. S. Tsung, B. B. Pollock, J. S. Ross, L. O. Silva, , and D. H. Froula. *Phys. Rev. Lett.*, 105:105003, 2010.

[61] Fei Li, Kyle G. Miller, Xinlu Xu, Frank S. Tsung, Viktor K. Decyk, Weiming An, Ricardo A. Fonseca, and Warren B. Mori. A new field solver for modeling of relativistic particle-laser interactions using the particle-in-cell algorithm. *Computer Physics Communications*, page 107580, 2020.

[62] Alexander Pukhov. Strong field interaction of laser radiation. *Reports on Progress in Physics*, 66(1):47–101, dec 2002.

[63] L Willingale, A V Arefiev, G J Williams, H Chen, F Dollar, A U Hazi, A Maksimchuk, M J-E Manuel, E Marley, W Nazarov, T Z Zhao, and C Zulick. The unexpected role of

evolving longitudinal electric fields in generating energetic electrons in relativistically transparent plasmas. *New Journal of Physics*, 20(9):093024, sep 2018.

[64] Tianhong Wang, Vladimir Khudik, Alexey Arefiev, and Gennady Shvets. Direct laser acceleration of electrons in the plasma bubble by tightly focused laser pulses. *Physics of Plasmas*, 26(8):083101, 2019.

[65] A. Rousse, K.T. Phuoc, R. Shah, A. Pukhov, E. Lefebvre, V. Malka, S. Kiselev, F. Burgy, J.P. Rousseau, and D. Umstadter. *Phys Rev Lett*, 93:135005–135005, 2004.

[66] Y. Glinec, J. Faure, L. Le Dain, S. Darbon, T. Hosokai, J. J. Santos, E. Lefebvre, J. P. Rousseau, F. Burgy, B. Mercier, and V. Malka. High-resolution γ-ray radiography produced by a laser-plasma driven electron source. *Phys. Rev. Lett.*, 94:025003, Jan 2005.

[67] K. Ta Phuoc and S. Corde. *Nature Photonics*, 6:308–311, 2012.

[68] Wenchao Yan, Colton Fruhling, Grigory Golovin, Daniel Haden, Ji Luo, Ping Zhang, Baozhen Zhao, Jun Zhang, Cheng Liu, Min Chen, Shouyuan Chen, Sudeep Banerjee, and Donald Umstadter. High-order multiphoton thomson scattering. *Nature Photonics*, 11:514 EP –, 06 2017.

[69] S. Kneip, S. R. Nagel, C. Bellei, N. Bourgeois, A. E. Dangor, A. Gopal, R. Heathcote, S. P. D. Mangles, J. R. Marquès, A. Maksimchuk, P. M. Nilson, K. Ta Phuoc, S. Reed, M. Tzoufras, F. S. Tsung, L. Willingale, W. B. Mori, A. Rousse, K. Krushelnick, and Z. Najmudin. Observation of synchrotron radiation from electrons accelerated in a petawatt-laser-generated plasma cavity. *Phys. Rev. Lett.*, 100:105006, Mar 2008.

[70] N. Lemos, F. Albert, J. L. Shaw, D. Papp, R. Polanek, P. King, A. L. Milder, K. A. Marsh, A. Pak, and B.B. Pollock. *Plasma Physics and Controlled Fusion*, 60:5, 2018.

[71] C. D. Chen, J. A. King, M. H. Key, K. U. Akli, and F. N. Beg. *Rev. Sci. Instrum.*, 79:10E305, 2008.

[72] G. J. Williams, R. Tommasini, N. Lemos, J. Park, and Hui Chen. High-energy differential-filtering photon spectrometer for ultraintense laser-matter interactions. *Review of Scientific Instruments*, 89(10):10F116, 2018.

[73] F Albert, A G R Thomas, S P D Mangles, S Banerjee, S Corde, A Flacco, M Litos, D Neely, J Vieira, Z Najmudin, R Bingham, C Joshi, and T Katsouleas. Laser wakefield accelerator based light sources: potential applications and requirements. *Plasma Physics and Controlled Fusion*, 56(8):084015, 2014.

[74] B. R. Maddox, H. S. Park, B. A. Remington, N. Izumi, S. Chen, C. Chen, G. Kimminau, Z. Ali, M. J. Haugh, and Q. Ma. High-energy x-ray backlighter spectrum measurements using calibrated image plates. *Review of Scientific Instruments*, 82(2):023111, 2011.

[75] S. Kneip, S. R. Nagel, C. Bellei, N. Bourgeois, A. E. Dangor, A. Gopal, R. Heathcote, S. P. D. Mangles, J. R. Marquès, A. Maksimchuk, P. M. Nilson, K. Ta Phuoc, S. Reed, M. Tzoufras, F. S. Tsung, L. Willingale, W. B. Mori, A. Rousse, K. Krushelnick, and Z. Najmudin. Observation of synchrotron radiation from electrons accelerated in a petawatt-laser-generated plasma cavity. *Phys. Rev. Lett.*, 100:105006, Mar 2008.

[76] T. Bonnet and M. Comet. *Review of Scientific Instruments*, 84:10, 2013.

[77] P. A. Ross. *Opt. Soc. Am. and Rev. Sci. Inst.*, 16:433, 1928.

[78] F. Albert, B. B. Pollock, J. L. Shaw, K. A. Marsh, J. E. Ralph, Y.-H. Chen, D. Alessi, A. Pak, C. E. Clayton, S. H. Glenzer, and C. Joshi. Angular dependence of betatron x-ray spectra from a laser-wakefield accelerator. *Phys. Rev. Lett.*, 111:235004, Dec 2013.

[79] C. Courtois, A. Compant La Fontaine, O. Landoas, G. Lidove, V. Meot, P. Morel, R. Nuter, E. Lefebvre, A. Boscheron, J. Grenier, M. M. Aleonard, M. Gerbaux, F. Gobet, F. Hannachi, G. Malka, J. N. Scheurer, and M. Tarisien. Effect of plasma density scale length on the properties of bremsstrahlung x-ray sources created by picosecond laser pulses. *Physics of Plasmas*, 16(1):013105, 2009.

[80] E. L. Dewald, J. E. Pino, R. E. Tipton, J. D. Salmonson, J. Ralph, E. Hartouni, S. F. Khan, R. Hatarik, C. V. Young, D. Thorn, V. A. Smalyuk, R. Sacks, A. Nikroo, N. Rice, S. A. MacLaren, S. Prisbrey, B. A. Remington, and F. Graziani. Pushered single shell implosions for mix and radiation trapping studies using high-z layers on national ignition facility. *Physics of Plasmas*, 26(7):072705, 2019.

[81] E. C. Merritt, J. P. Sauppe, E. N. Loomis, T. Cardenas, D. S. Montgomery, W. S. Daughton, D. C. Wilson, J. L. Kline, S. F. Khan, M. Schoff, M. Hoppe, F. Fierro, R. B. Randolph, B. Patterson, L. Kuettner, R. F. Sacks, E. S. Dodd, W. C. Wan, S. Palaniyappan, S. H. Batha, P. A. Keiter, J. R. Rygg, V. Smalyuk, Y. Ping, and P. Amendt. Experimental study of energy transfer in double shell implosions. *Physics of Plasmas*, 26(5):052702, 2019.

[82] O. Culfa, G. J. Tallents, A. K. Rossall, E. Wagenaars, C. P. Ridgers, C. D. Murphy, R. J. Dance, R. J. Gray, P. McKenna, C. D. R. Brown, S. F. James, D. J. Hoarty, N. Booth, A. P. L. Robinson, K. L. Lancaster, S. A. Pikuz, A. Ya. Faenov, T. Kampfer, K. S. Schulze, I. Uschmann, and N. C. Woolsey. Plasma scale-length effects on electron energy spectra in high-irradiance laser plasmas. *Phys. Rev. E*, 93:043201, Apr 2016.

[83] M. I. K. Santala, M. Zepf, I. Watts, F. N. Beg, E. Clark, M. Tatarakis, K. Krushelnick, A. E. Dangor, T. McCanny, I. Spencer, R. P. Singhal, K. W. D. Ledingham, S. C. Wilks, A. C. Machacek, J. S. Wark, R. Allott, R. J. Clarke, and P. A. Norreys. Effect of the

plasma density scale length on the direction of fast electrons in relativistic laser-solid interactions. *Phys. Rev. Lett.*, 84:1459–1462, Feb 2000.

[84] S. Jiang, A. G. Krygier, D. W. Schumacher, K. U. Akli, and R. R. Freeman. Effects of front-surface target structures on properties of relativistic laser-plasma electrons. *Phys. Rev. E*, 89:013106, Jan 2014.

[85] Sheng Jiang, Andrew G. Krygier, Douglass W. Schumacher, Kramer U. Akli, and Richard R. Freeman. Enhancing bremsstrahlung production from ultraintense laser-solid interactions with front surface structures. *The European Physical Journal D*, 68(10):283, 2014.

[86] S. Jiang, L. L. Ji, H. Audesirk, K. M. George, J. Snyder, A. Krygier, P. Poole, C. Willis, R. Daskalova, E. Chowdhury, N. S. Lewis, D. W. Schumacher, A. Pukhov, R. R. Freeman, and K. U. Akli. Microengineering laser plasma interactions at relativistic intensities. *Phys. Rev. Lett.*, 116:085002, Feb 2016.

[87] Tina Ebert, Nico W. Neumann, Leonard N. K. Dohl, Jonathan Jarrett, Christopher Baird, Robert Heathcote, Markus Hesse, Aasia Hughes, Paul McKenna, David Neely, Dean Rusby, Gabriel Schaumann, Christopher Spindloe, Alexandra Tebartz, Nigel Woolsey, and Markus Roth. Enhanced brightness of a laser-driven x-ray and particle source by microstructured surfaces of silicon targets. *Physics of Plasmas*, 27(4):043106, 2020.

[88] Luca Fedeli, Arianna Formenti, Lorenzo Cialfi, Andrea Pazzaglia, and Matteo Passoni. Ultra-intense laser interaction with nanostructured near-critical plasmas. *Scientific Reports*, 8(1):3834, 2018.

[89] Hui Chen, M. R. Hermann, D. H. Kalantar, D. A. Martinez, P. Di Nicola, R. Tommasini, O. L. Landen, D. Alessi, M. Bowers, D. Browning, G. Brunton, T. Budge,

J. Crane, J.-M. Di Nicola, T. Döppner, S. Dixit, G. Erbert, B. Fishler, J. Halpin, M. Hamamoto, J. Heebner, V. J. Hernandez, M. Hohenberger, D. Homoelle, J. Honig, W. Hsing, N. Izumi, S. Khan, K. LaFortune, J. Lawson, S. R. Nagel, R. A. Negres, L. Novikova, C. Orth, L. Pelz, M. Prantil, M. Rushford, M. Shaw, M. Sherlock, R. Sigurdsson, P. Wegner, C. Widmayer, G. J. Williams, W. Williams, P. Whitman, and S. Yang. High-energy (¿70 kev) x-ray conversion efficiency measurement on the arc laser at the national ignition facility. *Physics of Plasmas*, 24(3):033112, 2017.

[90] Andrew G. MacPhee, David Alessi, Hui Chen, Ginevra Cochran, Mark R. Hermann, Daniel H. Kalantar, Andreas J. Kemp, Shaun M. Kerr, Anthony J. Link, Tammy Ma, Andrew J. Mackinnon, Derek A. Mariscal, David Schlossberg, Riccardo Tommasini, Scott Vonhof, Clifford C. Widmayer, Scott C. Wilks, G. Jackson Williams, Wade H. Williams, and Kelly Youngblood. Enhanced laser–plasma interactions using non-imaging optical concentrator targets. *Optica*, 7(2):129–130, Feb 2020.

[91] G. J. Williams. Order of magnitude increase in laser-target coupling at near-relativistic intensitiesusing compound parabolic concentrators.

[92] S. C. Wilks, W. L. Kruer, M. Tabak, and A. B. Langdon. Absorption of ultra-intense laser pulses. *Phys. Rev. Lett.*, 69:1383–1386, Aug 1992.

[93] D. Rusby and et al. *In Review*, 2021.

[94] Hui Chen, Anthony J. Link, Roger van Maren, Pravesh K. Patel, Ronnie Shepherd, Scott C. Wilks, and Peter Beiersdorfer. High performance compact magnetic spectrometers for energetic ion and electron measurement in ultraintense short pulse laser solid interactions. *Review of Scientific Instruments*, 79(10):10E533, 2008.

[95] Nicola M. Winch, Scott A. Watson, and James F. Hunter. Modeling blur in various detector geometries for MeV radiography. In Thomas G. Flohr, Joseph Y. Lo, and

Taly Gilat Schmidt, editors, *Medical Imaging 2017: Physics of Medical Imaging*, volume 10132, pages 981 – 996. International Society for Optics and Photonics, SPIE, 2017.

[96] A. Hannasch, A. Laso Garcia, M. Laberge, R. Zgadzaj, A. Koehler, J.P. Couperus Cabadag, O. Zarini, T. Kurz, A. Ferrari, M. Molodtsova, L. Naumann, T. E. Cowan, U. Schramm, A. Irman, and M. C. Downer. Compact Spectroscopy of keV to MeV X-rays from a Laser Wakefield Accelerator. *Submitted to Scientific Reports*, pages 1–16, 2021.

[97] S. F. Khan and et al. *In Review*, 2021.

[98] M. B. Aufderheide, G. Henderson, A. E. S. von Wittenau, D. M. Slone, and H. E. Martz. Hades, a code for simulating a variety of radiographic techniques. In *IEEE Symposium Conference Record Nuclear Science 2004.*, volume 4, pages 2579–2583 Vol. 4, Oct 2004.

[99] Los alamos scientific laboratory. group x-6, mcnp : a general monte carlo code for neutron and photon transport. *Los Alamos, N.M. : [Springfield, Va.] :Dept. of Energy, Los Alamos Scientific Laboratory*, [for sale by the National Technical Information Service], 1979.